

University of Nottingham
UK | CHINA | MALAYSIA

Reactivity of the $O_2^{+\cdot}(H_2O)_n$ and $NO^{+\cdot}(H_2O)_n$ Cluster Ions in the D-region of the Ionosphere

Sainish Sharma, BSc
4297420

Supervised by Prof. Nick Besley and Prof. Tim Wright

School of Chemistry

The University of Nottingham

I hereby declare that this thesis is all my own work, except as indicated in the text:

Signature _____

Date_____/_____/_____

Abstract

The structure, spectroscopy and reactivity of hydrated dioxygenyl cluster ions $O_2^+\cdot(H_2O)_n$ with n = 1 – 5 has been theoretically investigated for the first time to understand potential reaction pathways that may convert O_2^+, present in high abundance in the upper layers of the ionosphere (E-region), into protonated water clusters, which are the predominant positively charged ion species in the lower D-region. The reactivity of hydrated nitrosonium as $NO^+\cdot(H_2O)_n$ with n = 4 – 5 has also been reinvestigated to clarify the potential intramolecular reaction for the formation of nitrous acid and a protonated water cluster.

Lowest energy geometries, binding energies and harmonic vibrational frequencies have been obtained for $O_2^+\cdot(H_2O)_n$ (n = 1 – 5) cluster ions. Through performing geometry optimisation calculations on $O_2^+\cdot(H_2O)$ using coupled cluster theory (CCSD(T)), second order Møller-Plesset perturbation theory (MP2) and density functional theory (DFT) with a wide range of exchange-correlation functionals, it was found that the MP2/6-311++G** level of theory was reliable for the calculation of minimum energy geometries and harmonic vibrational frequencies. In particular, methods that include 100% exact Hartree-Fock exchange such as MP2 and M06-HF were found to accurately describe the charge distribution in the clusters. MP2-based Born-Oppenheimer ab initio molecular dynamics (AIMD) simulations of the reactions of the $O_2^+\cdot(H_2O)_n$ and $NO^+\cdot(H_2O)_n$ cluster ions to form protonated water clusters reveal different mechanisms for the O_2^+ and NO^+ based ions. AIMD simulations of $O_2^+\cdot(H_2O)_n$ (n = 2 – 5) with initial velocities of the atoms sampled from the Maxwell-Boltzmann distribution at 220 K show that following charge transfer, a reaction to form a protonated water cluster and OH radical occurs rapidly where the neutral O_2 molecule is just a spectator. In contrast, the reaction of $NO^+\cdot(H_2O)_n$ (n = 4 – 5) has been hypothesised to involve an intracluster reaction, but no reaction is observed in the AIMD simulations using thermal initial velocities. AIMD simulations of a water molecule colliding with $NO^+\cdot(H_2O)_4$ to form $NO^+\cdot(H_2O)_5$ were performed to establish whether the resulting activated complex, with excess energy, would be more susceptible to forming a protonated water cluster and nitrous acid. The simulations showed that an intramolecular reaction could occur and was dependant on the impact direction and velocity of the incoming water molecule.

Acknowledgements

A special thanks to…

Room A46 for their guidance throughout this project.

Prof. Tim Wright for helping me develop a greater understanding of atmospheric chemistry.

And especially to Prof. Nick Besley for all the support and guidance he has offered throughout the year and for helping me develop a stronger understanding of theoretical chemistry.

Table of Contents

1. Introduction

1.1 Structure of the Ionosphere……..……. 1

1.2 O_2^+ in the Ionosphere.……...……. 1

1.3 $O_2^+ \cdot (H_2O)_n$ Clusters…..……...……. 6

1.4 NO^+ in the Ionosphere...……...…….……8

1.5 Reactivity of $NO^+ \cdot (H_2O)_n$ with n = 4 – 5…….……..11

1.6 Aims of the Project…….……...15

2. Background Theory

2.1 Principles of Quantum Mechanics…….…….. 17

2.2 Hartree-Fock Theory…...…….……...…...21

2.3 Basis Sets …...…….…….……..... 25

2.4 Beyond Hartree-Fock…….…….…...……...27

2.5 Density Functional Theory (DFT)…..……..…….… 30

2.6 Optimisation Methods…….....…..…….……..…. 37

2.7 Computing Vibrational Frequencies……...…..……..…..…… 38

2.8 Basis Set Superposition Error (BSSE).…….……...……..… 41

3. Computational Methodology…….……...……...42

4. Results and Discussion

4.1 Benchmarking……...…..…..…… 44

4.2 Structures of $O_2^+ \cdot (H_2O)_n$ with n = 1 – 5 ..…..…….……..…. 52

4.3 Spectra of $O_2^+ \cdot (H_2O)_n$ with n = 1 – 5 .....…..…….……...….68

4.4 Reactivity of $O_2^+ \cdot (H_2O)_n$ with n = 2 – 5 ..…..…….……..... 72

4.5 Reactivity of $NO^+ \cdot (H_2O)_n$ with n = 4 – 5 ….…….……...….75

4.6 Conclusions……..…..…… 80

5. References……..……... 85

List of Figures

Figure 1. Minimum energy geometries of $O_2^{+}\cdot(H_2O)$ in the doublet (1A and 1B) and quartet spin state (1C), optimised at the MP2/6-311++G** level of theory…….....44

Figure 2. The structure of $O_2^{+}\cdot(H_2O)$ and direction of the dipole moment predicted by CCSD(T), MP2 and a wide range of exchange-correlation functionals ……46

Figure 3. Lowest energy geometries of $O_2^{+}\cdot(H_2O)$ cluster when re-optimised at the MP2/6-311++G** level of theory.……..…….…….....…52

Figure 4. Lowest energy geometries of $O_2^{+}\cdot(H_2O)$ cluster when re-optimised at the M06-HF/6-311++G** level of theory.……52

Figure 5. Lowest energy geometries of $O_2^{+}\cdot(H_2O)_2$ cluster when re-optimised at the MP2/6-311++G** level of theory..……..……54

Figure 6. Lowest energy geometries of $O_2^{+}\cdot(H_2O)_2$ cluster when re-optimised at the M06-HF/6-311++G** level of theory...…….……..……54

Figure 7. Atomic charges (upper value in blue) and spin densities (lower value in red) for $O_2^{+}\cdot(H_2O)_2$...……...…….……57

Figure 8. Lowest energy geometries of $O_2^{+}\cdot(H_2O)_3$ cluster when re-optimised at the MP2/6-311++G** level of theory....…….…….…….……58

Figure 9. Lowest energy geometries of $O_2^{+}\cdot(H_2O)_3$ cluster when re-optimised at the M06-HF/6-311++G** level of theory.....…….……..….……58

Figure 10. Lowest energy geometries of $O_2^{+}\cdot(H_2O)_4$ cluster when re-optimised at the MP2/6-311++G** level of theory.....…….……..…….……..…62

Figure 11. Lowest energy geometries of $O_2^{+\cdot}(H_2O)_5$ cluster when re-optimised at the MP2/6-311++G** level of theory.....66

Figure 12. IR spectra for the lowest energy conformers of $O_2^{+\cdot}(H_2O)_n$ cluster ions with n = 1 – 5 computed using MP2.....69

Figure 13. Initial and final structures from AIMD of $O_2^{+\cdot}(H_2O)_n$ with the OH radical fragment formed circled.....74

Figure 14. Initial and final structures of the AIMD MP2/6-311++G** simulations of $NO^{+\cdot}(H_2O)_4$ and $NO^{+\cdot}(H_2O)_5$ with thermal initial velocities.....76

Figure 15. Composite diagram showing the initial positions of the water molecules in the collision-based AIMD simulations, the hydrogen atoms of the colliding water molecules have been omitted for clarity.....78

Figure 16. Ab initio molecular dynamics simulation of a water molecule collision onto the most stable $NO^{+\cdot}(H_2O)_4$ cluster leading to the formation of protonated water cluster and nitrous acid.....79

Figure 17. Composite diagram showing the initial locations of the water molecules that led to the formation of protonated water clusters.....79

List of Tables

Table 1. MP2 computed energies of the two low energy doublet and lowest energy quartet spin state structures…….....45

Table 2. Computed binding energies with the 6-311++G** basis set and difference with respect to CCSD(T) for $O_2^+ \cdot (H_2O)$ in kJ mol^{-1}……..…….....47

Table 3. Net Mulliken charge distribution on the O_2^+ and H_2O fragments in the $O_2^+ \cdot (H_2O)$ complex predicted by CCSD(T), MP2 and a wide range of DFT exchange correlation functionals…….……..…….....49

Table 4. Computed energies of the low energy molecular geometries obtained for $O_2^+ \cdot (H_2O)$, predicted using MP2 and M06-HF..…….…….....53

Table 5. Energies of the low energy molecular geometries obtained for $O_2^+ \cdot (H_2O)_2$, predicted by MP2 and M06-HF...……..…...…….....55

Table 6. Energies of the low energy molecular geometries obtained for $O_2^+ \cdot (H_2O)_3$, predicted by MP2 and M06-HF...…..…..……..…….....59

Table 7. Energies of the low energy molecular geometries obtained for $O_2^+ \cdot (H_2O)_4$, predicted using MP2 and M06-HF...…..…..……..……...….....64

Table 8. Energies of the low energy molecular geometries obtained for $O_2^+ \cdot (H_2O)_5$, predicted by MP2 and M06-HF...……..…….....67

1. Introduction

1.1 Structure of the Ionosphere

The ionosphere, the largest layer in the Earth's atmosphere, ranging in altitude between ~60 – 1000 km, is an ionised region in the upper atmosphere as a result of ionisation of gases by radiations of solar origin.[1] The ionosphere is described in terms of characteristic layers based on electron density, so-called the D-region (ranging in altitude between 60 km and 95 km), E-region (95 km to 150 km) and the F-region (150 km to 1000 km).[1] The ionosphere has a distinct chemical boundary at between 82 and 85 km in altitude, such that below ~82 km (D-region), the dominant positively charged species present are protonated water clusters. Conversely, above ~85 km, ions such as NO^+ and O_2^+ are most dominant.[2] Due to their significant role in the chemistry of the ionosphere, many experimental and theoretical studies have been performed on the nitrosonium ion, dioxygenyl ion and protonated water clusters to understand their reactivity.

1.2 O_2^+ in the Ionosphere

In 1960, Nicolet and Aikin built a theoretical model predicting that the major positively charged species present in the D-region of the ionosphere are NO^+, O_2^+ and N_2^+, in order of decreasing ion concentration and in line with their ionisation energies.[3] They studied the formation of the D-region in the ionosphere where they investigated the different sources of ionisation (X-rays, Solar Lyman-α radiation and cosmic rays) that could potentially ionise the principal constituents present including nitric oxide, molecular oxygen and molecular nitrogen.[3] It was reported that the ionisation of molecular oxygen could not occur via ultraviolet radiation as its ionisation cross-sections (the probability of an ionisation process to occur) hinders the penetration of such ionising radiation below 100 km in altitude.[3] In order for ultraviolet radiation to cause ionisation of molecular oxygen, it would require a wavelength less than 1026.5 Å which corresponds to the first ionisation potential of O_2. It was therefore proposed

that dioxygenyl cations are present in the ionosphere due to ionisation of molecular oxygen via X-rays ($\lambda < 10$ Å) and cosmic rays (reaction 1).

$$O_2 + h\upsilon \rightarrow O_2^+ + e^- \quad (1)$$

Five years later, Narcisi and Bailey confirmed the presence of O_2^+ as it was detected experimentally via a quadrupole mass spectrometer system, flown on a Nike Cajun rocket that sampled positively charged ions at altitudes between 64 – 112 km.[4] The rocket-borne mass spectrometer system performed positive ion composition measurements in the D-region of the ionosphere for the first time and showed that NO^+ and O_2^+ were present in high abundance, with NO^+ being the major primary ion.[4] The appearance of O_2^+ was first detected at an altitude of 75 km and the concentration was found to rapidly increase, close to the concentration of NO^+, as the mass spectrometer system approached altitudes ~ 82.5 km. However, the major positively charged ion species present in the D-region of the ionosphere (at altitudes between 63.4 – 82.5 km) were found to be protonated water clusters, $H^+(H_2O)_n$, where n is in the range of 1 – 3 and with the $H^+(H_2O)_2$ cluster being the most abundant.[4] Consequently, the mass spectrometer results had contradicted the theoretical model predicted by Nicolet and Aikin, who suggested the major positively charged ions present in the D-region were NO^+, O_2^+ and N_2^+.[3, 4] Considerable progress has been made since in the study of the positive ion composition of the D-region through improvements in rocket-borne mass spectrometry technology.[1] Consequently, significant amounts of research have been conducted to develop an understanding for the formation of protonated water clusters, their connections with hydrated dioxygenyl and nitrosonium ion clusters, and their roles in the chemistry of the ionosphere.

In 1969, following the first positive ion composition measurements in the D-region of the ionosphere where it was discovered that protonated water clusters are the most dominant positively charged ion species present, Fehsenfeld and Ferguson attempted to explain the formation of such species through qualitative reaction schemes, deduced from laboratory observations. They studied the ions produced after the addition of water vapour into flowing streams of O_2^+ ions where they observed a vapour phase reaction scheme that was thought to be responsible for the formation of protonated water clusters in the ionosphere.[5] Fehsenfeld and Ferguson proposed that the reaction sequence leading to the formation of protonated water clusters could

initially occur from the hydration of dominant positively charged ion species present in the D-region, such as O_2^+ (reaction 2), forming $O_2^+ \cdot (H_2O)$.[5] Following the hydration of O_2^+, the successive addition of water molecules was thought to produce hydrated dioxygenyl cluster ions through chain clustering reactions. It was experimentally reported that the hydrated dioxygenyl cluster, $O_2^+ \cdot (H_2O)$, upon collision with a second water molecule could potentially convert to a protonated water cluster through a chain breaking reaction, as shown in reaction 3.[5]

$$O_2^+ + H_2O + M \rightarrow O_2^+ \cdot (H_2O) + M \quad (2)$$

$$O_2^+ \cdot (H_2O) + H_2O \rightarrow H_3O^+ + OH + O_2 \quad (3)$$

However, it was discovered a faster reaction for the formation of the $O_2^+ \cdot (H_2O)$ cluster ion exists. At D-region ionospheric temperatures and conditions, it was expected that substantial amounts of O_2^+ would cluster with O_2 through a three-body reaction to form O_4^+ (reaction 4).[5] It was proposed that the existence of O_4^+ would dominate the formation of $O_2^+ \cdot (H_2O)$ since reaction 5 was found to occur and was significantly faster than reaction 4 under ionospheric conditions. Further hydration of $O_2^+ \cdot (H_2O)$ was thought to cause a branching reaction into two channels, reaction 3 which leads directly to the formation of $H^+(H_2O)$ and reaction 7 forming $H^+(H_2O)_2$. It was suggested that the observed branching ratio ($k_7 / k_3 \sim 10$) was responsible for the high concentration of $H^+(H_2O)_2$ when compared to $H^+(H_2O)$ in the D-region of the ionosphere, a fact discovered earlier by Narcisi and Bailey.[4]

$$O_2^+ + O_2 + M \rightarrow O_4^+ + M \quad (4)$$

$$O_4^+ + H_2O \rightarrow O_2^+ \cdot (H_2O) + O_2 \quad (5)$$

$$O_2^+ \cdot (H_2O) + H_2O \rightarrow H_3O^+ \cdot (OH) + O_2 \quad (6)$$

$$H_3O^+ \cdot (OH) + H_2O \rightarrow H^+ \cdot (H_2O)_2 + OH \quad (7)$$

In the same year, Good, Durden and Kebarle also performed experimental studies to deduce the reaction pathway for the formation of protonated water clusters under ionospheric conditions. A quadrupole mass spectrometer was used to record the initial and product ion intensities (in an O_2/H_2O system) as a function of time.[6] The successive intensity maxima of the product ions were monitored which allowed determination of the steps in their proposed major reaction sequence (8). Good, Durden and Kebarle independently utilised different experimental techniques and discovered their proposed reaction scheme supported the Fehsenfeld and Ferguson ion-molecule mechanism (that was based on qualitative experiments).[5, 6] They were able to perform measurements of rate constants for the reactions that could potentially be involved in the formation of protonated water clusters.

$$O_2^+ \rightarrow O_4^+ \rightarrow O_2^+\cdot(H_2O) \rightarrow H_3O^+\cdot(OH) \rightarrow H^+\cdot(H_2O)_2 \rightarrow H^+\cdot(H_2O)_n \qquad (8)$$

The existence of the $O_2^+\cdot(H_2O)_2$ cluster was also observed at room temperature by Good *et al.* where they explained its formation through direct 3-body addition of water to $O_2^+\cdot(H_2O)$, shown in reaction 9.[5] However, Adams *et al.* also observed the $O_2^+\cdot(H_2O)_2$ cluster where they proposed the $H_3O^+\cdot OH$ intermediate ion was first formed through a bimolecular reaction (10) followed by a 3-body association of O_2 via reaction 11.[7] Aside from the disagreement over the proposed mechanisms, there had also been a disagreement over the structure as Good *et al.* proposed the structure was $O_2^+\cdot(H_2O)_2$ whereas Adams *et al.* suggested the structure to exist in the form $H_3O^+\cdot OH\cdot O_2$.[6, 7] Reaction 12, in analogy with reaction 7 was also proposed to explain the presence of the observed ion peak which was assumed to be $H_3O^+H_2O$.

$$O_2^+\cdot(H_2O) + H_2O + M \rightarrow O_2^+\cdot(H_2O)_2 + M \qquad (9)$$

$$O_2^+\cdot(H_2O) + H_2O \rightarrow H_3O^+\cdot OH + O_2 \qquad (10)$$

$$H_3O^+\cdot OH + O_2 + M \rightarrow H_3O^+\cdot OH\cdot O_2 + M \qquad (11)$$

$$H_3O^+\cdot OH\cdot O_2 + H_2O \rightarrow H_3O^+H_2O + OH + O_2 \qquad (12)$$

In 1980 Rakshit *et al.* further investigated the mechanism for the formation of protonated water clusters from O_2^+ using an ion-drift chamber mass spectrometer where they also observed the existence of the $O_2^+{\cdot}(H_2O)_2$ cluster ion and reported the rate constants for the formation of such species (reactions 10 and 11). It was also suggested the cluster has two different stable structures, both possessing different reactivities (in the presence of water vapour) as the ion with the structure $O_2^+{\cdot}(H_2O)_2$ was expected to produce $H_3O^+H_2O$ ions less readily than the ion with the structure $H_3O^+{\cdot}OH{\cdot}O_2$.[8] As a result, Rakshit *et al.* proposed a reaction mechanism that was in agreement with Good *et al.* (reaction 12) and was also consistent with their experimental data.

In the following year, McCrumb *et al.* performed ion-molecule reaction experiments to investigate the mechanisms leading from primary O_2^+ to protonated water clusters where it was also reported reactions 10 and 11, previously proposed by Adams *et al.*, seemed possible for the formation of the $H_3O^+{\cdot}OH{\cdot}O_2$ ion. Possible intermediate ions were also discussed in terms of their stability and existence during the production of protonated water clusters under atmospheric conditions.[9] The $O_2^+{\cdot}(H_2O)_3$ ion, in contrast to previous experimental studies conducted by Good *et al.* and Rakshit *et al.*, was experimentally observed by McCrumb *et al.* in a drift tube at 223 K (a typical ionospheric temperature).[9] On the basis of their laboratory data, it was postulated the $H_3O^+{\cdot}H_2O{\cdot}OH$ intermediate was first formed through reaction 13 followed by a 3-body association of O_2 via reaction 14 during the production of the $O_2^+{\cdot}(H_2O)_3$ ion.[9] McCrumb *et al.* also proposed the pronated water cluster, $H_3O^+(H_2O)_2$ could also be formed through a water switching reaction (15), analogous to reaction 12.

$$O_2^+{\cdot}(H_2O)_2 + H_2O \rightarrow H_3O^+{\cdot}H_2O{\cdot}OH + O_2 \quad (13)$$

$$H_3O^+{\cdot}H_2O{\cdot}OH + O_2 + M \rightarrow O_2^+{\cdot}(H_2O)_3 + M \quad (14)$$

$$O_2^+{\cdot}(H_2O)_3 + H_2O \rightarrow H_3O^+(H_2O)_2 + OH + O_2 \quad (15)$$

1.3 $O_2^{+\cdot}(H_2O)_n$ Clusters

In 1975, Vanderhoff and Beyer reported absolute photodissociation cross-section measurements for the $O_2^{+\cdot}(H_2O)$ positive cluster ion at wavelengths within the visible region. The simplest photodissociation reaction, shown in reaction 16, was found to be highly exothermic where the bond energy of the $O_2^{+\cdot}(H_2O)$ positive cluster ion was reported to be ~77.2 kJ mol^{-1}.[10]

$$O_2^{+\cdot}(H_2O) + h\upsilon \rightarrow O_2^{+} + H_2O \qquad (16)$$

Susič *et al.* recorded the collision-induced dissociation, mass-analysed ion kinetic energy (CID MIKE) spectrum of the $O_2^{+\cdot}(H_2O)$ positive cluster ion for the first time where the spectrum only showed two significant peaks, one corresponding to O_2^+ and the other corresponding H_2O^+.[11] As a result, the dissociation of the $O_2^{+\cdot}(H_2O)$ positive cluster ion through the loss of a neutral water or oxygen molecule was concluded to be the predominant process, suggesting the cluster exists in the form of $O_2^{+\cdot}(H_2O)$. The absence of other significant peaks in the spectrum suggested a relativity weak bond present between the O_2 and H_2O moieties in the $O_2^{+\cdot}(H_2O)$ complex, precluding the possibility of the ion to exist in the form of $H_2O_3^+$.[11]

In 1999, Angel and Stace probed the fragmentation patterns of the clusters $O_2^{+\cdot}(H_2O)_n$ with $n = 1 – 5$ using three different cluster dissociation techniques including unimolecular (metastable) decay, collision-induced fragmentation and photodissociation via visible laser radiation.[2] The fragmentation patterns of the clusters were investigated to provide evidence for the reaction products anticipated in reaction 17, leading from $O_2^{+\cdot}(H_2O)_n$ to protonated water clusters.

$$O_2^{+\cdot}(H_2O)_n \rightarrow H^+(H_2O)_{n-1} + OH + O_2 \qquad (17)$$

For the $O_2^{+\cdot}(H_2O)$ cluster, a dominant loss of H_2O through bond fission to leave O_2^+ was evident from the metastable decay pattern which indicated the structure existed in the form of $O_2^{+\cdot}(H_2O)$, previously proposed by Susič *et al.*[2, 11] Conversely, for the $O_2^{+\cdot}(H_2O)_n$ ($n = 2 – 5$) cluster ions, it was proposed a charge transfer could initially occur from O_2^+ to the solvent waters, causing the cluster to adopt the structure

$O_2{\cdot}(H_2O)_{n-2}{\cdot}H_3O^+{\cdot}OH$.[2] The charge transfer would then result in the formation of protonated water clusters and cause OH, followed by O_2 to leave the cluster as separate entities in a sequential process, as shown in equations 18 and 19.[2]

$$O_2^{+\cdot}(H_2O)_n \rightarrow O_2.(H_2O)_{n-2}.H_3O^+OH \rightarrow (H_2O)_{n-2}.H_3O^+OH + O_2 \qquad (18)$$

$$(H_2O)_{n-2}.H_3O^+OH \rightarrow H_3O^+.(H_2O)_{n-2} + OH \qquad (19)$$

The CID MIKE spectrum of $O_2^+{\cdot}(H_2O)$ produced similar results to those obtained from the metastable decay pattern as a dominant loss of H_2O and O_2^+ was observed. The CID MIKE spectrum of $O_2^+{\cdot}(H_2O)_2$ displayed significant peaks corresponding to H_3O^+. Evidence from the CID MIKE spectrum and the metastable decay pattern suggested a charge transfer from O_2^+ to the water dimer initially occurs, facilitating the loss of OH and O_2 to give H_3O^+.[2] It was then concluded the structure of the cluster existed in the form $O_2{\cdot}H_3O^+OH$, previously proposed by Good *et al.*[2, 6] Photofragmentation spectra were also recorded where the dissociation pathways of $O_2^+{\cdot}(H_2O)$ (reaction 16) and $O_2^+{\cdot}(H_2O)_2$ (reaction 20) were observed.

$$O_2^{+\cdot}(H_2O)_2 + h\upsilon \rightarrow H_3O^+ + O_2 + OH \qquad (20)$$

More recently in 2003, Zhou *et al.* recorded the infrared (IR) spectrum and theoretically characterised the spectroscopy of the $O_2^+{\cdot}(H_2O)$ complex.[12] Absorptions corresponding to OH asymmetric stretch (3430.7 cm^{-1}) and OH symmetric stretch (3341.7 cm^{-1}), O-O stretch (1601.1 cm^{-1}) and H_2O-O_2 stretch (731.0 cm^{-1}) were observed.[12] Quantum chemical calculations were also carried out to investigate the structure and spectroscopy of the $O_2^+{\cdot}(H_2O)$ cation where geometry optimisations and harmonic vibrational frequency calculations were performed using density functional theory (with a range of exchange-correlation functionals including B3LYP, BHHLYP, BLYP, BP86 and SVWN) and the coupled cluster theory, CCSD(T). The B3LYP exchange correlation functional predicted 59% of the positive charge to be localised on the oxygen and the remaining 41% on the water molecule.[12] The computed harmonic vibrational frequencies were compared against experimentally observed frequencies where it was discovered all methods, excluding the SVWN/6-311++G** level of

theory, had underestimated the experimentally observed H_2O-O_2 stretching frequency (731 cm^{-1}).[12] This was surprising since computed harmonic vibrational frequencies are often higher than experimental values due to the negligence of anharmonicity. Conversely, the SVWN/6-311++G** level of theory (a method less accurate than hybrid and gradient corrected DFT) surprisingly predicted a H_2O-O_2 stretching frequency of 745 cm^{-1}, close to the experimental value. The large spin contamination (S^2 = 1.68), and the self-interaction error that DFT exhibits, were deemed responsible for the underestimated H_2O-O_2 stretching frequencies predicted by CCSD(T) and DFT, respectively.[12]

1.4 NO^+ in the Ionosphere

The presence of NO^+ in the upper layers of the Earth's ionosphere (E-region) was first proposed by Nicolet in 1945, where it was postulated the cation was formed via ionisation of NO by solar Lyman-α radiation (λ ~ 1215.7 Å), as shown in equation 21.[13]

$$NO + h\upsilon \rightarrow NO^+ + e^- \qquad (21)$$

In 1965, Narcisi and Bailey were the first to confirm the presence of NO^+ as it was experimentally detected via a quadrupole mass spectrometer system that sampled positively charge ions within the D and lower E-region of the ionosphere.[4] At altitudes ranging from between 64 – 111.7 km, NO^+ was found to be one of the major constituents. However, as previously mentioned, the major positively charged ion species detected within the D-region of the ionosphere were found to be protonated water clusters, $H^+(H_2O)_n$, where *n* is in the range of 1 – 3 and with the $H^+(H_2O)_2$ cluster being the most abundant.[4] Consequently, many experimental and theoretical studies have been performed since to understand the reaction pathways leading from NO^+ to protonated water clusters.

Fehsenfeld and Ferguson in 1969 first attempted to explain the formation of protonated water clusters in the ionosphere, starting from NO^+.[5] The ions produced after the addition of water vapour into flowing streams of NO^+ were studied where a vapour

phase reaction scheme was observed that seemed responsible for the formation of protonated water clusters, $H^+(H_2O)_n$ with n within the range of 1 – 3.[5] Fehsenfeld and Ferguson postulated the reaction sequence leading to protonated water clusters could initially occur from the hydration of NO^+ forming $NO^+\cdot(H_2O)$, shown in reaction 22.

$$NO^+ + H_2O + M \rightarrow NO^+\cdot(H_2O) + M \quad (22)$$

Following the formation of $NO^+\cdot(H_2O)$, successive addition of water molecules via three body processes was thought to produce larger hydrated nitrosonium ion clusters, $NO^+\cdot(H_2O)_n$. Fehsenfeld and Ferguson observed the cluster ions $NO^+\cdot(H_2O)_n$ where n is within the range of 1 – 3, but not the $NO^+\cdot(H_2O)_4$ cluster ion. It was then postulated that an exothermic chain breaking reaction upon hydration of $NO^+\cdot(H_2O)_3$ exists, forming a protonated water cluster and nitrous acid, shown in reaction 23. The formation of nitrous acid was proposed due to the need for OH-NO bond formation in order to make the reaction exothermic, as experimentally observed.[5]

$$NO^+\cdot(H_2O)_3 + H_2O \rightarrow H_3O^+(H_2O)_2 + HONO \quad (23)$$

Fehsenfeld and Ferguson showed the major atmospheric cation species present within the D-region of the ionosphere are formed via reactions initiated by three body ion-neutral associations. This motivated Dunkin *et al.* in 1971 to study NO^+ three body association reactions with abundant atmospheric molecules in an attempt to determine reaction mechanisms for NO^+ loss that occurs in the ionosphere, which may be a precursor in the formation of protonated water clusters.[14] It was proposed NO^+ is involved in an equilibrium with major atmospheric species, X, where X = N_2, O_2 or CO_2, forming $NO^+\cdot X$ complexes as shown in equation 24. The NO^+ association with N_2 was inferred to be extremely slow since minor $NO^+\cdot N_2$ signals were observed. NO^+ association with O_2 was also studied where no signals corresponding to $NO^+\cdot O_2$ were observed. Conversely, in the case for CO_2 association, signals corresponding to $NO^+\cdot CO_2$ were readily detected. It was proposed the $NO^+\cdot X$ complexes could undergo a rapid "switching" reaction, in which a second neutral species could replace the major atmospheric species, X, associated with NO^+.[14] The second neutral species could be any of the major species present within the atmosphere such as N_2, O_2 , NO, H_2O or

CO_2. Most relevant to this study is the switching reaction with water (equation 25), forming $NO^+ \cdot (H_2O)$.

$$NO^+ + X + M \rightarrow NO^+ \cdot X + M \quad (24)$$

$$NO^+ \cdot X + H_2O \rightarrow NO^+ \cdot (H_2O) + X \quad (25)$$

When compared to the simple direct three body association of H_2O to NO^+ (reaction 22), reaction sequences 26 and 27 were reported to be a more efficient mode of NO^+ hydration due to the natural occurrence of the large $[CO_2]/[H_2O]$ concentration ratio (10^2) that exists in the Earth's ionosphere.[14]

$$NO^+ + CO_2 + M \rightarrow NO^+ \cdot CO_2 + M \quad (26)$$

$$NO^+ \cdot CO_2 + H_2O \rightarrow NO^+ \cdot H_2O + CO_2 \quad (27)$$

In the same year, Fehsenfeld *et al.* studied their proposed three body stepwise solvation processes of NO^+ that leads to the formation of larger $NO^+ \cdot (H_2O)_{n+1}$ clusters (n = 1, 2 and 3).[15] Their proposed intramolecular reaction of $NO^+ \cdot (H_2O)_4$, forming a protonated water cluster and nitrous acid was also studied. Quantitative measurements were performed at 295 K in a flowing afterglow system which contained ionised NO/H_2O mixtures. It was discovered that as the concentration of water vapor increased in the system, signals corresponding to NO^+ decreased and the ions $NO^+ \cdot (H_2O)$, $NO^+ \cdot (H_2O)_2$ and $NO^+ \cdot (H_2O)_3$ increased in the following order due to consecutive hydrations.[15] The ion peaks corresponding to $NO^+ \cdot (H_2O)$ and $NO^+ \cdot (H_2O)_2$ had reached a similar maximum, however the ion peaks of $NO^+ \cdot (H_2O)_3$ remained significantly lower. The absence of an ion peak corresponding to $NO^+ \cdot (H_2O)_4$ suggested the cluster ion, $NO^+ \cdot (H_2O)_3$, reacts with a fourth water molecule to form a protonated water cluster and nitrous acid.[15] The ion peaks corresponding to $H_3O^+ \cdot (H_2O)_2$, $H_3O^+ \cdot (H_2O)_3$ and $H_3O^+ \cdot (H_2O)_4$ had all significantly increased upon the addition of water vapour. From the observations made, Fehsenfeld *at al.* deduced the following reaction mechanism and determined their rate constants.

$$NO^+ + H_2O + M \rightarrow NO^+ \cdot (H_2O) + M \quad (28)$$

$$NO^{+}\cdot(H_2O) + H_2O + M \rightleftharpoons NO^{+}\cdot(H_2O)_2 + M \quad (29)$$

$$NO^{+}\cdot(H_2O)_2 + H_2O + M \rightleftharpoons NO^{+}\cdot(H_2O)_3 + M \quad (30)$$

$$NO^{+}\cdot(H_2O)_3 + H_2O \rightleftharpoons H_3O^{+}(H_2O)_2 + HONO \quad (31)$$

$$H_3O^{+}(H_2O)_{n-1} + H_2O \rightleftharpoons H_3O^{+}(H_2O)_n \quad (32)$$

1.5 Reactivity of $NO^{+}\cdot(H_2O)_n$ with $n = 4 - 5$

In 1994, Choi *et al.* recorded the IR spectra of the cluster ions $NO^{+}\cdot(H_2O)_n$ within the region of 2700 – 3800 cm^{-1} in search for evidence for the proposed intramolecular reaction forming nitrous acid and a protonated water cluster where $n \geq 4$.[16] Vibrational predissociation spectroscopy was employed to obtain the IR spectra and determine the photofragments of the cluster ions $NO^{+}\cdot(H_2O)_n$, where n is within the range of 1 – 5. IR excitation upon the $NO^{+}\cdot(H_2O)_4$ cluster ion produced several photofragments, with the $NO^{+}\cdot(H_2O)_3$ fragment being most dominant which indicated the major dissociation channel involves the loss of one water molecule.[16] The observation of the minor photofragment, $H_3O^{+}\cdot(H_2O)_2$ indicated a dissociation channel involving the loss of neutral nitrous acid also occurs.[16] A relative yield of 12% nitrous acid, in comparison with the loss of H_2O was observed upon absorption of a single IR photon that possessed an energy approximately equivalent to the internal energy of the activated complex formed during the thermal collision $H_2O + NO^{+}\cdot(H_2O)_3$. It was concluded that the thermal collision, $H_2O + NO^{+}\cdot(H_2O)_3$ would lead to the formation of nitrous acid 10% of the time.[16] For the $NO^{+}\cdot(H_2O)_5$ cluster ion, the dominant dissociation channel observed involved the loss of $H_3O^{+}\cdot(H_2O)_3$, thus it was concluded IR excitation of the cluster resulted in almost complete loss of neutral nitrous acid. The IR spectrum of the $NO^{+}\cdot(H_2O)_4$ cluster ion displayed two (broad) bands at 3230 $cm^{-1}$and 3375 cm^{-1}, both corresponding to a hydrogen bonded OH stretch, indicating an OH bond is involved as a donor in hydrogen bonding.[16] The strong broad absorption band at 2800 cm^{-1} and the weaker band at 3190 cm^{-1} (assigned to the OH stretches of H_3O^{+})

provided clear evidence that the $NO^+\cdot(H_2O)_5$ intermediate ion has an H_3O^+ ion core hydrogen bonded to three solvating water molecules. The observed sharp band at 3576 cm^{-1}, assigned to the OH stretch of nitrous acid also indicated HONO was bound to the intermediate complex. As nitrous acid was the dominant dissociation product, it was proposed HONO forms a weaker hydrogen bond than the solvating water molecules. Thus, the intermediate complex (in the formation leading from $NO^+\cdot(H_2O)_5$ to a protonated water cluster and nitrous acid) was proposed to have H_3O^+ bound to three water molecules in the first solvation shell and nitrous acid hydrogen bonded to one of the first shell waters, $H_3O^+(H_2O)_3HONO$.[16]

Four years later, Angel and Stace investigated the collision-induced reactions of the $NO^+\cdot(H_2O)_n$ (where n is within the range of 3 – 5) cluster ions to determine the level of hydration of NO^+ required to promote the formation of nitrous acid and a protonated water cluster. The MIKE spectrum of $NO^+\cdot(H_2O)_3$ displayed only two loss channels, both of which did not correspond to collision-induced or metastable loss of nitrous acid.[17] Conversely, for the $NO^+\cdot(H_2O)_4$ cluster ion, two peaks corresponding to metastable and collision-induced loss of nitrous acid and water were observed.[17] The loss signals of water and nitrous acid were in a 9:1 ratio which agreed well with the IR spectroscopic study performed by Choi *et al.*[16, 17] For the $NO^+\cdot(H_2O)_5$ cluster ion, both metastable and collision induced signals corresponding to the loss of water and nitrous acid were also observed, however the loss of HONO from the cluster was substantially greater than the loss of water. This indicated the intramolecular reaction for the $NO^+\cdot(H_2O)_5$ cluster ion results in almost complete loss of nitrous acid.

Hammam *et al.* performed ab initio calculations on hydrated nitrosonium cluster ions, $NO^+\cdot(H_2O)_n$ to determine the geometries of the low energy isomers, harmonic vibrational frequencies and stepwise binding energies.[18, 19] As a clear description on the mechanism for the production of HONO and $H_3O^+\cdot(H_2O)_n$ was absent at the time, the reaction route for their formation from $NO^+\cdot(H_2O)_4$ was also investigated. When a water molecule was added to the second solvation shell water in their low energy optimised $NO^+\cdot(H_2O)_3$ structure, geometry optimisation calculations, performed at the MP2/6-311++G(2d,p) level of theory resulted in the formation of nitrous acid. [18, 19] From observation of the geometry changes in the complex during the optimisation calculation, proton transfer from the first solvation shell water to the second solvation shell water appeared to be the initial step of the reaction. [18, 19] The proposed $NO^+\cdot(H_2O)_4$ structure (possessing one, one and two water molecules in the first, second and third

solvation shell, respectively) had been previously proposed by Fehsenfeld *et al.* who also suggested the structure could lead to the formation of nitrous acid and a protonated water cluster based on experimental studies.

In 2010, Asada *et al.* clarified the reaction pathways for the formation of nitrous acid and a protonated water cluster from hydrated nitrosonium cluster ions, $NO^+\cdot(H_2O)_n$ (n = 4 – 5) through performing ab initio molecular orbital calculations at the MP2/aug-cc-pVTZ level of theory. Fifteen and thirteen stable optimised structures, in addition to two and three transition state structures were found for $NO^+\cdot(H_2O)_4$ and $NO^+\cdot(H_2O)_5$ cluster ions, respectively.[20] An intracluster reaction pathway for the $NO^+\cdot(H_2O)_4$ cluster ion was proposed where the product and reactant isomers were determined via intrinsic reaction coordinate calculations. As the structure of the reactant was very close to that of the transition state structure, the activation energy became so small, that it disappeared once zero-point energy corrections were taken into account.[20] In the study of $NO^+\cdot(H_2O)_5$ cluster ions, the thirteen stable optimised structures all possessed zero-point energy corrected relative energies very close to each other, in comparison to the fifteen isomers of $NO^+\cdot(H_2O)_4$.[20] The lowest energy structure with HONO bound was also very close in energy (0.47 kcal mol^{-1} higher) than that of the global minimum energy structure of $NO^+\cdot(H_2O)_5$. The lowest energy transition state structure was used in the intrinsic reaction coordinate calculation to determine the reactant and product structures in the potential intramolecular reaction for $NO^+\cdot(H_2O)_5$.[20] It was found the structure of the reactant promoted the single intracluster proton transfer reaction to form the product, consisting of nitrous acid bound to H_3O^+. Based on the transition state structures and intrinsic reaction coordinate calculations, the lowest activation energies for the intracluster reaction for $NO^+\cdot(H_2O)_5$ (3.4 kcal mol^{-1}) was found to be lower than that of $NO^+\cdot(H_2O)_4$ (4.1 kcal mol^{-1}).[20] The relative energy difference between the reactant, $NO^+\cdot(H_2O)_5$ and products were also found to be very close in energy. Reaction energies for the release of nitrous acid and a protonated water cluster in reaction 23 was found to be an endothermic process.[20] As a result, the authors concluded HONO release was difficult to occur in the $NO^+\cdot(H_2O)_4$ cluster ion. Similarly for $NO^+\cdot(H_2O)_5$, HONO release was also found to be an endothermic process but by only 0.93 kcal mol^{-1}, hence it was concluded the reaction could readily proceed if the system possesses some internal energy.[20]

Most recently in 2018, Linton *et al.* used quantum chemical methods including MP2 and DFT to study the reactivity of hydrated nitrosonium cluster ions.[21] AIMD

simulations were performed at a temperature of 220 K (typical ionospheric temperature) to study the formation of a protonated water cluster and nitrous acid from the $NO^+\cdot(H_2O)_5$ cluster ion. [21] The AIMD simulations were performed using the lowest energy isomers of $NO^+\cdot(H_2O)_5$ (determined through a random movement search procedure) as initial starting structures and initial velocities were sampled from a Maxwell-Boltzmann distribution at a temperature of 220 K. The simulations were performed at the MP2 level and DFT with the M06-HF and BLYP-D exchange-correlation functionals and with a small (6-31G) and moderately sized (6-31+G*) basis set. On the timescale studied (4 ps), a reaction forming nitrous acid and a protonated water cluster was observed for the simulations using DFT (M06-HF and BLYP-D) with a small basis set (6-31G). [21] In contrast, simulations performed using MP2 and DFT with the larger 6-31+G* basis set did not lead to an observed reaction. The behaviour was explained through the comparison of the relative energies of the lowest energy $NO^+\cdot(H_2O)_5$ cluster ion and the cluster ion with HONO within the structure. [21] It was discovered that all methods with the small 6-31G basis set found the HONO containing cluster ion to be lower in energy than the $NO^+\cdot(H_2O)_5$ cluster ion, with DFT predicting a relative energy of -100 kJ mol^{-1}. [21] It was concluded the inaccurate description of the energetics of the system led to a reaction forming nitrous acid and a protonated water cluster in the AIMD simulations. All other methods (MP2 and DFT with the larger 6-31+G* basis set) had shown the energy of the final structure (with HONO within the structure) to be higher than the initial starting structure. The energy change and activation energies were also predicted to be greatest via MP2 calculations which suggested a lower level of reactivity was expected from MP2 in comparison to DFT calculations. The simulations showed the reaction pathway involved a charge transfer from NO^+ to the subsequent water molecules which caused a reorganisation resulting in the formation of H_3O^+, followed by nitrous acid formation. [21] Conversely, a second reaction pathway was also observed which involved a more concerted charge transfer from NO^+ (to the subsequent water molecules) and formation of nitrous acid. The calculations performed in the study suggested an intramolecular reaction was very unlikely to occur from equilibrated low energy geometries and the quality of the basis set had a great influence on the occurrence for the formation of nitrous acid and a protonated water cluster from the $NO^+\cdot(H_2O)_5$ cluster ion. [21] It was suggested that the observed reactivity in the ionosphere could be due $NO^+\cdot(H_2O)_5$ being formed via an association of a water molecule to $NO^+\cdot(H_2O)_4$, leading to a highly vibrationally excited

$NO^+\cdot(H_2O)_5$ complex that would be more susceptible to rearrangement and dissociation of nitrous acid and a protonated water cluster.

1.6 Aims of the Project

The unexpectedly high concentration of protonated water clusters present in the D-region of the ionosphere has been postulated to arise from cluster ions such as $O_2^+\cdot(H_2O)_n$ and $NO^+\cdot(H_2O)_n$, although the detailed mechanism of the underlying reactions is not understood.[3] The aim of the project is to determine the lowest energy structures of $O_2^+\cdot(H_2O)_n$ with n = 1 – 5 cluster ions and to deduce the intramolecular reaction pathway leading to the formation of a protonated water cluster from cluster ions $O_2^+\cdot(H_2O)_n$ and $NO^+\cdot(H_2O)_n$, as shown in reactions 17 and 31.

Initially, the lowest energy geometries of $O_2^+\cdot(H_2O)_n$ with n = 1 – 5 cluster ions will be determined using a hierarchical procedure where unrestricted HF with the 6-31+G* basis set is used to search the conformational space and identify low energy isomers. HF theory is employed at this stage for its computational efficiency and to reduce the computational cost during the random movement searches of the potential energy surfaces for each cluster ion. MP2 level calculations will then be used to re-optimise the low energy isomers obtained from the random movement search procedure to determine the lowest energy structure of each cluster ion. Subsequently, binding energies of $O_2^+\cdot(H_2O)$ will be computed using a wide range of exchange-correlation functionals with the counterpoise correction and the error with respect to CCSD(T) results will be calculated to investigate how the results from DFT vary with the nature of the exchange-correlation functional and to determine the most suitable method for studying the larger $O_2^+\cdot(H_2O)_n$ with n = 2 – 5 cluster ions.

Harmonic vibrational frequencies will be computed for the lowest energy $O_2^+\cdot(H_2O)_n$ with n = 1 – 5 structures obtained from the random movement search procedure to determine stationary points and vibrational properties. Computed harmonic vibrational frequencies and intensities will allow theoretical IR spectra to be produced which can be compared to experimental IR spectra in future experimental work on $O_2^+\cdot(H_2O)_n$ cluster ions. The spectra will be focussed on the O-H stretching region since this is the region of the spectrum that is typically measured in the reported spectra.

MP2 theory based Born-Oppenheimer AIMD simulations will be performed on the lowest energy structures of $O_2^+ \cdot (H_2O)_n$ (n = 2 – 5) cluster ions at a typical ionospheric temperature to study the proposed intramolecular reaction pathway that leads to the formation of a protonated water cluster.[2] MP2 theory based Born-Oppenheimer AIMD simulations will also been carried out on the lowest energy structures of $NO^+ \cdot (H_2O)_n$ (n = 4 – 5) cluster ions to investigate potential reaction pathways that could result in the formation of nitrous acid and a protonated water cluster, as experimentally observed within the D-region of the ionosphere.[4] Collision dynamics simulations of an association of a water molecule onto the lowest energy $NO^+ \cdot (H_2O)_4$ configuration to form $NO^+ \cdot (H_2O)_5$ will be carried out to deduce whether the resulting activated complex, with excess energy, would be more susceptible to forming nitrous acid and a protonated water cluster.

2. Background Theory

2.1 Principles of Quantum Mechanics

2.1.1 The Wavefunction (Ψ)

The wavefunction, Ψ, in quantum mechanics possesses all the information about the system and from the wavefunction, properties such as energy, momentum and most importantly, the location of the particle can be determined. Max Born first attempted to deduce a mathematical description for the location of a particle where he focused on the square modulus of the wavefunction. If the wavefunction of a particle possesses the value Ψ at position x, then the probability of locating the particle between x and $x + dx$ is proportional to the square modulus of the wavefunction, $|\Psi|^2$, so called the probability density. Integrating the probability density, $|\Psi|^2$ over a specified region of space ($x + dx$) allows the probability of the particle existing within the region to be determined. Furthermore, by integrating over all space ($d\boldsymbol{\tau}$)**,** equation 1 follows as the probability of locating a particle in all space must equal to one.

$$\int_{-\infty}^{\infty} \Psi^* \Psi d\boldsymbol{\tau} = 1 \qquad (1)$$

2.1.2 The Schrödinger equation

The Schrödinger equation, first proposed by Erwin Schrödinger in 1926 introduced a second-order differential equation which allows the wavefunction of any system to be calculated and forms the basis of quantum chemical calculations. The Schrödinger equation has two forms; the time-dependent Schrödinger equation (shown in equation 2) is one in which time exists and describes how the wavefunction of a particle changes with time. In equation 2, i is an imaginary unit, $\hbar$ is the reduced Planck's constant, $\widehat{H}$ is the Hamiltonian operator and N and M are the total number of electrons and nuclei within the chemical system, respectively.

$$i\hbar\frac{\delta}{\delta t}\Psi(\boldsymbol{X}_1,\ldots,\boldsymbol{X}_N,\boldsymbol{R}_1,\ldots,\boldsymbol{R}_M,t)=\hat{H}\Psi(\boldsymbol{X}_1,\ldots,\boldsymbol{X}_N,\boldsymbol{R}_1,\ldots,\boldsymbol{R}_M,t) \quad (2)$$

Equation 2 shows that the wavefunction, Ψ is dependent upon the position vectors of all electrons $\boldsymbol{X}_i$ and nuclei $\boldsymbol{R}_i$ within the system as well as with time, t. The second form, the time-independent Schrödinger equation (shown in equation 3) possesses no time dependency and describes the allowed energies within the system. From the time-independent Schrödinger equation, it can be seen the energy (E) and wavefunction (Ψ) are only dependent on the position vectors of all the electrons $\boldsymbol{X}_i$ and nuclei $\boldsymbol{R}_i$ within the system.

$$\hat{H}\Psi(\boldsymbol{X}_1,\ldots,\boldsymbol{X}_N,\boldsymbol{R}_1,\ldots,\boldsymbol{R}_M)=E\Psi(\boldsymbol{X}_1,\ldots,\boldsymbol{X}_N,\boldsymbol{R}_1,\ldots,\boldsymbol{R}_M) \quad (3)$$

$\hat{H}$ is the Hamiltonian operator that represents the total energy of the system, i.e. the summation of the potential and kinetic energies for both the nuclei and electrons within the chemical system (equation 4). The symbols A and B refer to the nuclei whereas i and j represent the electrons within the system. The r_{Ai} term represents the distance between nucleus A and electron i and r_{ij} is the inter-electronic distance between electrons i and j. The symbol r_{AB} represents the distance between nuclei A and B with atomic numbers Z_A and Z_B, respectively. In atomic units, $\hat{H}$ can be written:

$$\hat{H}=-\sum_A\frac{1}{2M_A}\nabla_A^2-\sum_i\frac{1}{2}\nabla_i^2+\sum_{A>B}\frac{Z_AZ_B}{r_{AB}}-\sum_{Ai}\frac{Z_A}{r_{Ai}}+\sum_{i>j}\frac{1}{r_{ij}} \quad (4)$$

When constructing the Hamiltonian, the electron-nuclear attraction, nuclear-nuclear repulsion and electron-electron interaction terms need to be accounted for which causes the Hamiltonian to become too complex to be solved exactly for many electron systems. As a result, exact solutions to the Schrödinger equation have only been obtained for one electron systems. Therefore, to solve the Schrödinger equation for polyatomic molecules, approximations are applied to the time independent Hamiltonian.

2.1.3 Born-Oppenheimer Approximation

With the mass of nuclei being much greater than an electron (proton mass is 1836 times larger in comparison to the mass of an electron), nuclei are expected to move very slowly in comparison to electrons, and thus can be treated as stationary whilst the electrons move around their potential field. Therefore, it can be assumed the electronic motion in a given chemical system is independent of nuclear motion. The nuclei can be assumed to be fixed in arbitrary positions, and that the nuclear and electronic motion can be separated. As the nuclei are in fixed arbitrary positions, they possess no kinetic energy and the nuclear-nuclear interactions are constant. Consequently, the Schrödinger equation can be solved to deduce the wavefunction of the electrons within the system only (Ψ_{elec}). The kinetic energy of the nuclei (first term in equation 4) can therefore be neglected and the nuclear-nuclear interactions can be treated as a constant, as shown in equation 5 and 6. As a result, the electronic motion can be determined for a fixed position of the nuclei.

$$\widehat{H}_{elec}\Psi_{elec}(\boldsymbol{X}_1, \dots, \boldsymbol{X}_N) = E_{elec}\Psi_{elec}(\boldsymbol{X}_1, \dots, \boldsymbol{X}_N) \tag{5}$$

$$\widehat{H}_{elec} = -\sum_i \frac{1}{2}\nabla_i^2 - \sum_{Ai} \frac{Z_A}{r_{Ai}} + \sum_{i>j} \frac{1}{r_{ij}} \tag{6}$$

The electronic Hamiltonian ($\widehat{H}_{elec}$) can be used to solve the electronic Schrödinger equation for a specific internuclear separation in a diatomic molecule, for example, and the resulting eigenvalue solution obtained is referred to as the electronic energy (E_{elec}). Subsequently, different fixed arrangements of the nuclei may be adopted, and the Schrödinger equation can be solved again to deduce the total energy of the system. A repetition of the calculation at different internuclear separations allows a comparison of how the energy varies with bond length for diatomics and also with bond angles for polyatomic molecules. As a result, a molecular potential energy curve can be obtained for diatomic molecules, whereas if the bond length and angle changes in polyatomic molecules, a potential energy surface (PES) can be deduced. Thus, a plot of the total energy (deduced from sets of solutions at different internuclear distances) against the specified internuclear distance can be deduced for a diatomic molecule. From such a

potential energy curve, important parameters such as the equilibrium bond length (R_e) and bond dissociation energy (D_0) can be established.

2.1.4 Potential Energy Surface

Potential energy surfaces arise from the Born-Oppenheimer approximation which separates the nuclear and electronic motion in a chemical system. The potential energy surface represents how the electronic energy (E_{elec}) varies as a function of the relative positions of all atoms within a chemical system in which the nuclear coordinates may undergo changes in bond lengths, bond angles and torsional angles. For a linear molecule with N atoms, the potential energy surface would possess $3N - 5$ internal coordinates and $3N - 6$ internal coordinates for non-linear molecules. Once the number of internal coordinates within a system increases to two, the potential energy surface can be represented by a three-dimensional plot. However, once the number of internal coordinates within a system increases above two, a cut-through potential energy surface is required to represent the system since visualising the entire potential energy surface would be impossible.

The most useful information gained from the potential energy curve or surfaces are minima and first order saddle points which correspond to equilibrium geometries and transition-state structures, respectively. Both equilibrium and transition-state structures correspond to stationary points on the potential energy surface in which the first derivative of the electronic energy (E_{elec}) with respect to the internal coordinates is zero. There are two types of minima; unique global minimum and local minima which correspond to the most stable and meta-stable configurations of the chemical system, respectively. Characterisation of both equilibrium and transition-state structures requires determination of the eigenvalues of Hessian (second derivative matrix) as equilibrium geometries are defined by Hessians whose eigenvalues are positive, conversely transition-state structures are defined by Hessians with exactly one negative eigenvalue.[24]

2.1.5 Variational Theorem

The variational theorem forms the basis for methods used in quantum chemistry to solve the time-independent Schrödinger equation (equation 2) and hence provides an estimate for the ground state energy of a given chemical system.

$$E_0 \leq E = \langle \Psi | \hat{H} | \Psi \rangle \tag{7}$$

The variational theorem involves estimating an arbitrary (trial) wavefunction that consists of variational (adjustable) parameters. By varying the parameters until the energy of the trial wavefunction (E) has reached a minimum, a close approximation to the exact wavefunction and ground state energy of a system can be deduced. The variational theorem states the exact ground state energy, E_0 is always less than, or equal to the energy obtained from the normalised trial wavefunction, E (mathematically represented in equation 7). Therefore, the best approximate trial wavefunction is the one that possesses the lowest energy.

2.2 Hartree-Fock Theory

Hartree-Fock (HF) theory is a method that was recently developed after the publication of the Schrödinger equation and is fundamental to most of electronic structure theory.[28 – 31] HF theory was developed to solve the electronic Schrödinger equation that results from the full Schrödinger equation after the application of the Born-Oppenheimer approximation which separates the nuclear and electronic motion in a chemical system. Although the Schrödinger equation can be solved exactly for one-electron systems (such as the hydrogen atom and helium ion), it is impossible to solve the Schrödinger equation for systems with $N > 2$ as the fifth term in equation 4 couples the motion of the electrons.

In a multi-electron system, the wavefunction can be represented by the product of one-electron wavefunctions, also referred to as orbitals. Equation 8 represents an N-electron closed-shell system where electron 1 occupies molecular orbital ψ_a with spin α, electron 2 occupies molecular orbital ψ_a with spin β and so on…

$$\Psi = \psi_{a,\alpha}(1)\psi_{a,\beta}(2)\ldots\psi_{z,\beta}(N) \tag{8}$$

The multi-electron wavefunction however must obey to the Pauli exclusion principle which states that a maximum of two electrons may occupy any given orbital, and if two electrons do occupy an orbital, their spins must be paired. The Pauli exclusion principle is based on the general statement called the Pauli principle which states when the labels of two identical fermions (sub-atomic particles that possess half-integral spin) are exchanged, the total wavefunction must interchange sign. To satisfy the Pauli principle, an N-bodied wavefunction can be represented by the sum of all possible permutations assigned with an appropriate sign, shown in equation 9.

$$\Psi = \psi_{a,\alpha}(\boldsymbol{X}_1)\psi_{a,\beta}(\boldsymbol{X}_2)\ldots\psi_{z,\beta}(\boldsymbol{X}_N) - \psi_{a,\alpha}(\boldsymbol{X}_2)\psi_{a,\beta}(\boldsymbol{X}_1)\ldots\psi_{z,\beta}(\boldsymbol{X}_N) + \ldots \tag{9}$$

As there are $N!$ terms in the expression, the entire sum can be represented as a determinant, known as the Slater determinant, shown in equation 10. The first term in the expression ensures the wavefunction is normalised and the elements within the determinant are one-electron spin orbital functions that depend on the spatial and spin coordinates ($\boldsymbol{X}_i$).

$$\Psi_{SD} = \frac{1}{\sqrt{N!}} \begin{vmatrix} \psi_{a,\alpha}(\boldsymbol{X}_1) & \psi_{a,\beta}(\boldsymbol{X}_1) & \cdots & \cdots & \psi_{z,\beta}(\boldsymbol{X}_1) \\ \psi_{a,\alpha}(\boldsymbol{X}_2) & \psi_{a,\beta}(\boldsymbol{X}_2) & \cdots & \cdots & \psi_{z,\beta}(\boldsymbol{X}_2) \\ \vdots & \vdots & & & \vdots \\ \vdots & \vdots & & & \vdots \\ \psi_{a,\alpha}(\boldsymbol{X}_N) & \psi_{a,\beta}(\boldsymbol{X}_N) & \cdots & \cdots & \psi_{z,\beta}(\boldsymbol{X}_N) \end{vmatrix} \tag{10}$$

The Slater determinant therefore ensures the Pauli exclusion principle is obeyed as the wavefunction is anti-symmetric, i.e. when the electrons within the chemical system are interchanged, the sign of the wavefunction also interchanges (equation 11). From rearrangement of equation 5, the electronic energy (E_{elec}) can also be established, as shown in equation 12.

$$\Psi(\boldsymbol{X}_1, \ldots, \boldsymbol{X}_i, \ldots \boldsymbol{X}_j, \ldots \boldsymbol{X}_N) = -\Psi(\boldsymbol{X}_1, \ldots, \boldsymbol{X}_j, \ldots \boldsymbol{X}_i, \ldots \boldsymbol{X}_N) \tag{11}$$

$$E = \frac{\langle \Psi_{SD} | \widehat{H}_{elec} | \Psi_{SD} \rangle}{\langle \Psi_{SD} | \Psi_{SD} \rangle} \tag{12}$$

Substituting equation 6 for the electronic Hamiltonian ($\widehat{H}_{elec}$), equation 10 for the Slater determinant and replacing the denominator with 1 (as the wavefunction, Ψ_{SD} is normalised), equation 12 can be rearranged, shown in equation 13.

$$E_{SD} = \langle \Psi_{SD} | \widehat{H}_{elec} | \Psi_{SD} \rangle = \sum_{i}^{N} h_{ii} + \sum_{i>j}^{N} (J_{ij} - K_{ij}) \tag{13}$$

where

$$h_{ii} = \langle \psi_i | \hat{h} | \psi_i \rangle = \int \psi_i^*(\boldsymbol{X})(-\frac{1}{2}\nabla_i^2 - \sum_{Ai} \frac{Z_A}{r_{Ai}})\psi_i(\boldsymbol{X}) d\boldsymbol{X} \tag{14}$$

$$J_{ij} = (ii|jj) = \iint \frac{\psi_i^*(\boldsymbol{X}_1)\psi_j^*(\boldsymbol{X}_2)\psi_i(\boldsymbol{X}_1)\psi_j(\boldsymbol{X}_2)}{r_{12}} d\boldsymbol{X}_1 d\boldsymbol{X}_2 \tag{15}$$

$$K_{ij} = (ij|ji) = \iint \frac{\psi_i^*(\boldsymbol{X}_1)\psi_j^*(\boldsymbol{X}_2)\psi_j(\boldsymbol{X}_1)\psi_i(\boldsymbol{X}_2)}{r_{12}} d\boldsymbol{X}_1 d\boldsymbol{X}_2 \tag{16}$$

The term h_{ii}, shown in equation 14 is referred to as the one electron part. The one electron operator, $\hat{h}$ corresponds to the average kinetic energy of the electron plus the nuclear attraction experienced by the electron. The J_{ij} and K_{ij} terms in the second summation in equation 13 are referred to as the two-electron part and are the coulomb and exchange integrals, respectively. Summation of the Coulomb integrals (J_{ij}) gives the Coulomb energy which corresponds to the classic Coulomb repulsion between the electrons within the system. Conversely, summation of the exchange integrals (K_{ij}) provides the exchange energy which is a result of the wavefunction being anti-symmetric.

Combining the Slater determinant wavefunction (equation 13) with the variation theorem (equation 7) leads to the HF equations which are a system of

equations that can be solved to give the wavefunction and energy for many-electron chemical systems. The HF equations introduce the one-electron Fock operator

$$\hat{f}\psi_{i,\sigma} = \varepsilon\psi_{i,\sigma} \tag{17}$$

where $\hat{f}$ is the Fock operator, ε is the energy of the molecular orbital (ψ_i) and σ corresponds to the spin of the electron. The Fock operator consists of three terms, $\hat{h}$, $\hat{J}$ and $\widehat{K}$.

$$\hat{f} = \hat{h} + \sum_{j=1}^{N} (\hat{J}_j - \widehat{K}_j) \tag{18}$$

$$\widehat{J}_j\psi_i(\boldsymbol{X}_1) = \left[\int \frac{\psi_j^*(\boldsymbol{X}_2)\psi_j(\boldsymbol{X}_2)}{r_{12}} d\boldsymbol{X}_2\right]\psi_i(\boldsymbol{X}_1) \tag{19}$$

$$\widehat{K}_j\psi_i(\boldsymbol{X}_1) = \left[\int \frac{\psi_j^*(\boldsymbol{X}_2)\psi_i(\boldsymbol{X}_2)}{r_{12}} d\boldsymbol{X}_2\right]\psi_j(\boldsymbol{X}_1) \tag{20}$$

The Fock operator ($\hat{f}$) is dependent on the wavefunction of all the electrons within the system. To solve the Hartree-Fock equations, the molecular orbitals (ψ_i) can be expressed as linear combinations of atomic orbitals (LCAOs) known as basis functions according to equation 21.

$$\psi = \sum_{\mu} c_{\mu i}\phi_\mu \tag{21}$$

Substitution of the linear combination of atomic orbitals into equation 17 and multiplication of the left by a second basis function results in a set of equations which can be represented in a matrix form, known as the Roothaan-Hall Hartree-Fock equations.[32, 33]

$$\boldsymbol{FC} = \boldsymbol{SC}\epsilon \tag{22}$$

The term $\boldsymbol{F}$ corresponds to the matrix formed from the Fock operator, $\boldsymbol{S}$ represents the matrix of the overlap integrals, ϵ is a diagonal matrix of the orbital energies, and $\boldsymbol{C}$ is the matrix of the coefficients. In order for the Hartree-Fock equations to be solved, an initial guess of the wavefunction is performed to calculate the Coulomb and exchange integrals to obtain an initial estimate for the Fock operator ($\hat{f}$). Subsequently, the process is repeated using the newly obtained wavefunctions until each calculation cycle causes the energies and wavefunctions to remain unchanged to within a specified criterion in an iterative self-consistent field (SCF) process.

2.3 Basis Sets

Basis sets are a set of functions (basis functions) used to mathematically represent the molecular orbitals. Basis functions are usually centred on the nuclei of a given molecule, and the coefficients ($c_{\mu i}$) are used to represent how much the atomic orbital (ϕ_{μ}) represented by the basis function contributes to the molecular orbital (ψ), shown in equation 21. In the orbital approximation, the coefficients ($c_{\mu i}$) are determined via the SCF procedure where the optimal values are obtained through using the variational method (equation 7) to minimise the energy of the system.

During the early development of quantum chemistry, atomic orbitals were referred to as Hartree-Fock orbitals of separate individual atoms. There are two common types of basis functions used in the construction of molecular orbitals, so-called Slater-type orbitals (STOs) and Gaussian type orbitals (GTOs). Slater-type orbitals accurately describe the features of hydrogenic orbitals, however they lack radial nodes. STOs have a radial dependency in the form $e^{-\alpha r}$ and possess a cusp at $r = 0$. However, from a computational prospective, the majority of the numerical integrals required during the SCF procedure significantly reduces the speed of the computation and hence efficiency. However, new methods which allow efficient SCF calculations using STOs have recently been implemented. STOs can be approximated using linear combination of Gaussian type orbitals (GTOs). [34] The distinct difference between the two basis functions is that the variable r in the exponential function for GTOs is squared (GTOs possess a radial dependency in the form $e^{-\alpha r^2}$) in comparison to STOs which have a radial dependency in the form $e^{-\alpha r}$. As GTOs are rounded at $r = 0$ and

experiences a slow exponential decay, GTOs do not accurately describe radial behaviour of atomic orbitals. However, two-electron integrals are much quicker to compute with GTOs and thus have been widely adopted in quantum chemistry. Most quantum chemistry calculations use contracted GTOs basis functions wherein a linear combination of GTOs is used as a basis function, where the coefficients and exponents are fixed.

The greater the number of basis functions used in a basis set during a quantum chemical calculation on a given system, the lower the energy is obtained. However, the use of large basis sets requires significant computational costs thus basis sets that require less computation time and simultaneously provides an accurate description of molecular orbitals are commonly used. The different types of basis sets include; minimal-type basis sets in which one basis function is used for each atomic orbital, whereas a double-zeta and triple-zeta type basis set possess two and three basis functions per atomic orbital, respectively. However, the most widely used basis sets in quantum chemistry are Split Valence (Pople) and Dunning basis sets.[38 – 41]

The Nobel Laureate, John Pople developed Split-Valence (Pople) basis sets which contain only one basis function for each core atomic orbital and several basis functions for valence atomic orbitals. An example of a simple split-valence double-zeta basis set is the 6-31G basis set in which the core orbital is a contracted Gaussian type orbital (CGTO) that is built from six Gaussians. The valence orbitals are described by two functions which are constructed from three Gaussians and one single Gaussian, respectively. This basis set is referred to as a double-zeta type as the valence orbitals are separated by inner and outer orbitals. Similarly, the 6-311G basis set is triply split in which the valence orbitals are represented by three functions; the inner valence orbital is constructed from three Gaussians whereas the middle and outer valence orbitals are constructed from a single Gaussian each. Thus triply basis sets therefore describes the valence orbitals more accurately than double-zeta type basis sets in quantum chemical calculations.

The inclusion of additional basis functions, so-called polarisation functions to Split-Valence (Pople) basis sets can improve the description of molecular orbitals. Polarisation functions are essential for an accurate description for the bonding between atoms as the presence of an additional atom distorts the electron's environment and removes its spherical symmetry. For example, an s orbital can polarise in one direction if mixed with a p orbital and similarly, p orbitals can polarise if mixed with d orbitals.

The addition of polarisation functions to basis sets allows the electron distribution to become polarised, allowing molecular orbitals to become asymmetric relative to the nucleus and hence describes the valence orbitals more accurately. For a basis function with a highest angular momentum l, to be polarised the addition of "*" to the basis set (6-31G*) adds an extra set of functions of higher angular momentum $(l + 1)$ to the valence orbitals. Another common addition to Split-Valence (Pople) basis sets are diffusion functions, denoted by a plus sign "+". Diffuse functions accurately describe the 'tail' part of atomic orbitals which are distant from atomic nuclei. Diffuse functions are necessary for Rydberg states (an atom or molecule in which an electron has been excited to a high principle quantum number orbital), anions and very electronegative atoms (such as fluorine and oxygen). Two pluses, "++" and two asterisk signs "**" are used to indicate that diffuse functions are also added for the light elements, hydrogen and helium.

Other commonly used basis sets in quantum chemistry are the Dunning's correlation-consistent basis sets. The general nomenclature used for Dunning's correlation-consistent basis sets is cc-pVNZ where N = D, T, Q… (double-zeta, triple-zeta and quadruple-zeta…). The 'cc-p' term stands for 'correlation consistent polarised' and the V indicates the valence part is polarised. A prefix of 'aug' can be added to the nomenclature to indicate one set of diffuse functions (which accurately describe the 'tail' part of atomic orbitals which are distant from atomic nuclei) is added for every angular momentum (l) present in the basis set.

2.4 Beyond Hartree-Fock

2.4.1 Electron Correlation

In Hartree-Fock theory, significant simplifications are made in the calculation of a molecule's electronic structure since it assumes that each electron moves in an average electronic potential due to other electrons present within the system. According to Coulomb's law, electrons repel each other with an energy that is proportional to r_{ij}^{-1}. However, Hartree-Fock theory replaces the correlated electron repulsion interactions with an average electron charge cloud. Electron correlation for the electrons that

possess opposite spins are totally neglected, however correlation between electrons with parallel spins are accounted for. These assumptions made in Hartree-Fock theory introduce errors in the wavefunction and energy. The error in the energy is referred to as the correlation energy, where the total correlation energy can be quantified by the difference between the nonrelativistic exact energy (ε_{exact}) and the Hartree-Fock limit energy (E_{HF}^{∞}) in a complete basis, as shown in equation 23.

$$E_{corr} = \varepsilon_{exact} - E_{HF}^{\infty} \tag{23}$$

The assumptions made in Hartree-Fock theory (as discussed above) can lead to significant deviations from experimental results, thus a number of methods, referred to as post Hartree-Fock methods have been developed to account for electron correlation. To include correlated electron repulsion interactions in a more accurate manner than Hartree-Fock theory, methods such as Møller-Plesset perturbation theory and coupled cluster theory have been devised.

2.4.2 Møller-Plesset Perturbation Theory

In 1934, Christian Møller and Milton S. Plesset described how Hartree-Fock method can incorporate correlated electron repulsion interactions by using second order perturbation theory.[42] This method is known as Møller-Plesset perturbation theory and is abbreviated to as MP*n* (*n* = 2, 3, 4…), where *n* is the order at which the perturbation is truncated. Møller-Plesset perturbation theory is not variational as the calculated energy of a given chemical system can be lower than the actual ground state energy. The theory is founded on the concept that the energy corrections can be obtained through the inclusion of a perturbating operator ($\widehat{H}'$), shown in equation 24.

$$\widehat{H} = \widehat{H}^0 + \widehat{H}' \tag{24}$$

The term $\widehat{H}$ and $\widehat{H}^0$ is the full electronic Hamiltonian and unperturbed Hamiltonian, respectively. Taylor series expansions can be utilised to represent the wavefunction and hence energy of the system that can be truncated at a specified order. The second order

truncation, so-called MP2 is the first of the MP*n* methods that improves on the Hartree-Fock method where the energy is represented in equation 25.

$$E_{MP2} = E_{HF}^{total} + E_0^2 = E_{HF}^{total} + \frac{1}{4}\sum_{abyz} \frac{|\langle ab|xy\rangle - \langle ay|bz\rangle|^2}{\epsilon_y + \epsilon_z - \epsilon_a - \epsilon_b} \quad (25)$$

In equation 25, the terms a and b represent unoccupied orbitals whereas terms y and z represent occupied orbitals and ϵ corresponds to the energy of the occupied/unoccupied orbitals. MP*n* (n = 2, 3, 4…) methods can be implemented in various computational chemistry codes, however higher level Møller-Plesset calculations (up to MP5) are possible but rarely applied in studying the electronic structure of chemical systems due to high computational costs. Conversely MP2 level accounts for around 80% of correlation energy and requires significantly less computational time in comparison to other higher levels of theory, making it one of the most widely used methods in quantum chemistry for studying weak dispersion forces.[60]

2.4.3 Coupled Cluster Theory

Another commonly used post Hartree-Fock method is the Coupled Cluster (CC) theory. The CC method is based upon a many-determinant wavefunction which is constructed using the exponential cluster operator. Despite the demanding computational time required for the calculation, CC is a widely used method to investigate complex chemical systems.

$$\Psi_{CC} = \exp^T \Psi_{HF} \quad (26)$$

$$e^T = 1 + T + \frac{1}{2!}T^2 + \frac{1}{3!}T^3 \ldots \quad (27)$$

The equations show the wavefunction is expressed as a linear combination of Slater determinants, where each of the additional determinants corresponds to where one or more electrons have been excited from an orbital occupied in the HF ground state to an unoccupied orbital. However due to computational costs, it is not practical to include

all excitations, hence the CC method (similar to Møller-Plesset perturbation theory) can be truncated. Second order truncation of the linear combination of Slater determinants allows consideration for single and double excitations. Similarly, third order truncations are where triple excitations are accounted for in addition to single and double excitations. In general, as the number of excitations included in the wavefunction increases, the energy of the wavefunction determined from the calculation becomes increasingly accurate, however computational costs also rise with increasing number of excitations. As a result, a method referred to as CCSD(T) has been implemented which approximates the contribution of triple excitations using perturbative methods. The CCSD(T) method is considered to be a benchmark in quantum chemical calculations, thus this method will be used in this investigation to act as a point of reference for the results obtained from other levels of theory.[43, 44]

2.5 Density Functional Theory

2.5.1 Electron Density

Hartree-Fock method does not account for electron correlation and as a result, an overestimation for the energy of the chemical system being studied occurs. Therefore, post Hartree-Fock methods have been devised to account for correlated electron repulsion interactions, however such methods require significant computational effort and time. As a result, an alternative technique that is not solely dependent on the wavefunction is required to avoid demanding computational costs.

Density functional theory (DFT) has become one of the most widely used techniques in the calculation of molecular structure and now approximately 90% of all quantum chemical calculations use DFT in study of chemical systems. DFT provides a method that includes electron correlation at relatively low computational costs and in most cases (especially for *d*-metal complexes) provides better agreement with experimental values than Hartree-Fock theory.

In DFT, the central focus is on electron density (ρ) rather than the N-electron wavefunction. The term 'functional' in DFT is originated from the fact the energy of a molecule is a function of electron density, $E[p]$ (equation 28), where the electron

density can be obtained from calculating the integral over the spin coordinates of all electrons and over all but one of the spacial variables, as shown in equation 29.

$$E[\rho] = E_K + E_{P;e,N} + E_{P;e,e} + E_{XC}[\rho] \tag{28}$$

$$\rho(\boldsymbol{r}) = \int |\Psi(\boldsymbol{r}, \boldsymbol{r}_2, \boldsymbol{r}_3 \dots \boldsymbol{r}_N)|^2 d\boldsymbol{r}_2 d\boldsymbol{r}_3 \dots d\boldsymbol{r}_N \tag{29}$$

In equation 28, the term E_K corresponds to the total kinetic energy of the electron, $E_{P;e,N}$ represents the electron-nucleus potential energy, $E_{P;e,e}$ is the electron-electron potential energy and $E_{XC}[p]$ is the exchange-correlation energy which includes all other effects including the exchange energy and correlation energy. The electron density contains valuable information as it corresponds to the probability of locating any of the N electrons within the volume ($d\boldsymbol{r}$). As a result, the total number of electrons and the nuclear positions within a given chemical system can be deduced from the integral and maxima of the electron density, respectively.

$$\int \rho(\boldsymbol{r}) d\boldsymbol{r} = N \tag{30}$$

Electron density is a function that can be experimentally measured using X-ray crystallography. In quantum chemistry, DFT offers a main advantage over post-HF methods (including Møller-Plesset perturbation theory and coupled cluster method) as it incorporates correlated electron repulsion interactions and simultaneously requires less demanding computational effort.

2.5.2 Hohenberg Kohn Theorems

In 1964 Hohenberg and Kohn proposed two theorems, so-called first Hohenberg-Kohn and second Hohenberg-Kohn theorem, both at which forms the basis of DFT.[45, 46] In the first Hohenberg-Kohn theorem (HK1), the energy of the electrons that move under the influence of a potential field, caused by the nuclei within the system, can be obtained from the ground-state electron density (ρ_0) and hence the

Hamiltonian can be deduced. From solving the electronic Schrödinger equation, a unique wavefunction, which possesses all the information about the chemical system can be deduced. Conversely, the second Hohenberg-Kohn theorem (HK2) is formed by applying the variational theorem to the electron energy, shown in equation 31.

$$E = E[\rho] = \int \rho(\boldsymbol{r}) v_{nuc}(\boldsymbol{r}) d\boldsymbol{r} + F_{HK}[\rho] \tag{31}$$

As previously mentioned, the term $E[\rho]$ is an energy functional. HK2 theorem states the exact ground state energy (E_0) is always less than, or equal to the energy obtained from the trial (arbitrary) electronic density, $\tilde{\rho}$, mathematically represented in equation 32.

$$E_0[\rho] \leq E[\widetilde{\rho}] \tag{32}$$

2.5.3 Kohn-Sham DFT

As previously discussed, pure DFT computes the energy of a given system as a function of electron density. However, it is not an accurate method due to the lack of accurate approximations for the kinetic energy functional. Consequently, Walter Kohn and Lu Jeu Sham in 1965 devised an alternative approach to overcome the issue where they suggested a given chemical system can be represented by a system of non-interacting electrons.[47] The non-interacting system is constructed such that its electron density is the same as that of the interacting electrons. Summation of the electron kinetic energy and potential energies of the nuclear-electron and electron-electron interactions gives the energy of the non-interacting system, as shown in equation 33. The following terms $T_s[\rho]$, which represents the kinetic energy of the non-interacting electrons and $J[\rho]$, which corresponds to the Coulomb repulsion between the electrons can be incorporated into equation 33 to form equation 34.

$$E = E[\rho] = V_{ne}[\rho] + T[\rho] + V_{ee}[\rho] \tag{33}$$

$$E[\rho] = V_{np}[\rho] + T_s[\rho] + J[\rho] + (T[\rho] - T_s[\rho] + V_{ee} - J[\rho]) \tag{34}$$

$$E[\rho] = V_{np}[\rho] + T_s[\rho] + J[\rho] + E_{XC}[\rho] \tag{35}$$

$$E_{XC}[\rho] = (T[\rho] - T_s[\rho]) + (V_{ee} - J[\rho]) \tag{36}$$

In equation 34, all four unknown parts ($T[\rho] - T_s[\rho] + V_{ee} - J[\rho]$) can be incorporated into a relatively small exchange-correlation functional term $E_{XC}[\rho]$, as seen in equation 35. In the exchange-correlation functional, (equation 36) the $T[\rho] - T_s[\rho]$ term corresponds to the difference between the non-interacting and interacting kinetic energies, whereas the $V_{ee} - J[\rho]$ term corresponds to the non-classical electron-electron interaction. In a Kohn-Sham calculation, the electron density is obtained by minimising the energy according to equation 38.

$$E[\rho(\mathbf{r})] = T_s[\rho(\mathbf{r})] + \int v_{ext}(\mathbf{r})\rho(\mathbf{r})d\mathbf{r} + \int \frac{\rho(\mathbf{r}_1)\rho(\mathbf{r}_2)}{|\mathbf{r}_1 - \mathbf{r}_2|} d\mathbf{r}_1 d\mathbf{r}_2 + E_{XC}[\rho(\mathbf{r})] \tag{38}$$

The fact that the electron densities arise from a Slater determinant wavefunction (Ψ_{SD}) ensures the electron density (ρ) corresponds to a valid wavefunction. The Slater determinant wavefunction (Ψ_{SD}) is built from Kohn-Sham orbitals (ψ_i) which are one-electron wavefunctions. From solving the Kohn-Sham equations, solutions to the one-electron wavefunctions can be deduced, as shown in equation 39.

$$\left[-\frac{1}{2}\nabla_i^2 + V_{eff}(\mathbf{r})\right]\psi_i = \epsilon_i\psi_i \tag{39}$$

The term $V_{eff}(\mathbf{r})$, shown in equation 39 is the effective potential of the non-interacting system. Solutions to the one-electron wavefunctions can be achieved through selecting $V_{eff}(\mathbf{r})$ such that the ground state energy of the non-interacting system is the same as that of the real system.

$$V_{eff}(\mathbf{r}) = V_{ext} + \int \frac{\rho(\mathbf{r}_2)}{r_{12}} d\boldsymbol{r}_2 + V_{XC} \tag{40}$$

$$V_{eff}(\mathbf{r}) = \sum_A \frac{Z_A}{r_{1A}} + \int \frac{\rho(\mathbf{r}_2)}{r_{12}} d\boldsymbol{r}_2 + \frac{\delta E_{XC}[\rho]}{\delta \rho} \tag{41}$$

$$\rho_0(\mathbf{r}) = \rho_s(\mathbf{r}) = \sum_i^N |\psi(\mathbf{r})|^2 \tag{42}$$

In order to calculate the effective potential of the non-interacting system, $V_{eff}(\mathbf{r})$, an initial guess for the electron density $\rho(\mathbf{r})$ is carried out. Subsequently, the Kohn-Sham equations are then solved in order to obtain a more accurate value for the electron density. The newly calculated electron density can be utilised to obtain a more accurate value for the effective potential of the non-interacting system, $V_{eff}(\mathbf{r})$. This procedure, referred to as the Kohn-Sham self-consistent field method, is an iterative process and continues until the specified convergence criterion is met. To calculate the effective potential of the non-interacting system, $V_{eff}(\mathbf{r})$, the exchange-correlation functional, V_{XC} is necessary, and from equation 41, it is apparent $V_{eff}(\mathbf{r})$ is dependent upon the exchange correlation energy, E_{XC}. The exchange correlation energy does not contribute significantly to the total energy of the chemical system; however, it is still vital for quantum chemical calculations, and as a consequence, numerous methods have been devised to approximate E_{XC} to a high accuracy.

2.5.4 Exchange Correlation Functionals

Early attempts at the exchange-correlation functionals were based upon simple model systems for which the exchange and correlation could be derived. The simplest model (introduced in 1965 by Walter Kohn and Lu Jeu Sham)[47], referred to as Local Density Approximation (LDA) assumes the electron density is uniform across all space. As represented in equation 43, the LDA exchange-correlation functional, $E_{XC}^{LDA}[\rho]$ is dependent upon the electron density at position **r** only.

$$E_{XC}^{LDA}[\rho] = \int \rho(\mathbf{r})\, \epsilon_{XC}(\rho) d\mathbf{r} \tag{43}$$

The term $\epsilon_{XC}(\rho)$ represents the exchange-correlation energy for each particle in a homogenous electron gas. However, the term $\epsilon_{XC}(\rho)$ can be separated into contributions for both the exchange and correlation. However, Walter Kohn and Lu Jeu Sham stated an "accurate description of chemical bonding" is not expected from the Local Density Approximation as the electron distribution can vary throughout a chemical system.[47] In reality, covalent, ionic and metallic bonds are surprisingly accurately described, however the LDA model fails to describe van-der-Waals and hydrogen bonds well. Metallic systems are also well described by LDA since such systems resemble a uniform electron gas.

As LDA approximates the energy of the true electron density within a system through assuming the electron density is uniform across all space, it fails in situations where the electron density undergoes rapid changes such as in molecules. Consequently, an improvement to LDA can be made through considering the gradient of the electron density, so-called the Generalised Gradient Approximation (GGA). GGA functionals attempt to account for the non-uniform electron density through including electron density and the gradient of the electron density (∇_ρ) into the functional, as shown in equation 44.

$$E_{XC}^{GGA}[\rho] = \int \rho(\mathbf{r})\, \epsilon_{XC}\left(\rho, |\nabla_\rho|\right) d\mathbf{r} \tag{44}$$

GGA functionals are essentially built from LDA functionals with the inclusion of a correction that is based on the gradient of the electron density (∇_ρ). Examples of GGA functionals include PW91, PBE and BLYP. Similarly, an improvement to GGA functionals can be made through the inclusion of the second derivative of the electron density (∇_ρ^2), so-called meta-GGA.

Hybrid functionals are another class of exchange-correlation functionals that often provides more accurate predictions for bond lengths, angles and harmonic frequencies. Such functionals include some component of exact Hartree-Fock exchange with other exchange and correlation from different sources. The most famous example of a hybrid functional is the B3LYP functional, shown in equation 45.[48]

$$E_{XC}^{B3LYP} = (1-a)E_X^S[\rho] + aE_X^{HF} + bE_X^{B88}[\rho] + cE_C^{LYP}[\rho] + (1-c)E_C^{VWN}[\rho] \quad (45)$$

Where a = 0.20, b = 0.72 and c = 0.81. The values can be altered such that the percentage of Hartree-Fock exchange in the functional can be varied.

2.5.5 Dispersion Interactions

For many problems, DFT provides sufficiently accurate results at an acceptable computational cost, however the theory does possess some significant deficiencies. For example, DFT will describe hydrogen bonded systems such as $(H_2O)_2$ well but will fail to accurately describe large systems such as the benzene dimer. This is a result of Kohn-Sham DFT (with standard functionals) not possessing dispersion interactions. In larger systems, such as biological systems, weak dispersion forces become more significant. The most common approach to account for dispersion interactions in DFT is to include an empirical dispersion correction term (E_{DISP}) to the energy obtained from the DFT calculation (E_{DFT}). As a result, the corrected DFT energy, E_{DFT-D} (expressed in equation 46) can be obtained.

$$E_{DFT-D} = E_{DFT} + E_{DISP} \quad (46)$$

where

$$E_{DISP} = -\sum_{A>B}^{atoms} f_{AB}(R_{AB}) \frac{C_6^{AB}}{R_{AB}^6} \quad (47)$$

The term C_6^{AB} are dispersion coefficients, defined by each pair of atoms A and B, where R_{AB} is the distance between both atoms. The $f_{AB}(R_{AB})$ term is a damping function which assists in avoiding double counting effects such that $f_{AB} = 0$ for small values of R_{AB} and $f_{AB} = 1$ for large values of R_{AB}. The inclusion of an empirical dispersion correction term (E_{DISP}) to the energy obtained from DFT calculations (E_{DFT}) provides a large improvement for the description of large chemical systems.

2.6 Optimisation Methods

2.6.1 Geometry Optimisation

The geometry optimisation procedure allows minima and first order saddle points on the potential energy surface which correspond to equilibrium geometries and transition-state structures, respectively, to be determined. This procedure is an iterative process which requires calculation of energies and gradients at each optimisation cycle until the specified convergence criterion is met. During the optimisation step, the trial molecular geometry is modified and the current and previous energy, gradient and hessian information is utilised such that a new molecular geometry that is closer to the target stationary point is deduced. When investigating molecular clusters, as the number of molecules within the system increases, the number of minima on the potential energy surface also increases. Consequently, it becomes increasingly challenging to find the global minimum on the potential energy surface which corresponds to the most stable molecular configuration. Therefore, an algorithm is essential to ensure the entire potential energy surface is examined. In this study, a random movement search procedure will be employed to determine the lowest energy molecular structures.

2.6.2 Random Movement Search

The random movement (RM) search is a procedure that can be employed to examine the potential energy surface in order to determine all low energy isomers of a given chemical system. In the random movement search procedure, an initial random set of coordinates undergo geometry optimisations, usually performed at a low level of theory such as Hartree-Fock theory level with a low basis set. This results in an initial structure which can be modified where a specified number of atoms/molecules undergo random movements in space. During the random movement, the given chemical system is subjected to a specified number of random moves in which an atom/molecule is chosen at random, translated and rotated by a random angle. The distance the atoms/molecules are displaced during the random moves is controlled through setting a box size which prevents them from being displaced too far away from each other.

Similarly, a minimum separation and maximum displacement between the atoms/molecules is set during the random moves to prevent them from being projected too close or far from each other. If a random move results in any of atoms/molecules in the system to be translated outside the specified box size, or closer than the minimum specified separation, the move will be rejected resulting in an SCF convergence failure. The molecules are then randomly positioned within the specified box size again, starting from the initial structure (that was optimised using a low level of theory) creating a new set of coordinates that further undergo geometry optimisations. The cartesian coordinates of the low energy optimised structure, obtained from the RM search procedure is then recorded. Subsequently, the procedure is then repeated N times resulting in a total of $N + 1$ low energy isomers. As the moves during the RM search procedure are completely random, the procedure ensures the entire potential energy surface, for a given chemical system is examined provided that N is sufficiently large.

2.7 Computing Vibrational Frequencies

From considering the nuclear Schrödinger equation (equation 48), the vibrational frequencies of a given molecular geometry can be calculated which would allow characterisation for the nature of the stationary point. Theoretical IR spectra can also be deduced from calculated vibrational frequencies and intensities; hence a comparison can be made against experimental IR spectra to assess the validity of the predicted molecular geometry. In order to calculate the vibrational frequencies and vibrational modes, the nuclear Schrödinger equation can be approximated using the harmonic approximation, as shown in equation 50.

$$\left[-\sum_{A}\frac{1}{2M_A}+V(x)\right]\Psi_{nuc}=E_{nuc}\Psi_{nuc} \tag{48}$$

$$V(\boldsymbol{x})\approx V(\boldsymbol{x}_o)+\left(\frac{dV}{d\boldsymbol{x}}\right)(\boldsymbol{x}-\boldsymbol{x}_o)+\frac{1}{2}\left(\frac{d^2V}{d\boldsymbol{x}^2}\right)(\boldsymbol{x}-\boldsymbol{x}_o)^2 \tag{50}$$

where at a stationary point

$$V(\boldsymbol{x}) \approx \frac{1}{2}\left(\frac{d^2V}{d\boldsymbol{x}^2}\right)(\boldsymbol{x}-\boldsymbol{x}_o)^2 \tag{51}$$

The vibrational frequencies and normal modes are obtained from the eigenvalues and eigenvectors of the mass-weighted Hessian matrix. The mass-weighted Hessian matrix consists of second order derivatives of the energy with respect to the coordinates of the system, shown in equation 52. The major cost of the computation lies within the evaluation of the second derivates.

$$G_{ij} = \frac{1}{\sqrt{m_i m_j}}\left(\frac{\partial^2 E}{\partial \boldsymbol{u}_i \partial \boldsymbol{u}_j}\right) \tag{52}$$

The term $\boldsymbol{u}$ in equation 52 denotes the displacement of the nuclei. As shown in equation 53, the eigenvalues of the mass-weighted Hessian matrix are in a direct relationship to the harmonic vibrational frequencies.

$$\nu_k = \frac{\lambda_k^{1/2}}{2\pi} \tag{53}$$

The term λ_k are the eigenvalues and the ν_k term represents the vibrational frequencies. In order for a given molecular structure to correspond to an equilibrium geometry on the potential energy surface, all the eigenvalues must be positive. However, if one eigenvalue is negative, it signifies an imaginary frequency present which implies the given molecular structure corresponds to a transition state structure on the potential energy surface. Due to the fact that computed harmonic vibrational frequencies are systematically too high, scaling factors are commonly employed to account for the effects of anharmonicity. Computing anharmonic vibrational frequencies is an alternative approach that can be employed to increase accuracy as the use of a single scaling factor is not appropriate for all vibrational modes. However, anharmonic frequency calculations are rarely computed as DFT based anharmonic frequencies are of similar accuracy to scaled harmonic DFT frequencies and the additional accuracy does not justify the vast increase in computational cost. Anharmonic frequency calculations are computationally demanding as third and fourth derivatives of the

energy are necessary for such calculations. Therefore, in this investigation, harmonic vibrational frequencies will be computed with the use of approximate scaling factors.

In the harmonic approximation, the allowed vibrational energies for a simple harmonic oscillator for a diatomic molecule is expressed by equation 54, where v is the vibrational quantum number, E_v is the energy for that vibrational quantum state, ω_e is the vibrational frequency, k and μ is the force constant and reduced mass, respectively. The specific selection rule for a simple harmonic oscillator is given by equation 55.

$$E_v = \left(v + \frac{1}{2}\right) h\omega_e \qquad \omega_e = \frac{1}{2\pi}\left(\frac{k}{\mu}\right)^{1/2} \qquad v = 0, 1, 2, \ldots \tag{54}$$

$$\Delta v = \pm 1 \tag{55}$$

From the harmonic oscillator model, the vibrational energy levels are equally spaced. The gaps between the vibrational energy levels are large and from the Boltzmann distribution, it can be seen most molecules reside in the vibrational v = 0 state at room temperature. The most frequently observed transition in a spectrum is therefore the fundamental, that corresponds to a 1 ← 0 change in vibrational state. Therefore, even when a molecule resides in the ground state (v = 0), from equation 54, it can be seen the system still possesses some energy. The lowest vibrational energy level (v = 0) has an energy of $\left(\frac{1}{2} h\omega_e\right)$, which is referred to as the zero-point energy (ZPE). The addition of the zero-point energy (ZPE) can be used to account for the difference between the ground state energy and the energy at the bottom of the potential energy surface. In computational chemistry, more accurate energies are obtained through the inclusion of ZPE corrections to the electronic energy of the chemical system, hence better comparisons can be made against experimental values.

2.8 Basis Set Superposition Error (BSSE)

The binding energy between two species (A and B) can be computed through deducing the difference between the energy of their associated form (AB) and the energies of the individual species (A and B), shown in equation 56:

$$\Delta E_{int}(AB) = E^{AB}(AB) - E^{A}(A) - E^{B}(B) \quad (56)$$

where the superscripts represent the basis functions used. However, when binding energies are computed, the energies of the individual species are overestimated. As the two individual species approach each other, their basis functions overlap which causes the complex AB to be artificially stabilised as species A exploits the extra basis functions possessed from species B (or vice versa). Consequently, the basis set size is increased which improves the description for electron distribution. As a result, more basis functions are available for both species A and B when complexed in comparison to when they are in their individual forms and infinitely separated. As a result, equation 56 overestimates the binding energy and this phenomenon is referred to as basis set superposition error which is an artefact of using finite basis sets. This error is resolved though using the counterpoise correction (equation 57).[49]

$$\Delta E_{int}(AB) = E^{AB}(AB) - E^{AB}(A) - E^{AB}(B) \quad (57)$$

The counterpoise correction evaluates the energy of species A in the AB complex through placing all the basis functions of species B on the atomic centres of species B while neglecting the electrons and nuclear charges of monomer B, or vice versa. Such functions on species B are referred to as ghost functions. Through using the counterpoise correction, a more accurate binding energy can be established.

3. Computational Methodology

The lowest energy structures of $O_2^+ \cdot (H_2O)_n$ with n within the range of 1 – 5 were calculated using a hierarchical procedure where a lower level of theory was used to search the conformational space and identify low energy isomers. The identified low energy isomers were then re-optimised at a higher level of theory. This approach has been used successfully in the study of related systems. [50, 51]

In this investigation, the conformational search was performed using unrestricted HF with the 6-31+G* basis set with a random movement (RM) search approach. For each cluster, 12 separate RM searches were performed in which all RM searches possessed different starting geometries. In this approach after an initial geometry optimization, the oxygen and water molecules in the molecular cluster were subjected to 20 random moves which include translations and rotations and the resulting structure was then re-optimised. The structural moves were subjected to the constraints that the atoms are kept separated by a least 0.2 bohr at the point of closest contact and the molecules are kept within a box of length 10 bohr. This procedure was repeated 100 times to give a total of 101 (including the initial) structures. The structural searches were performed for both doublet and quartet spin states. The low energy structures obtained from the RM search were categorised by visual inspection. The distinct low energy structures were then re-optimised at the unrestricted MP2/6-311++G** level of theory and harmonic vibrational frequencies were computed to determine the nature of the stationary point. This level of theory was chosen due to past success at describing the structure of similar atmospheric cluster ions in the literature.[21]

Theoretical IR spectra were calculated for the lowest energy structures of each $O_2^+ \cdot (H_2O)_n$ cluster ion. The computed harmonic frequencies were scaled by 0.95 and in the simulated spectra, the vibrational bands were represented by Lorentzian functions with full-width at half-maximum of 10 cm^{-1}. The computed spectra have been normalized such that the intensity of the most intense band is equal to one. Binding energies were computed subject to the counterpoise correction (performed with the individual moieties frozen at their optimised geometries in the complex) and atomic charges and spin were calculated from natural bonding orbital (NBO) analysis.

Born-Oppenheimer AIMD simulations were performed at the MP2/6-31+G* level of theory at a temperature of 220 K (which is representative of the temperature in

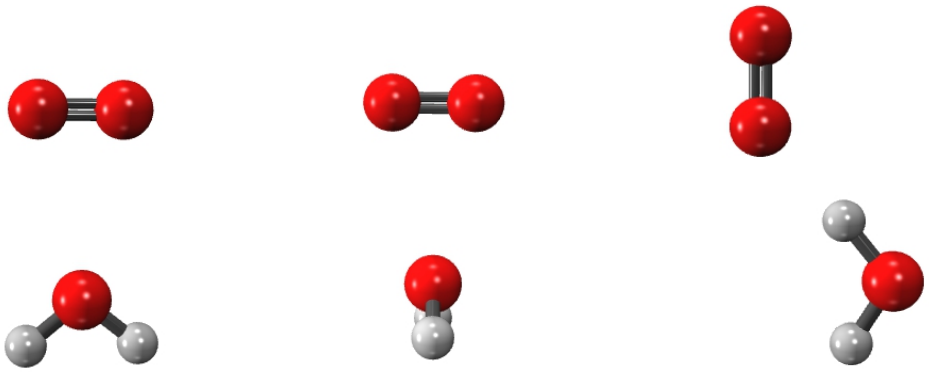
the D-region of the ionosphere) and initial velocities were sampled from the Maxwell-Boltzmann distribution. For the $O_2^{+}\cdot(H_2O)_n$ (where $n = 2 – 5$) cluster ions, a time step of 0.484 fs was used with a total simulation time of 4.84 ps, and the dynamics were run for the quartet spin state. The initial structures consisted of O_2^{+} with n undissociated water molecules in a configuration where the position of the oxygen atoms corresponded to the lowest energy structures obtained from the random search procedure since for $n \geq 2$, the lowest energy structures have the form $O_2\cdot(H_2O)_{n-2}\cdot H_3O^{+}\cdot OH$. Born-Oppenheimer AIMD simulations were also performed for the $NO^{+}\cdot(H_2O)_n$ ($n = 4 – 5$) cluster ions but with a significantly longer total simulation length of 9.676 ps and initial structures of the lowest energy structure of the clusters. For these clusters, simulations were performed using MP2 and a range of basis sets. Collision dynamics simulations of an association of a water molecule onto $NO^{+}\cdot(H_2O)_4$ to form $NO^{+}\cdot(H_2O)_5$ was performed at the MP2/6-311++G** level of theory to deduce whether the resulting activated complex, with excess energy, would be more susceptible to forming nitrous acid and a protonated water cluster which have been experimentally observed in the D-region of the ionosphere.

All quantum chemical calculations performed in this investigation were carried out using the Q-CHEM 5.0 software package, visual analysis was performed using IQ-mol and all plots produced were carried out in GNUPLOT.[24]

4. Results and Discussion

4.1 Benchmarking

4.1.1 $O_2^{+\cdot}(H_2O)$



(A) (B) (C)

Figure 1: Minimum energy geometries of $O_2^{+\cdot}(H_2O)$ in the doublet (1A and 1B) and quartet spin state (1C), optimised at the MP2/6-311++G** level of theory.

From performing 12 separate RM searches for the doublet spin state (using unrestricted HF with the 6-31+G* basis set), two low energy structures of $O_2^{+\cdot}(H_2O)$ cluster ions (Figures 1A and 1B) were obtained which were then re-optimised at the MP2/6-311++G** level of theory. Harmonic vibrational frequency calculations confirmed both structures corresponded to true minima on the potential energy surface as no imaginary frequencies were present. Note that zero-point energy corrections were not accounted for.

Two distinct minima can be identified for the $O_2^{+\cdot}(H_2O)$ complex corresponding to planar (1A) and non-planar (1B) orientations of the water molecule. The energy difference between structures 1A and 1B was found to be 2.6 kJ mol^{-1}, suggesting that the structures are of comparable stability. The energy difference between these two minima is small, but high-level calculations confirm that the planar structure has the lowest energy. The findings from this investigation suggests an interconversion

between structures 1A and 1B is highly likely at D-region ionospheric temperatures due to the small energy difference between the two minima on the potential energy surface.

The lowest energy cluster for n = 1 corresponds to a complex of a water and oxygen diatomic cation in a doublet spin state (Figure 1A). The lowest energy structure of $O_2^+ \cdot (H_2O)$ obtained from this study can be compared to previous theoretical studies where geometry optimisations have also been carried out on the complex at various levels of theory where in each case, a large spin contamination was observed for a doublet state.[12] However, in this study, a value of $\langle S^2 \rangle$ = 0.76 for the calculation and the structure of the cluster found in this investigation is significantly different with the oxygen atom of water much closer to one of the oxygen atoms of the diatomic cation.

12 separate RM searches were also performed on the $O_2^+ \cdot (H_2O)$ complex in the quartet spin state. However, it was found the lowest energy structure, shown in Figure 1C lies around 150 kJ mol^{-1} higher in energy when compared against the lowest energy doublet spin state structure (Figure 1A) even though the structure consists of a water and oxygen molecule. However, the structure of the complex is different with the water molecule binding to the oxygen molecule through a hydrogen atom rather than the oxygen atom. Table 1 shows the associated energy with the low energy doublet (Figure 1B) and quartet spin state structure (Figure 1C) and relative energies compared against lowest energy doublet spin state structure (Figure 1A).

Structure	MP2 Energy (E_h)	Relative Energy (kJ mol^{-1})
1A	-225.913882	0.00
1B	-225.912875	2.64
1C	-225.856804	149.86

Table 1: MP2 computed energies of the two low energy doublet and lowest energy quartet spin state structures.

4.1.2 Investigating Different Quantum Chemical Methods

To investigate larger $O_2^+ \cdot (H_2O)_n$ clusters ions for $n \geq 2$, a quantum chemical method that delivers an accurate description for the chemical properties such as charge distribution, dipole moment, and binding energy was required. Although CCSD(T) method is the most accurate and thoroughly developed post Hartree-Fock method at

describing the molecular properties, it requires extensive computation time making it an unsuitable method for performing theoretical calculations on larger molecular clusters. The lowest energy structure for $O_2^+ \cdot (H_2O)$, obtained from the RM search was re-optimised using coupled cluster theory, MP2 and DFT with a wide range of DFT exchange-correlation functionals to investigate their ability and efficiency at predicting the structure and molecular properties.

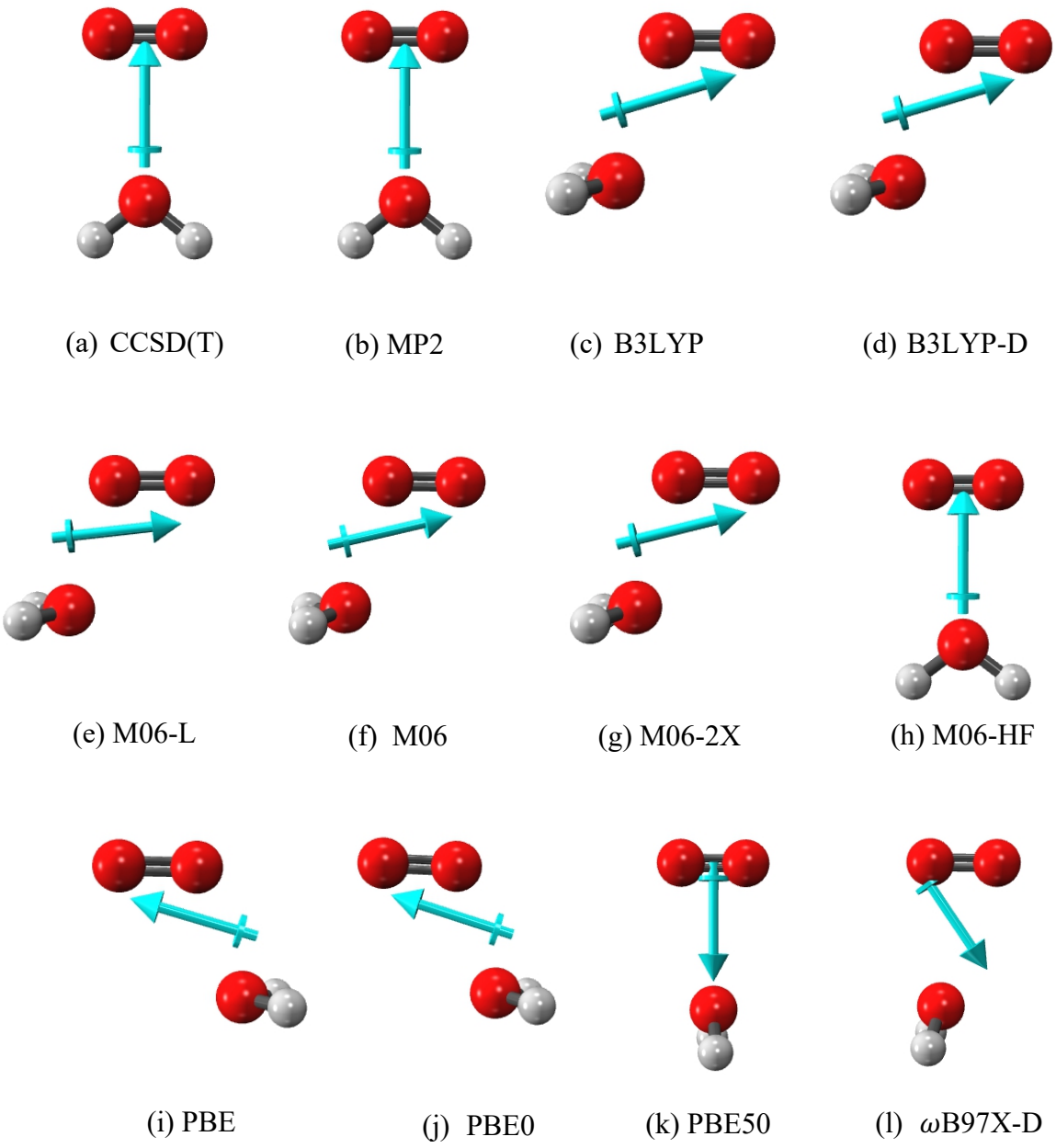


Figure 2: The structure of $O_2^+ \cdot (H_2O)$ and direction of the dipole moment predicted by CCSD(T), MP2 and a wide range of exchange-correlation functionals.

Structure 1A, obtained from the RM procedure was initially re-optimised using the B3LYP-D exchange correlation functional which is B3LYP with the inclusion of the empirical dispersion correction. Although the inclusion of the empirical dispersion correction in the functional improved the direction of the dipole moment (since it was closer towards the direction predicted by CCSD(T)), an increase in error for the binding energy was observed when compared to B3LYP results (Table 2).

Method/Functional	% HF Exchange in Functional	Binding Energy (kJ mol^{-1})	Error (kJ mol^{-1})
CCSD(T)	-	72.8	+0.0
MP2	100	73.1	+0.3
M06-HF	100	90.0	+17.2
PBE50	50	107.1	+34.3
ωB97X-D3	100	126.3	+53.5
ωB97X-D	100	128.3	+55.5
M06-2X	54	142.4	+69.7
M06	27	172.4	+99.7
PBE0	25	174.2	+101.4
B3LYP	20	174.4	+101.6
B3LYP-D	20	185.5	+112.8
M06-L	0	206.7	+133.9
PBE	0	214.4	+141.6

Table 2: Computed binding energies with the 6-311++G** basis set and difference with respect to CCSD(T) for $O_2^+ \cdot (H_2O)$ in kJ mol^{-1}.

Structure 1A was also used to obtain the binding energy between O_2^+ and H_2O in the $O_2^+ \cdot (H_2O)$ complex. Table 2 shows the computed binding energies for the doublet state of $O_2^+ \cdot (H_2O)$ for a wide range of DFT exchange-correlation functionals, MP2 and CCSD(T) with the 6-311++G** basis set. The binding energies have been computed with the counterpoise correction and the error with respect to CCSD(T) is given. It was found the binding energy computed with MP2 (73.1 kJ mol^{-1}) is in close agreement with coupled cluster value (72.8 kJ mol^{-1}). The basis set used was also an important factor as the binding energy calculated at the MP2/aug-cc-pVTZ level of theory is 78.2

kJ mol^{-1} which is about 5 kJ mol^{-1} higher than the MP2/6-311++G** value. However, the binding energy of 72.8 kJ mol^{-1} for CCSD(T)/6-311++G**, 73.1 kJ mol^{-1} for MP2/6-311++G** and 78.2 kJ mol^{-1} for MP2/aug-cc-pVTZ are all consistent with the experimental binding energy value of 77.2 kJ mol^{-1} reported in the literature.[10]

However, the binding energy between O_2^+ and H_2O predicted by B3LYP is overestimated by over 100 kJ mol^{-1}. This overestimation in the binding energy can be explained through investigating the direction of the dipole moment. The direction of the dipole moments for the $O_2^+ \cdot (H_2O)$ cluster ion calculated using CCSD(T), MP2 and a wide range of DFT exchange correlation functionals (including B3LYP) are shown in Figure 2. From comparison of the dipole moments predicted by B3LYP and CCSD(T), it is apparent B3LYP incorrectly predicts the direction of the dipole moment, hence the charge distribution is inaccurately modelled. Table 3 displays the net charge on O_2^+ and H_2O in the $O_2^+ \cdot (H_2O)$ complex modelled using CCSD(T), MP2 and a wide range of DFT exchange correlation functionals.

The charge distribution predicted using B3LYP shows the water molecule carries a positive charge of approximately +0.59e. This can be compared to the charge distribution calculated using CCSD(T) and MP2 where both methods predict the charge on the O_2^+ ion and water molecule to be +1.02e and -0.02e, respectively. The results obtained from CCSD(T) and MP2 confirm the positive charge is localised on the oxygen molecule and the water molecule is essentially neutral (see Table 3). Conversely, the charge distribution predicted by B3LYP indicates the positive charge is not fully localised on the oxygen molecule as the water molecule carries +0.41e of the positive charge. From closer inspection of the atomic charges on the water molecule in the $O_2^+ \cdot (H_2O)$ complex, it can be seen the oxygen atom carries a negative charge of -0.26e. Since the oxygen atom of the water molecule carries a negative charge, it becomes attracted to the positive charge that is localised on the oxygen molecule which causes an inaccurate prediction for the lowest energy $O_2^+ \cdot (H_2O)$ structure. Consequently, the differences in charge distribution predicted by B3LYP and CCSD(T) explains the discrepancies between the two structures. The B3LYP functional has been known to suffer from charge delocalisation due to self-interaction error. [35 – 37]

Method/Functional	% HF Exchange in Functional	Net Mulliken Charge on O_2^+	Net Mulliken Charge on H_2O
CCSD(T)	-	1.02	-0.02
MP2	100	1.02	-0.02
M06-HF	100	1.01	-0.01
PBE50	50	0.98	0.02
ωB97X-D	100	0.89	0.11
ωB97X-D3	100	0.89	0.11
M06-2X	54	0.65	0.35
M06	27	0.63	0.37
PBE0	25	0.60	0.40
B3LYP	20	0.59	0.41
B3LYP-D	20	0.59	0.41
M06-L	0	0.58	0.42
PBE	0	0.58	0.42

Table 3: Net Mulliken charge distribution on the O_2^+ and H_2O fragments in the $O_2^+ \cdot (H_2O)$ complex predicted by CCSD(T), MP2 and a wide range of DFT exchange correlation functionals.

Self-interaction errors can be significantly reduced by long-range corrected hybrid DFT which includes 100% exact Hartree-Fock exchange at long range inter-electronic distances. Consequently, Chai and Head-Gordon developed a series of ωB97 exchange correlation functionals which have been proven to be successful at modelling non-covalent interactions.[52] Therefore in this investigation, the ωB97X-D and ωB97X-D3 exchange correlation functionals were used to investigate its ability at predicting the structure and molecular properties of the $O_2^+ \cdot (H_2O)$ complex.

From comparison of the dipole moments predicted by ωB97X-D and CCSD(T), the ωB97X-D functional incorrectly predicts the direction of the dipole moment. However, the binding energy of 128.3 kJ mol^{-1} for ωB97X-D was found to be much closer to the CCSD(T) value (72.8 kJ mol^{-1}) when compared to the binding energies predicted by B3LYP and B3LYP-D. The ωB97X-D3 exchange correlation functional was also investigated to determine whether the inclusion of empirical dispersion correction in the functional would show improvements to the structure and binding

energy of the $O_2^+ \cdot (H_2O)$ complex. It was found the ωB97X-D3 exchange correlation functional improved the prediction of the binding energy when compared to CCSD(T) results, however the direction of the dipole moment remained unchanged. The charge distribution predicted by ωB97X-D3 and ωB97X-D indicates the positive charge is mainly localised on the oxygen molecule as the water molecule only carries $+0.11e$ of the positive charge. This can be compared to the charge distribution calculated by B3LYP and B3LYP-D where both methods predict the charge on the O_2^+ ion and water molecule to be $+0.59e$ and $+0.41e$, respectively. It is known that DFT suffers from charge delocalisation as a result of self-interaction error, however, the results obtained from the ωB97X-D and ωB97X-D3 exchange correlation functionals, it is apparent that the inclusion of 100% Hartree-Fock exchange in the functional prevents artificial delocalisation of charge from O_2^+ to the water molecule (Table 3) and consequently leads to a more accurate description of the charge distribution in the $O_2^+ \cdot (H_2O)$ complex.

Subsequently, a range of functionals with different fractions of HF exchange were used to investigate the effects of including HF exchange. PBE, PBE0 and PBE50 were used in this study as the functionals possess 0%, 25% and 50% HF exchange, respectively. Such functionals were thus useful in investigating how the binding energy and the direction of the dipole moment varies with the fraction of HF exchange in the functional. From Table 2, a strong correlation between the size of the binding energy error and the percentage of HF exchange in the functional was evident. As the percentage of HF exchange in the functional increased, the direction of the dipole moment shifted closer towards the direction predicted by CCSD(T). Conversely, as the fraction of HF exchange in the functional decreased, an increasing amount of artificial delocalisation of charge from O_2^+ to the water molecule was observed. However even with the PBE50 functional which possesses 50% HF exchange, the binding energy error was relatively high (34.4 kJ mol^{-1}) when compared to CCSD(T) results.

Minnesota exchange correlation functionals were also considered. The functionals M06-L, M06, M06-2X and M06-HF which possess 0%, 27% 54% and 100% HF exchange, respectively were investigated. Similar to the results obtained from the PBE functionals, a strong correlation was also evident between the size of the binding energy error and the percentage of HF exchange in the functional. The magnitude of the binding energy error had increased as the fraction of Hartree-Fock

exchange in the functional decreased and the source of the error can be attributed to an artificial delocalisation of charge from O_2^+ to the water molecule. Also, as the percentage of HF exchange in the functional increased, the direction of the dipole moment shifted closer towards the direction predicted by CCSD(T). Conversely, from Table 3, it was apparent as the fraction of HF exchange is reduced, an increasing amount of delocalisation of the charge from O_2^+ to the water molecule was observed. From comparison of the binding energies predicted using PBE and Minnesota exchange correlation functionals, it was observed the functionals that possess similar fractions of HF exchange predicted similar binding energy values.

Overall, DFT calculations show a large variation in the values for the binding energy from 90 kJ mol^{-1} to 214 kJ mol^{-1}. The magnitude of the error increases as the fraction of Hartree-Fock exchange in the functional decreases and the source of the error can be attributed to the delocalisation of charge from O_2^+ to the water molecule. The artificial delocalisation of charge associated with the use of approximate exchange in DFT studies of related systems is well documented.[57 – 59] The closest agreement with CCSD(T) for the range of DFT exchange correlation functionals investigated was found to be M06-HF, which is a global hybrid functional with 100% HF exchange. For the methods with 100% HF exchange, the positive charge is almost entirely localised on O_2^+ diatomic cation. The values show that the binding energies computed with MP2 are in close agreement with coupled cluster values. Of all the DFT exchange correlation functionals investigated, the Minnesota exchange correlation functional, M06-HF provided the most accurate binding energy value and most accurate prediction for direction of the dipole moment when compared to CCSD(T) results. As a result, the MP2 wavefunction method and M06-HF exchange correlational functional were both used to investigate the structures of the larger $O_2^+ \cdot (H_2O)_n$ cluster ions for $n \geq 2$.

4.2 Structures of $O_2^{+}\cdot(H_2O)_n$ with $n = 1 – 5$

4.2.1 $O_2^{+}\cdot(H_2O)$

As previously mentioned, two distinct minima were identified for the $O_2^{+}\cdot(H_2O)$ complex, both corresponding to planar and non-planar orientations of the water molecule. The two minimum energy structures of $O_2^{+}\cdot(H_2O)$ cluster ions, obtained from the RM search (performed using unrestricted HF with the 6-31+G* basis set) were re-optimised using second order Møller-Plesset (MP2) perturbation theory and the M06-HF exchange correlation functional with the 6-311++G** basis set.

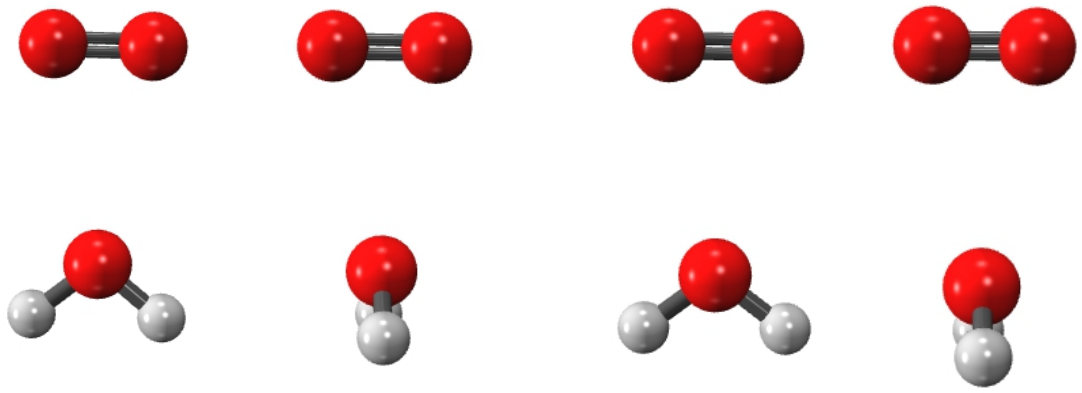


Figure 3: Lowest energy geometries of $O_2^{+}\cdot(H_2O)$ cluster when re-optimised at the MP2/6-311++G** level of theory.

Figure 4: Lowest energy geometries of $O_2^{+}\cdot(H_2O)$ cluster when re-optimised at the M06-HF/6-311++G** level of theory.

The lowest energy structures, re-optimised at the MP2/6-311++G** and M06-HF/6-311++G** level of theory are shown in Figures 3 and 4, respectively. The energies of each cluster with inclusion zero-point energy corrections and the relative energies in comparison to the lowest energy structure are shown in Table 4. For the lowest energy structure found, the hydrogen atoms of the water lie in the same plane as the oxygen diatomic cation, although the corresponding structure with the hydrogen atoms lying approximately perpendicular to the oxygen diatomic cation has a very similar energy. From comparison of the energies between structures 1A and 1B predicted by MP2 and

M06-HF, it is evident the energy difference between the non-planar and planar structure is small. Consequently, an interconversion between the planar and non-planar configuration seems likely to occur at D-region ionospheric temperatures (~220 K).

Method	Structure	Energy (E_h)	ZPE (E_h)	Corrected Energy (E_h)	Relative Energy / kJ mol^{-1}
MP2	1A	-225.913882	0.030186	-225.88370	0.000
	1B	-225.912875	0.029663	-225.88321	1.286
M06-HF	1A	-226.302800	0.032487	-226.27031	0.000
	1B	-226.302275	0.032717	-226.26956	1.969

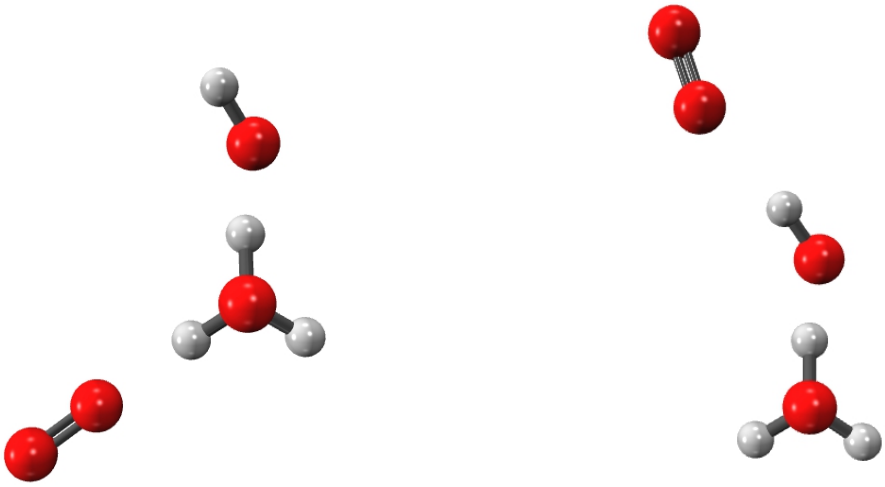
Table 4: Computed energies of the low energy molecular geometries obtained for $O_2^{+\cdot}(H_2O)$, predicted using MP2 and M06-HF.

For both low energy $O_2^{+\cdot}(H_2O)$ structures predicted using both MP2 and M06-HF, the atomic charges and spin confirm the positive charge and spin to be localised on the oxygen molecule. From natural bonding orbital analysis (NBO), the atomic charge and spin value of 1.00 on the oxygen molecule shows the positive charge and an unpaired is localised on the oxygen molecule. This behaviour is also consistent with the ionisation energies. The ionisation energy of neutral O_2 is less than the ionisation energy of a H_2O molecule, hence photoionisation which occurs in the D-region of the ionosphere causes the positive charge to be localised on the oxygen molecule. The lowest energy structure found is also consistent with experimental studies since Susič *et al.* and Angel and Stace recorded the CID MIKE spectrum and observed two significant peaks, one corresponding to O_2^+ and the other corresponding H_2O^+ which provided strong evidence for the cluster to exist in the form of $O_2^{+\cdot}(H_2O)$.[2, 11]

4.2.2 $O_2^{+\cdot}(H_2O)_2$

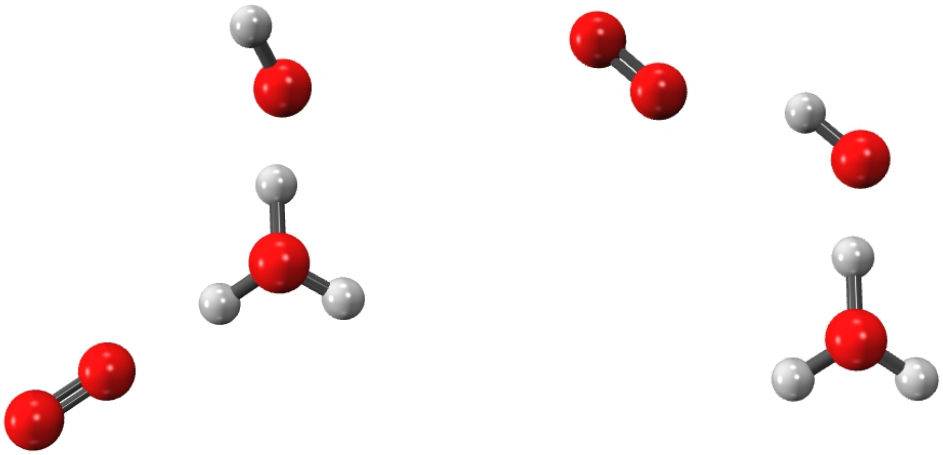
From performing RM searches for $O_2^{+\cdot}(H_2O)_2$ complex in the doublet spin state, unrestricted HF calculations showed the doublet spin state structures to have high

degree of spin contamination and it was difficult to converge the self-consistent field calculation. Consequently, RM searches were performed for $O_2^+ \cdot (H_2O)_2$ complex in the quartet spin state in which two low energy structures were obtained. The minimum energy geometries of $O_2^+ \cdot (H_2O)_2$ cluster ions, obtained from the RM search were re-optimised using MP2 and the M06-HF exchange correlation functional with the 6-311++G** basis set.



MP2-2A MP2-2B

Figure 5: Lowest energy geometries of $O_2^+ \cdot (H_2O)_2$ cluster when re-optimised at the MP2/6-311++G** level of theory.



M06-HF-2A M06-HF-2B

Figure 6: Lowest energy geometries of $O_2^+ \cdot (H_2O)_2$ cluster when re-optimised at the M06-HF/6-311++G** level of theory.

The lowest energy structures, re-optimised at the MP2/6-311++G** and M06-HF/6-311++G** level of theory are shown in Figures 5 and 6, respectively. The energies of each cluster with inclusion zero-point energy corrections and the relative energies in comparison to the lowest energy structure are shown in Table 5.

Method	Structure	Energy (E_h)	ZPE (E_h)	Corrected Energy (E_h)	Relative Energy / kJ mol^{-1}
MP2	2A	-302.201597	0.059623	-302.14197	0.000
	2B	-302.199702	0.058891	-302.14081	3.046
M06-HF	2A	-302.779529	0.059097	-302.72043	0.000
	2B	-302.778785	0.059661	-302.71912	3.439

Table 5: Energies of the low energy molecular geometries obtained for $O_2^+ \cdot (H_2O)_2$, predicted by MP2 and M06-HF.

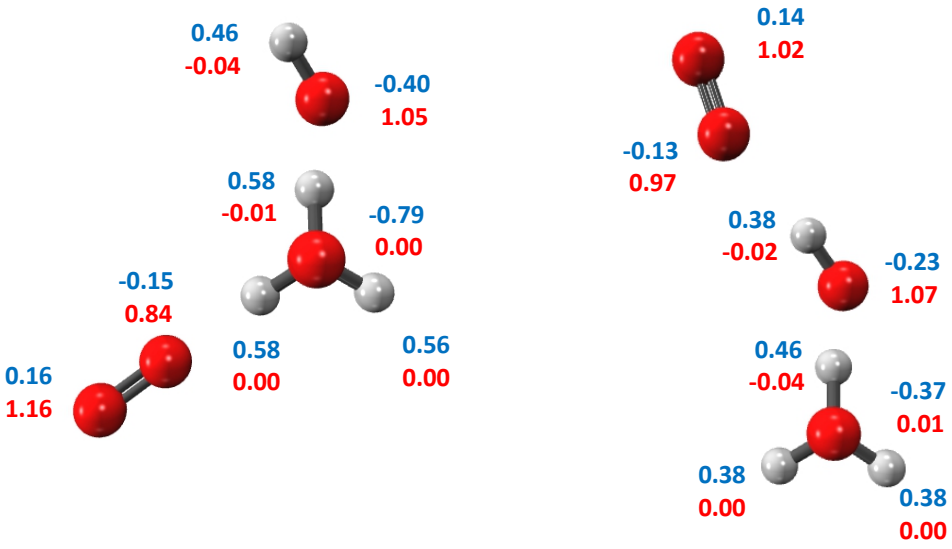
From MP2 calculations, two distinct minima can be identified for the $O_2^+ \cdot (H_2O)_2$ complex, both in which a reorganisation of the two water molecules to form H_3O^+ and OH radical was observed. This suggests the low energy structures for $O_2^+ \cdot (H_2O)_2$ cluster ions undergo charge transfer from the oxygen diatomic cation to the waters, resulting in the formation of a protonated water cluster which has been experimentally observed within the D-region of the ionosphere.[4] Consequently, when using MP2 and M06-HF, the reaction proposed by Angel and Stace will occur where protonated water clusters can be formed from the $O_2^+ \cdot (H_2O)_2$ cluster ion.[2] The lowest energy structure found is also consistent with experimental studies since Angel and Stace recorded the CID MIKE spectrum and observed significant peaks corresponding to H_3O^+ which provided strong evidence for the cluster to exist in the form of $O_2 \cdot H_3O^+ \cdot OH$.[2] The energy difference between structures 2A and 2B was found to be 3.05 kJ mol^{-1} which suggested structure 2A corresponded to the lowest energy structure. The inclusion of zero-point energies showed no difference in the energy ordering of the MP2 structures.

When using M06-HF, structure 2A was also found to be the minimum energy geometry. The results are in agreement with MP2 results, where the lowest energy structure for the $O_2^+ \cdot (H_2O)_2$ complex has the oxygen molecule directly hydrogen

bonded to the H_3O^+ cation. Structure 2A builds from the lowest energy $O_2^+\cdot(H_2O)$ quartet spin state structure (Figure 1C) with an additional proton hydrogen bonding with the water molecule forming H_3O^+ and an OH radical interacting with resulting hydronium cation. Several experimental studies have also considered the structure of ionised water dimers and it was found the lowest energy structure for the $O_2^+\cdot(H_2O)_2$ cluster ion showed to have the form of neutral O_2 interacting with the lowest energy structure for $(H_2O)_2^+$.[26, 27]

From the re-optimised low energy structures using MP2 and M06-HF, the second lowest energy structure found (2B) is very similar to the lowest energy structure (2A), with the only difference being the position of the oxygen molecule relative to the H_3O^+ cation and OH radical. The lowest energy structure for the $O_2^+\cdot(H_2O)_2$ complex has the oxygen molecule hydrogen bonded to the H_3O^+ cation, whereas the second lowest energy structure has the oxygen molecule hydrogen bonded to the OH radical. Both low energy quartet spin state structures have a value of $\langle S^2 \rangle = 3.79$ which indicates the structures are not significantly spin contaminated. The second lowest energy structure also showed to have the form of neutral O_2 interacting with the lowest energy structure for $(H_2O)_2^+$.[26, 27]

For both the low energy $O_2^+\cdot(H_2O)_2$ structures predicted using both MP2 and M06-HF, the charge has transferred from the oxygen diatomic cation to the waters, and a subsequent reorganisation of the water molecules to form H_3O^+ and OH radical was observed. The atomic charge and spin values for $O_2^+\cdot(H_2O)_2$ (Figure 7) are consistent with this, showing the positive charge to be localised on H_3O^+, two unpaired electrons on O_2 and a single unpaired electron on the OH. This behaviour is consistent with the ionisation energies. The ionisation energy of neutral O_2 is less that the ionisation energy of a H_2O molecule but greater than the ionisation energy of $(H_2O)_2$. As a consequence, solar radiation present in the D-region of the ionosphere causes the $(H_2O)_2$ fragment to become ionised resulting in the positive charge to be localised on the water dimer. The results are also consistent with the observation from the experiments performed by Angel and Stace where they showed a charge transfer initially occurs from O_2 to the water dimer, causing the cluster to adopt the structure $O_2{\cdot}H_3O^+OH$ based on collision induced dissociation studies.[2]

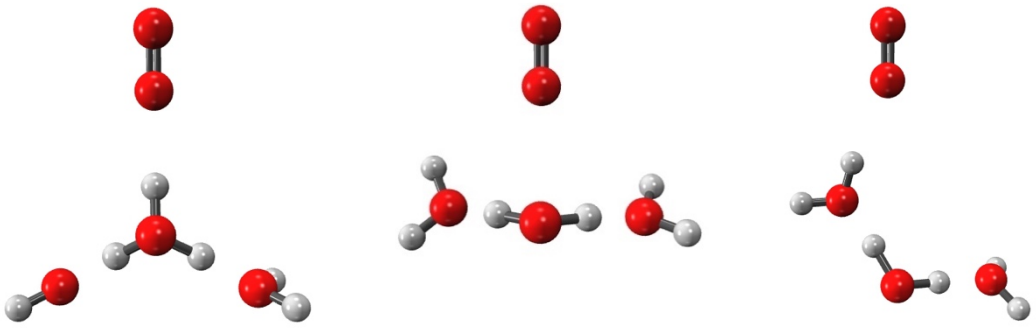


MP2-2A MP2-2B

Figure 7: Atomic charges (upper value in blue) and spin densities (lower value in red) for $O_2^{+}\cdot(H_2O)_2$

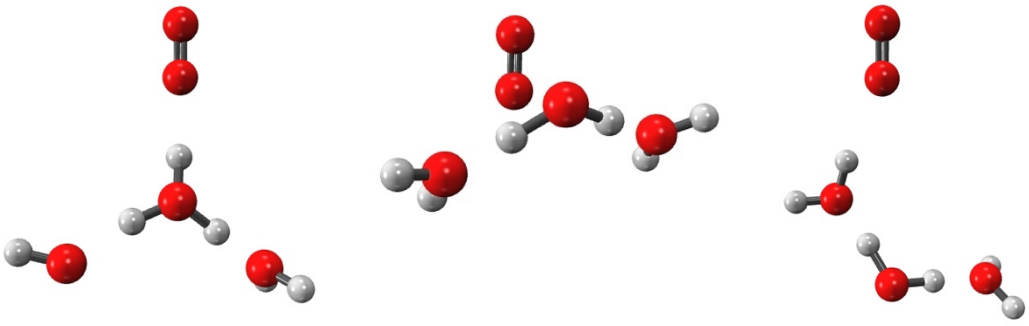
4.2.2 $O_2^{+}\cdot(H_2O)_3$

For the $O_2^{+}\cdot(H_2O)_3$ complex, RM searches were performed in the quartet spin state in which three low energy isomers were obtained. The minimum energy geometries of $O_2^{+}\cdot(H_2O)_3$ cluster ions, obtained from the RM search were re-optimised using MP2 and the M06-HF exchange correlation functional with the 6-311++G** basis set.



MP2-3A MP2-3B MP2-3C

Figure 8: Lowest energy geometries of $O_2^+ \cdot (H_2O)_3$ cluster when re-optimised at the MP2/6-311++G** level of theory.



M06-HF-3A M06-HF-3B M06-HF-3C

Figure 9: Lowest energy geometries of $O_2^+ \cdot (H_2O)_3$ cluster when re-optimised at the M06-HF/6-311++G** level of theory.

The lowest energy structures of the $O_2^+ \cdot (H_2O)_3$ cluster ions, obtained from the RM search procedure using unrestricted HF with the 6-31+G* basis set were re-optimised with MP2 and the M06-HF functional. The energies of each cluster with inclusion zero-point energy corrections and the relative energies in comparison to the lowest energy structure are shown in Table 6.

Method	Structure	Energy (E_h)	ZPE (E_h)	Corrected Energy (E_h)	Relative Energy / kJ mol^{-1}
MP2	3A	-378.520306	0.087490	-378.432816	0.000
	3B	-378.512491	0.086700	-378.425791	18.444
	3C	-378.512343	0.086451	-378.425892	18.180
M06-HF	3A	-379.251623	0.088051	-379.163572	0.000
	3B	-379.247048	0.087828	-379.159220	11.426
	3C	-379.247071	0.088085	-379.158986	12.041

Table 6: Energies of the low energy molecular geometries obtained for $O_2^+ \cdot (H_2O)_3$, predicted by MP2 and M06-HF.

The three lowest energy geometries of $O_2^+ \cdot (H_2O)_3$ were found to be structures 3A, 3B and 3C. Analogous to the low energy structures of $O_2^+ \cdot (H_2O)_2$, a reorganisation of the water molecules to form H_3O^+ and OH radical was observed for the lowest energy $O_2^+ \cdot (H_2O)_3$ complex (structure 3A). As observed with the lowest energy $O_2^+ \cdot (H_2O)_2$ cluster ion, the lowest energy structure for $O_2^+ \cdot (H_2O)_3$ undergoes charge transfer from O_2^+ to the subsequent waters to form a protonated water cluster which has been experimentally detected within the D-region of the ionosphere.[4] Consequently, when using MP2 and M06-HF, the reaction proposed by Angel and Stace occurs in which a protonated water cluster can be formed from the $O_2^+ \cdot (H_2O)_3$ cluster ion.[2] All three low energy quartet spin state structures have a value of $\langle S^2 \rangle = 3.80$ for a quartet state which indicated the structures are not significantly spin contaminated.

Structure 3A builds from the global minimum structure of $O_2^+ \cdot (H_2O)_2$ with the third water molecule forming a hydrogen bond with the H_3O^+ cation. Based on experimental studies performed on the structure of ionised water clusters $(H_2O)_n^+$, the lowest energy structure found for the $O_2^+ \cdot (H_2O)_3$ cluster ion showed to have the form of neutral O_2 hydrogen bonded with the lowest energy structure for $(H_2O)_3^+$.[26, 27] Conversely, for structure 3B, the formation of H_3O^+ and OH radical was not observed, however the two additional water molecules forms hydrogen bonds with both hydrogen atoms of the third water molecule which results in a chain of hydrogen bonded water molecules. Structure 3C is also based on the global minimum structure of $O_2^+ \cdot (H_2O)_2$,

however the third water molecule creates a third solvation shell rather than adding to the second solvation shell as seen in the 3A structure. The third water molecule creates a third solvation shell through hydrogen bonding to the second solvation shell water which results in the formation of a chain of hydrogen bonded water molecules, as seen in structure 3B.

When using MP2, structure 3A was found to be the lowest energy structure, followed by structures 3B and 3C before zero point energy corrections were applied. However once ZPE corrections were included, the energy ordering of the clusters altered with structure 3B becoming the highest energy structure. In contrast, when using M06-HF, structure 3A was also found to be the lowest energy structure which was in agreement with MP2 results. However before ZPE corrections were applied, structure 3B was the highest energy structure. Once ZPE corrections were included, structure 3C became the highest energy structure and the changes in the energy ordering were a result of applying the harmonic approximation when conducting harmonic vibrational frequency calculations which are not as accurate as anharmonic vibrational frequencies.

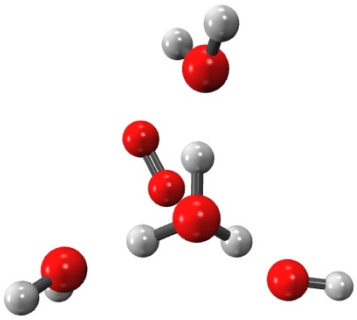
For all three low energy $O_2^{+\cdot}(H_2O)_3$ isomers predicted using both MP2 and M06-HF, the positive charge has transferred from the oxygen diatomic cation to the waters, however a reorganisation of the water molecules to form H_3O^+ and OH radical was only observed for the lowest energy structure (3A). This behaviour is consistent with the ionisation energies. The ionisation energy of neutral O_2 is greater than the ionisation energy of $(H_2O)_3$ and as a consequence, solar radiation present in the D-region of the ionosphere causes the $(H_2O)_3$ fragment to become ionised, resulting in the positive charge to be localised on the water molecules. For the lowest energy $O_2^{+\cdot}(H_2O)_3$ cluster ion, the positive charge is almost entirely localised on the H_3O^+, two unpaired electrons are localised on the oxygen molecule and a single unpaired electron on OH which is also observed in the low energy $O_2^{+\cdot}(H_2O)_2$ cluster ions. The results for the lowest energy $O_2^{+\cdot}(H_2O)_3$ structure is also consistent with the observation from the experiments performed by Angel and Stace where they showed a charge transfer initially occurs from O_2 to the water trimer, causing the cluster to adopt the structure $O_2{\cdot}(H_2O){\cdot}H_3O^{+\cdot}OH$ based on collision induced dissociation studies.[2] Conversely for structures 3B and 3C, closer inspection of the atomic charges and spin shows two unpaired electrons are also localised on the oxygen molecule (as observed with structure 3A), however the positive charge and an unpaired electron was found to be

localised on the water molecule that is hydrogen bonded to the two additional water molecules.

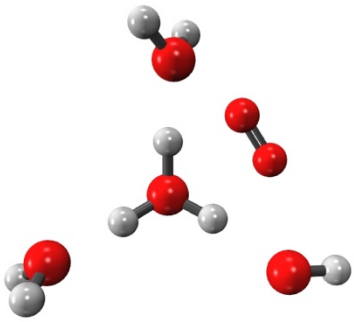
Harmonic vibrational frequency calculations carried out on the coordinates for structure 3C using M06-HF revealed one imaginary vibrational frequency. As a result, at the M06-HF/6-311++G** level of theory, structure 3C corresponds to a transition state structure despite having been identified as a minimum energy structure predicted by MP2. Such structures could provide a pathway for the stepwise solvation of the $O_2^+ \cdot (H_2O)_2$ cluster, as proposed in equation 4, resulting in the global minimum of the $O_2^+ \cdot (H_2O)_3$ cluster being obtained.

4.2.3 $O_2^+ \cdot (H_2O)_4$

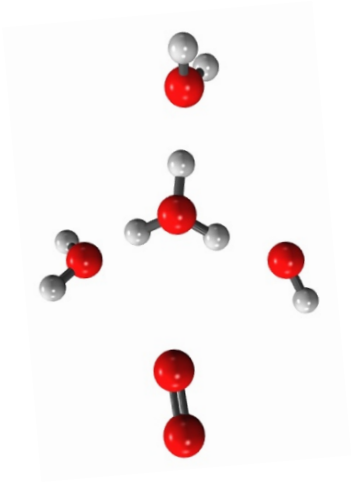
The six low energy structures of $O_2^+ \cdot (H_2O)_4$ obtained from the RM search have a quartet spin state. The minimum energy geometries of $O_2^+ \cdot (H_2O)_4$ cluster ions, obtained from the RM search and re-optimised using MP2 theory and the M06-HF exchange correlation functional with the 6-311++G** basis set are shown in Figure 10. The energies of each cluster with inclusion zero-point energy corrections and the relative energies in comparison to the lowest energy structure are shown in Table 7.



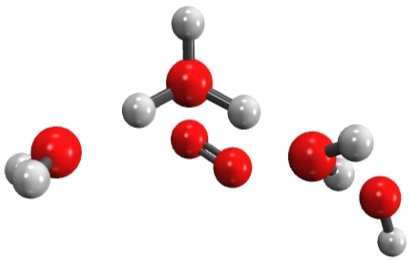
MP2-4A



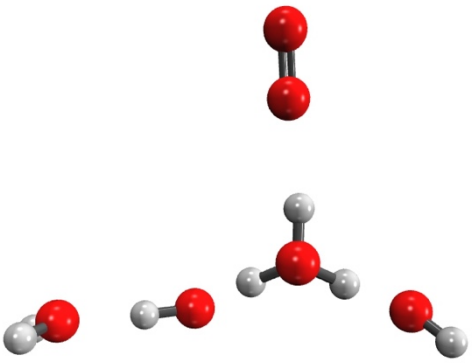
MP2-4B



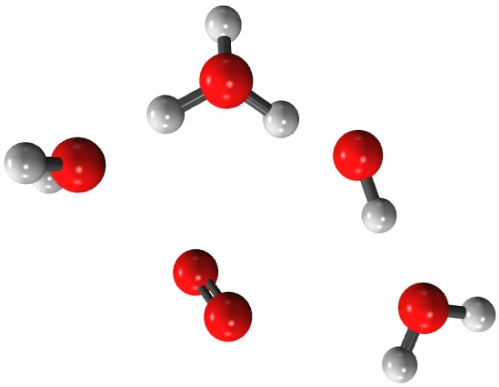
MP2-4C



MP2-4D



MP2-4E



MP2-4F

Figure 10: Lowest energy geometries of $O_2^{+}\cdot(H_2O)_4$ cluster when re-optimised at the MP2/6-311++G** level of theory.

The six lowest energy geometries of $O_2^{+}\cdot(H_2O)_4$ were found to be structures 4A, 4B, 4C, 4D, 4E and 4F, as shown in figure 10. Similar to the observations made from the lowest energy structure for $O_2^{+}\cdot(H_2O)_2$ and $O_2^{+}\cdot(H_2O)_3$ cluster ions, a reorganisation of the water molecules to form H_3O^{+} and OH radical was observed for all six low energy geometries of $O_2^{+}\cdot(H_2O)_4$. All six low energy quartet spin state structures have a value of $\langle S^2 \rangle$ = 3.80 which indicated the structures are not significantly spin contaminated.

Similarly with the lowest energy $O_2^+\cdot(H_2O)_2$ and $O_2^+\cdot(H_2O)_3$ cluster ions, the low energy $O_2^+\cdot(H_2O)_4$ cluster ions undergo charge transfer from O_2^+ to the subsequent water molecules to form a protonated water cluster which have been experimentally detected within the D-region of the ionosphere.[4] Consequently, when using MP2 and M06-HF, the reaction proposed by Angel and Stace occurs in which a protonated water cluster can be formed from the $O_2^+\cdot(H_2O)_4$ cluster ion.[2] Based on experimental studies performed on the structure of ionised water clusters $(H_2O)_n^+$ for n = 4, structures 4A, 4B and 4C showed to have the form of neutral O_2 interacting with the lowest energy structure for $(H_2O)_4^+$ ionised water cluster.[26, 27]

When using MP2 before zero-point energy corrections were applied, structure 4A which shows the formation of a protonated water cluster was found to be the lowest energy structure. Structure 4A builds from the global minimum structure of $O_2^+\cdot(H_2O)_3$ with the fourth water molecule forming a hydrogen bond with the H_3O^+ cation. Structure 4A shows a strong similarity to structure 3A with the only difference being the fourth water molecule hydrogen bonding to H_3O^+ cation rather than the oxygen molecule as seen in structure 3A. For structure 4A, a charge transfer from O_2^+ to the subsequent water molecules occurred which resulted in the formation of the global minimum $(H_2O)_4^+$ ionised water cluster.[26, 27] The second (4B) and third (4C) lowest energy structure found shows strong resemblance to structure 4A (again building from the global minimum structure of $O_2^+\cdot(H_2O)_3$) with the only difference being the position of the oxygen molecule relative to the ionised water cluster. Similar to the observations made from structure 4A, charge transfer from O_2^+ to the subsequent water molecules also occurs which results in the formation of the global minimum $(H_2O)_4^+$ ionised water cluster. [26, 27] The fourth lowest energy structure 4D is different with two water molecules hydrogen bonded with the H_3O^+ cation and an OH radical hydrogen bonded to the subsequent water molecule. Structure 4E also builds from the global minimum structure of $O_2^+\cdot(H_2O)_3$ with the fourth water molecule forming a hydrogen bond with the water molecule in the second solvation shell. Finally structure 4F is similar to structure 4D with the difference being the OH radical hydrogen bonded to the H_3O^+ cation and the subsequent water molecule hydrogen bonded to the OH radical.

Using the M06-HF exchange correlation functional to re-optimise the low energy isomers gives the same six structures to be minimum energy geometries of $O_2^+\cdot(H_2O)_4$. These structures are visually the same as the structures obtained with MP2,

shown in Figure 10 and the relative energies obtained when using M06-HF are shown in Table 7. The relative energies of the clusters when using M06-HF are significantly different to the ordering obtained when using MP2. When using MP2, structure 4A was found to be the lowest energy structure, before ZPE corrections were applied. However once ZPE corrections were included, the energy ordering of the clusters altered with structure 4B becoming the lowest energy structure. Structure 4F was found to be the highest energy structure irrespective of the inclusion of ZPE corrections. When using M06-HF, structure 4B was found to be the highest energy structure which is inconsistent with MP2 results which suggested structure 4B was the lowest energy structure. Once ZPE correction were applied, structure 4C was found to be the lowest energy structure which also contradicted MP2 results.

Method	Structure	Energy (E_h)	ZPE (E_h)	Corrected Energy (E_h)	Relative Energy / kJ mol^{-1}
MP2	4A	-454.829868	0.11638	-454.713488	3.366
	4B	-454.829340	0.11457	-454.714770	0.000
	4C	-454.829180	0.11566	-454.713520	3.282
	4D	-454.824616	0.11454	-454.710076	12.324
	4E	-454.822689	0.11508	-454.707609	18.801
	4F	-454.820681	0.11439	-454.706291	22.262
M06-HF	4A	-455.711536	0.11723	-455.594306	4.474
	4B	-455.703399	0.11751	-455.585889	26.573
	4C	-455.713100	0.11709	-455.596010	0.000
	4D	-455.712355	0.11779	-455.594565	3.794
	4E	-455.708519	0.11720	-455.591319	12.316
	4F	-455.708393	0.11762	-455.590773	13.750

Table 7: Energies of the low energy molecular geometries obtained for $O_2^{+\cdot}(H_2O)_4$, predicted using MP2 and M06-HF.

Harmonic vibrational frequency calculations performed on the low energy structures using M06-HF revealed one imaginary frequency present for structures 4B,

4D and 4F. As a result, at the M06-HF/6-311++G** level of theory, all three structures correspond to a transition state structure despite having been identified as a minimum energy structure predicted using MP2. Consequently, such structures could provide a pathway for the stepwise solvation of the $O_2^{+\cdot}(H_2O)_3$ cluster, as proposed in equation 15, resulting in the global minimum of the $O_2^{+\cdot}(H_2O)_4$ cluster ion being obtained.

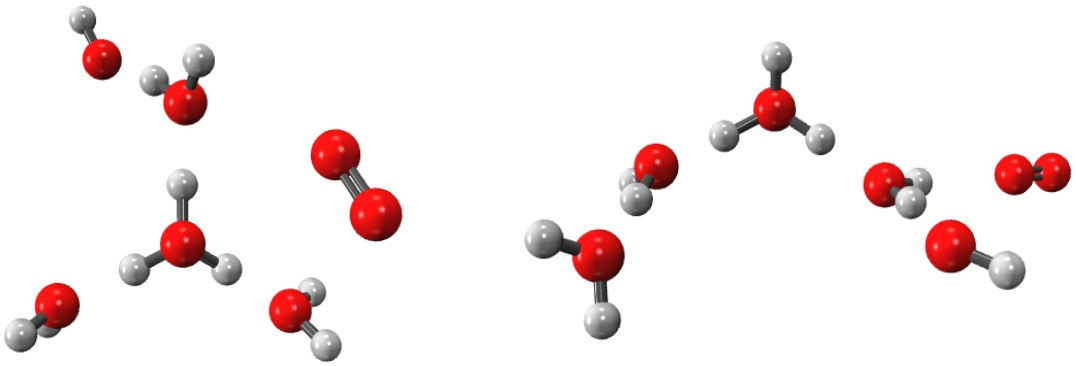
For all six low energy isomers of $O_2^{+\cdot}(H_2O)_4$ predicted using both MP2 and M06-HF, the positive charge has transferred from the oxygen diatomic cation to the waters. This behaviour is consistent with the ionisation energies. The ionisation energy of neutral O_2 is greater than the ionisation energy of $(H_2O)_4$ and as a consequence, solar radiation present within the D-region of the ionosphere causes the $(H_2O)_4$ fragment to become ionised, resulting in the positive charge to be localised on the water molecules. For all six low energy $O_2^{+\cdot}(H_2O)_4$ cluster ions, the positive charge is almost entirely localised on the H_3O^+, two unpaired electrons are localised on the oxygen molecule and a single unpaired electron on the OH radical which is also observed for the low energy $O_2^{+\cdot}(H_2O)_2$ and $O_2^{+\cdot}(H_2O)_3$ cluster ions. The results for the lowest energy $O_2^{+\cdot}(H_2O)_4$ structure is also consistent with the observation from the experiments performed by Angel and Stace where they showed a charge transfer initially occurs from O_2 to the waters, causing the cluster to adopt the structure $O_2{\cdot}(H_2O)_2{\cdot}H_3O^{+}{\cdot}OH$ based on collision induced dissociation studies.[2]

4.2.3 $O_2^{+\cdot}(H_2O)_5$

The two low energy structures of $O_2^{+\cdot}(H_2O)_5$ cluster ions obtained from the RM search procedure were performed in the quartet spin state. The minimum energy geometries of $O_2^{+\cdot}(H_2O)_5$ cluster ions predicted using MP2 and the M06-HF exchange correlation functional with the 6-311++G** basis set are shown in Figure 11. The energies of each cluster ion with inclusion of ZPE corrections and the relative energies in comparison to the lowest energy structure are shown in Table 8.

The two lowest energy geometries of $O_2^{+\cdot}(H_2O)_5$ were found to be structures 5A and 5B. Analogous to the lowest energy structures of $O_2^{+\cdot}(H_2O)_n$ where $n = 2 – 4$, a reorganisation of the water molecules to form H_3O^+ and OH radical was also observed for both low energy geometries for $O_2^{+\cdot}(H_2O)_5$. Similarly with the lowest energy

$O_2^+ \cdot (H_2O)_n$ cluster ions where n = 2 – 4, the low energy $O_2^+ \cdot (H_2O)_5$ cluster ions also undergo charge transfer from O_2^+ to the subsequent water molecules to form a protonated water cluster which have been experimentally detected within the D-region of the ionosphere.[4] Consequently, when using MP2 and M06-HF, the reaction proposed by Angel and Stace occurs in which a protonated water cluster can be formed from the $O_2^+ \cdot (H_2O)_5$ cluster ion, as seen in reaction 17.[2]



MP2-5A MP2-5B

Figure 11: Lowest energy geometries of $O_2^+ \cdot (H_2O)_5$ cluster when re-optimised at the MP2/6-311++G** level of theory.

Structure 5A builds from the global minimum structure of $O_2^+ \cdot (H_2O)_4$ with an additional water molecule hydrogen bonding to the H_3O^+ cation and an OH radical forming a hydrogen bond with the subsequent water molecule. The global minimum structure found for the n = 5 structure has the separated ion-radical pair structure where the OH radical is not directly interacting with H_3O^+ cation which has been shown to be the most stable structure for $(H_2O)_5^+$.[26, 27] For structure 5B, the formation of H_3O^+ and OH was also observed, however the arrangement of the protonated water cluster is different. Structure 5B builds from structure 4D with the OH radical and oxygen molecule forming hydrogen bonds through each of the hydrogen atoms in the first solvation shell water molecule of structure 4D. An additional water molecule hydrogen bonding to the first solvation shell water (located adjacent to the water molecule

hydrogen bonded to oxygen and OH radical) is also observed forming a second solvation shell.

The energy difference between structures 5A and 5B was found to be 12.9 kJ mol^{-1} which suggested structure 5A corresponded to the lowest energy structure. The inclusion of zero-point energies showed no difference in the energy ordering of the MP2 structures. When using M06-HF, structure 5A was also found to be the minimum energy geometry which is in agreement with MP2 results.

Method	Structure	Energy (E_h)	ZPE (E_h)	Corrected Energy (E_h)	Relative Energy / kJ mol^{-1}
MP2	5A	-531.131553	0.14274	-530.988813	0.000
	5B	-531.124788	0.14088	-530.983908	12.878
M06-HF	5A	-532.166193	0.14722	-532.018973	0.000
	5B	-532.163580	0.14656	-532.017020	5.128

Table 8: Energies of the low energy molecular geometries obtained for $O_2^{+\cdot}(H_2O)_5$, predicted by MP2 and M06-HF.

For both low energy $O_2^{+\cdot}(H_2O)_5$ structures predicted using both MP2 and M06-HF, the positive charge has transferred from the oxygen diatomic cation to the waters, resulting in the formation of a protonated water cluster which is consistent with experimental studies performed on such clusters.[2, 4] For both low energy $O_2^{+\cdot}(H_2O)_5$ cluster ions, the positive charge is almost entirely localised on the H_3O^+, two unpaired electrons are localised on the oxygen molecule and a single unpaired electron on the OH radical which is consistent with the observations made for the low energy $O_2^{+\cdot}(H_2O)_n$ where n = 2 – 4 cluster ions.

4.3 Spectra of $O_2^{+}\cdot(H_2O)_n$ with $n = 1 – 5$

4.3.1 $O_2^{+}\cdot(H_2O)$

Harmonic vibrational frequencies for the lowest energy structures for $O_2^{+}\cdot(H_2O)_n$ with $n = 1 – 5$ were computed using MP2 and the corresponding IR spectra for each cluster ion is shown in figure 12. The calculated spectra focus on the O-H stretching region since this is the region of the spectrum that is typically measured in the experimental spectra.

The IR spectrum of the $O_2^{+}\cdot(H_2O)$ cation has been previously measured.[12] Absorptions corresponding to the OH asymmetric stretch (3430.7 cm^{-1}), the OH symmetric stretch (3341.7 cm^{-1}) and the O-O stretch (1601.1 cm^{-1}) were observed, with a further mode assigned to a H_2O-O_2 stretch at 731.0 cm^{-1}.[12] Quantum chemical calculations of the structure and harmonic vibrational frequencies were also performed by the author using DFT and CCSD(T) methods in which a surprising level of discrepancy between the computed vibrational frequencies and experimental data was observed.[12] For example, the CCSD(T) frequencies were over 200 cm^{-1} too high after the application of a suitable scaling factor and the H_2O-O_2 stretching frequency is too low. However, the poor agreement with experimental results was attributable to the large spin contamination, $\langle S^2 \rangle = 1.68$ for a doublet state present in the calculations.

The MP2 computed IR spectrum for the global minimum structure of $O_2^{+}\cdot(H_2O)$ found in this study display two strong peaks corresponding to the O-H symmetric and anti-symmetric stretching modes of the water molecule. The calculated frequencies of the asymmetric stretch, symmetric stretch and O-O stretch predicting using MP2 are 3772 cm^{-1}, 3698 cm^{-1} and 1456 cm^{-1}, respectively. The frequency of the antisymmetric mode is shifted to lower frequency by about 30 cm^{-1} and there is an increase in the relative intensity of the symmetric stretching mode when compared with an isolated water molecule.[53] The closest mode to the reported H_2O-O_2 stretch lies at 650 cm^{-1} and corresponds to a rocking of the water molecule relative to O_2. The computational method used predicts the vibrational frequencies of gas-phase water [53] to within 50 cm^{-1}, and the frequencies are consistent with the CCSD(T) frequencies reported in the experimental paper.[12] However, the calculated frequencies for the $O_2^{+}\cdot(H_2O)$ ion complex deduced from this study are considerably higher than the reported

experimental spectrum.[12] One potential reason for the discrepancy could be the effects of anharmonicity. Exploratory anharmonic vibrational frequency calculations based upon transition-optimised shifted Hermite theory[54] at the HF/6-311++G** level of theory show that the anharmonic frequency correction for the O-H stretching modes in the $O_2^+ \cdot (H_2O)$ complex are about 100 cm^{-1} larger than for the water molecule. This suggests that the scaling factor of 0.95 is underestimating the anharmonic effects in the complex. This would bring the calculated frequencies in closer agreement with the experimental values. Although none of the calculated frequencies upon which the assignment of the measured spectrum to the $O_2^+ \cdot (H_2O)$ complex are in very good agreement with the experimental values suggests further experimental work should be undertaken to confirm those values, or otherwise.

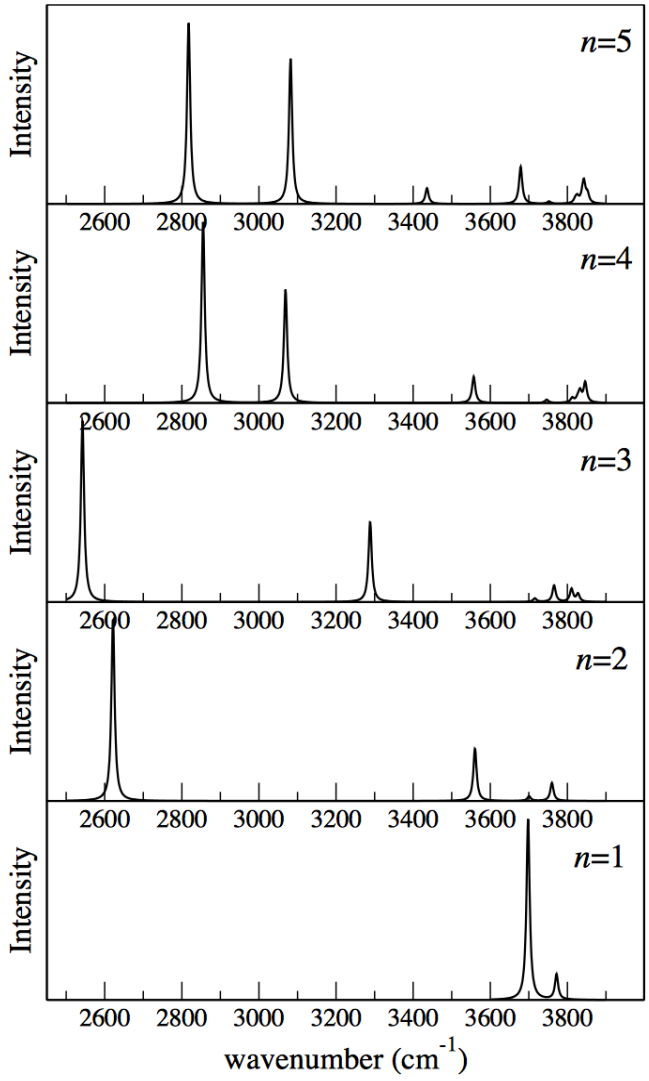


Figure 12: IR spectra for the lowest energy conformers of $O_2^+ \cdot (H_2O)_n$ cluster ions with n = 1 – 5 computed using MP2.

4.3.1 $O_2^{+}\cdot(H_2O)_n$ with $n = 2 – 5$

Harmonic vibrational frequencies for the lowest energy $O_2^{+}\cdot(H_2O)_2$ structure were calculated using MP2 which allowed a theoretical IR spectrum to be produced, as shown in Figure 12. The MP2 computed spectrum display two peaks around 3700 cm^{-1} and 3760 cm^{-1}, corresponding to the OH symmetric and asymmetric stretches. Harmonic vibrational frequency calculations also show a new intense band at 2620 cm^{-1} which is associated with the O-H stretching modes of H_3O^{+} moiety. As the IR spectrum of the $O_2^{+}\cdot(H_2O)_2$ cluster ion has never been measured, a comparison of the MP2 computed IR spectrum with experimental data could not be undertaken. However as previously mentioned, the lowest energy structure for the $O_2^{+}\cdot(H_2O)_2$ cluster ion was shown to have the form of neutral O_2 interacting with the lowest energy structure for $(H_2O)_2^{+}$.[26, 27] The experimental IR spectrum for the ionised water dimer displays two peaks at 3609 cm^{-1} and 3684 cm^{-1} which were assigned to the OH symmetric stretch (out of phase) and OH asymmetric stretches (out of phase), respectively.[25] The computed IR spectrum for the lowest energy $O_2^{+}\cdot(H_2O)_2$ conformer also displayed two peaks between 3600-3800 cm^{-1}, both corresponding to OH symmetric and anti-symmetric stretches, however even after the application of scaling, the computed IR peaks are higher in frequency than the experimental data by around 100 cm^{-1}. As previously mentioned for the $O_2^{+}\cdot(H_2O)$ cluster ion, the discrepancy between the computed and experimental frequencies could due to the effects of anharmonicity. The presence of the oxygen molecule also causes a shift in the vibrational frequencies.

The computed IR spectrum for the lowest energy $O_2^{+}\cdot(H_2O)_3$ conformer also displays two peaks around 3710 cm^{-1} and 3770 cm^{-1}, corresponding to the OH symmetric and asymmetric stretches, respectively. Analogous to the IR spectrum for the lowest energy $O_2^{+}\cdot(H_2O)_2$ conformer, harmonic vibrational frequency calculations show an intense band at 2570 cm^{-1} corresponding to the O-H stretching modes of H_3O^{+} moiety. Similarly to the $O_2^{+}\cdot(H_2O)_2$ cluster ion, a comparison of the MP2 computed IR spectrum with experimental data could not be established as the IR spectrum of the $O_2^{+}\cdot(H_2O)_3$ cluster ion has not been reported. However as previously mentioned, the charge transfer from O_2^{+} to the subsequent water molecules resulted in the formation of the global minimum $(H_2O)_3^{+}$ ionised water cluster.[26, 27] The experimental IR spectrum for the ionised water trimer displays two peaks at 3624 cm^{-1} and 3697 cm^{-1} which were assigned to the OH symmetric stretch and OH anti-symmetric stretch,

respectively.[26] In the MP2 computed IR spectrum, even after the application of scaling, the computed IR peaks are higher in frequency than the experimental data and this discrepancy frequencies could due to the effects of anharmonicity and the presence of the oxygen molecule which could cause a shift in the frequencies.

The computed IR spectrum for the lowest energy $O_2^+ \cdot (H_2O)_4$ conformer displays peaks around between 3700 – 3900 cm^{-1}, corresponding to the OH symmetric and asymmetric stretches. Analogous to the IR spectrum for the lowest energy $O_2^+ \cdot (H_2O)_3$ conformer, harmonic vibrational frequency calculations show an intense band at 2860 cm^{-1} and 3080 cm^{-1} corresponding to the O-H stretching modes of H_3O^+ moiety. There is a significant shift in the frequency of these bands between $n = 3$ and $n = 4$ which is a consequence of O_2 no longer being directly hydrogen bonded to H_3O^+ cation. An additional peak at 3560 cm^{-1} was also observed which corresponds to an OH radical. As mentioned in a previous section, charge transfer from O_2^+ to the subsequent water molecules occurs for the lowest energy $O_2^+ \cdot (H_2O)_4$ conformer which results in the formation of the global minimum $(H_2O)_4^+$ ionised water cluster. [26, 27] It was found the MP2 computed IR spectrum for $O_2^+ \cdot (H_2O)_4$ cluster ion shows a strong agreement with the experimental IR data for the $(H_2O)_4^+$ ionised water cluster.[26] Experimental IR peaks at 3103 cm^{-1}, 3543 cm^{-1}, 3639 cm^{-1} and 3725 cm^{-1} were assigned to a hydrogen bonded OH stretch of water towards an OH radical, OH radical, OH symmetric stretch and OH anti-symmetric stretches, respectively.[26] The computational method used predicts the vibrational frequencies of $(H_2O)_4^+$ ionised water cluster to be within 30 cm^{-1}.[26] The close agreement of the computed IR spectrum for $O_2^+ \cdot (H_2O)_4$ with the experimental IR spectrum of $(H_2O)_4^+$ was a consequence of O_2 no longer being directly hydrogen bonded to H_3O^+ cation. This can be compared with the predicted IR spectra of $O_2^+ \cdot (H_2O)_n$ (n = 2 – 3) cluster ions in which a large discrepancy between the computed frequencies and experimental frequencies of $(H_2O)_n^+$ (n = 2 – 3) was observed as a consequence of O_2 directly hydrogen bonding to the H_3O^+ moiety.

The computed IR spectrum for the lowest energy $O_2^+ \cdot (H_2O)_5$ conformer displays peaks around between 3650 – 3900 cm^{-1}, corresponding to the OH symmetric and asymmetric stretches, as seen in the $O_2^+ \cdot (H_2O)_4$ computed IR spectrum. Harmonic vibrational frequency calculations show an intense band at 2810 cm^{-1} and 3090 cm^{-1} corresponding to the O-H stretching modes of H_3O^+ moiety. As observed with the $O_2^+ \cdot (H_2O)_4$ computed IR spectrum, a significant shift in the frequency of these bands (when compared with the bands observed in the $O_2^+ \cdot (H_2O)_n$ (n = 2 – 3) IR spectra) were

observed as a result of O_2 no longer being directly hydrogen bonded to the H_3O^+ cation. As mentioned in a previous section, the global minimum structure found for the $n = 5$ structure has the separated ion-radical pair structure where the OH radical is not directly interacting with H_3O^+ which has been shown to be the most stable structure for $(H_2O)_5^+$.[26, 27] As observed with the computed $O_2^{+\cdot}(H_2O)_4$ IR spectrum, the computed IR spectrum for $O_2^{+\cdot}(H_2O)_5$ cluster ion shows a strong agreement with the experimental IR data for the $(H_2O)_5^+$ ionised water cluster.[26, 27] Experimental IR peaks at 3458 cm^{-1}, 3647 cm^{-1}, and 3734 cm^{-1} were assigned to a hydrogen bonded OH stretch of water towards an OH radical, OH symmetric stretch and OH anti-symmetric stretches, respectively.[26] The computational method used predicts the vibrational frequencies of $(H_2O)_5^+$ ionised water cluster to be within 30 cm^{-1}.[26] The close agreement of the computed IR spectrum of $O_2^{+\cdot}(H_2O)_5$ with the experimental IR data of $(H_2O)_5^+$ was a consequence of O_2 no longer being directly hydrogen bonded to the H_3O^+ cation. This can be compared to the $O_2^{+\cdot}(H_2O)_n$ (with $n = 2 – 3$) cluster ions MP2 computed IR spectra in which a large discrepancy between the computed and experimental frequencies was observed since O_2 was directly hydrogen bonded to the H_3O^+ moiety.

4.4 Reactivity of $O_2^{+\cdot}(H_2O)_n$ with $n = 2 – 5$

The results from previous sections show that MP2 theory with good quality basis sets provides an accurate description for the structure and energetics of the low energy $O_2^{+\cdot}(H_2O)_n$ cluster ions when compared to CCSD(T) results. There is strong experimental evidence that for $O_2^{+\cdot}(H_2O)_n$ cluster ions with $n \geq 2$, a protonated water cluster (which have been experimentally detected within the lower D-region of the ionosphere via rocket borne mass spectrometric studies) can be formed, as shown in equation 33.[2 – 9] Consequently, the reactivity of $O_2^{+\cdot}(H_2O)_n$ ($n = 2 – 5$) with regards to the formation of a protonated water cluster and OH radical was explored under D-region ionospheric conditions.

$$O_2^{+\cdot}(H_2O)_n^+ \rightarrow H_3O^{+\cdot}(H_2O)_{n-1} + OH + O_2 \qquad (33)$$

AIMD simulations have been performed using the lowest energy structures that were obtained from the random movement search procedure and re-optimised at the MP2/6-311++G** level of theory. Born-Oppenheimer AIMD simulations were performed using MP2 with a moderately sized basis set (6-31+G*) at a temperature of 220 K, which is representative of the temperature in the D-region of the ionosphere, with initial velocities sampled from a Maxwell-Boltzmann distribution. The initial structures consisted of O_2^+ with n undissociated water molecules in a configuration where the position of the oxygen atoms correspond to the lowest energy structures obtained from the random search procedure since for $n \geq 2$ the lowest energy structures have the form of $O_2{\cdot}(H_2O)_{n-2}{\cdot}H_3O^+{\cdot}OH$.

All AIMD simulations for $O_2^+{\cdot}(H_2O)_n$, with $n = 2 – 5$ had started with a structure where O_2 was bound to a cluster of water molecules. The calculations show that for the structures, the positive charge is almost entirely localised on a water molecule. This is consistent with the highest occupied molecular orbital for the neutral clusters corresponding to a lone pair on a water molecule. With the positive charge on a water molecule, as the simulation progresses with thermal initial velocities sampled from a Maxwell-Boltzmann distribution at 220 K, a rearrangement of the water molecules to form H_3O^+ and OH radical was observed, and during this process the O_2 molecule is largely just a spectator. For all of the simulations, the formation of OH radical occurs on a fast timescale and within the simulation length of 4.84 ps (Figure 13).

The analogous simulations for the $n = 1$ cluster was also performed, however no reactions to form OH radical occur which is consistent with experimental studies.[2] For clusters with $n \geq 2$, Angel and Stace performed collision induced dissociation studies on the $O_2^+{\cdot}(H_2O)_n$ cluster ions in which they proposed a charge transfer could initially occur from O_2^+ to the solvent waters, causing the cluster to adopt the structure $O_2{\cdot}(H_2O)_{n-2}{\cdot}H_3O^+OH$.[2] The charge transfer was postulated to result in the formation of a protonated water cluster and cause OH radical, followed by neutral O_2 to leave the cluster as separate entities.[2] The CID MIKE spectrum of $O_2^+{\cdot}(H_2O)_2$ recorded by the authors displayed significant peaks corresponding to H_3O^+ which suggested a charge transfer from O_2^+ to the water dimer must initially occur, facilitating the loss of OH and O_2 to give H_3O^+.[2] Consequently, the reactions observed from the AIMD simulations performed on $O_2^+{\cdot}(H_2O)_n$ ($n = 2 – 5$) show a strong agreement with experimental studies in which the formation of OH radical, H_3O^+ and neutral O_2 occurs in the AIMD

simulations. However, in the experiments, this reaction channel was smaller than the reaction channel where OH is not formed.

In the calculations for $n \geq 2$ the doublet state has not been considered in detail owing to the large spin contamination and erratic convergence associated with the reference HF calculation. Consequently, an accurate description of this state is challenging for single reference methods and multireference methods are likely to be required. The calculations for the doublet state indicate that it is higher in energy than the corresponding quartet state and it corresponds to $O_2^+ \cdot (H_2O)_n$ where OH radical has not been formed. This can be rationalised by considering the spin state of the system. For charge transfer to occur in the doublet state to form O_2 and $(H_2O)_2^+$, the resulting O_2 must be in an excited (singlet) state which will be an energetically less favourable process than the corresponding process for the quartet state where O_2 is in its ground (triplet) state. Consequently, charge transfer and reaction to form OH is less likely to occur in the doublet state.

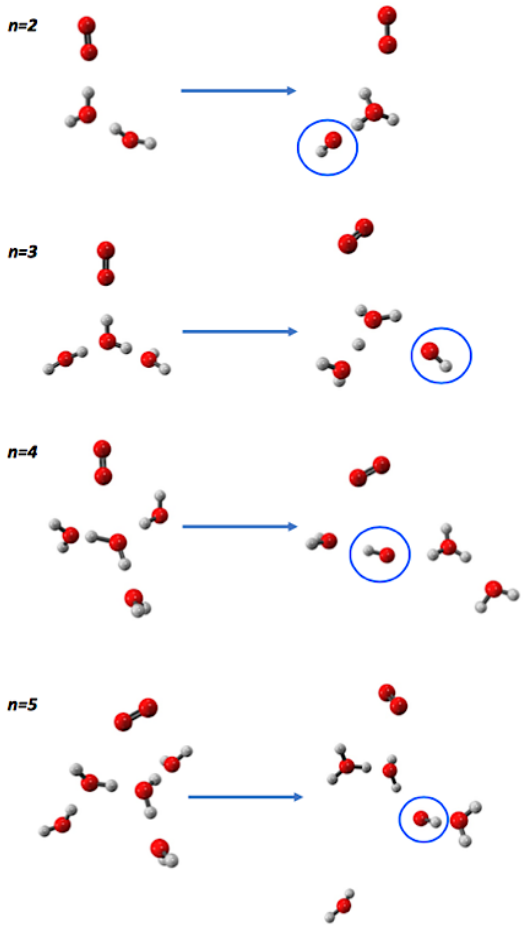


Figure 13: Initial and final structures from AIMD of $O_2^+ \cdot (H_2O)_n$ with the OH radical fragment formed circled.

4.5 Reactivity of $NO^{+}\cdot(H_2O)_n$ with $n = 4 – 5$

Due to the strong experimental evidence for protonated water clusters and nitrous acid formation from cluster ions $NO^{+}\cdot(H_2O)_n$ where n is within the range of 4 – 5, the reactivity of the low energy isomers with respect to protonated water cluster and nitrous acid formation has been investigated in detail in previous studies.[14 – 21] It has been established from MP2 based AIMD simulations performed at typical ionospheric temperatures, the low energy structures for $NO^{+}\cdot(H_2O)_n$ ($n = 4 – 5$) do not conform to structures where a rearrangement to form a protonated water cluster and nitrous acid occurs.[21] However, AIMD simulations using DFT with a small basis set (6-31G) showed an intramolecular reaction to form nitrous acid and a protonated water cluster occurs on a fast timescale.[21]

$$NO^{+}\cdot(H_2O)_4 \rightarrow H_3O^{+}\cdot(H_2O)_3 + HONO \quad (34)$$

$$NO^{+}\cdot(H_2O)_5 \rightarrow H_3O^{+}\cdot(H_2O)_4 + HONO \quad (35)$$

In this study, the reactivity of the lowest energy $NO^{+}\cdot(H_2O)_4$ and $NO^{+}\cdot(H_2O)_5$ clusters ions with respect to the formation of HONO was explored using MP2 based AIMD simulations with initial velocities sampled from the Maxwell-Boltzmann distribution at 220 K. The initial structures were obtained from the most recent theoretical study performed on $NO^{+}\cdot(H_2O)_n$ cluster ions in which the lowest energy geometries were determined for $n = 4 – 5$ through the random movement search procedure.[21] These simulations were performed using MP2 with a small (6-31G), moderately sized (6-31+G*) and large (6-311++G**) basis set for both $n = 4$ and 5 at a significantly longer simulation length of 9.676 ps in comparison to the previous study where only a simulation time of 4 ps was performed. However, no reactions to form nitrous acid and a protonated water cluster were observed during the time-scale studied. In contrast to the AIMD simulations performed on $O_2^{+}\cdot(H_2O)_n$ ($n = 2 – 4$), the ionisation energy of NO is less than water, hence no charge transfer to the water molecules occur. During the AIMD simulations for $NO^{+}\cdot(H_2O)_4$ and $NO^{+}\cdot(H_2O)_5$ complexes, the molecules within the cluster move around their initial positions and there is no large change in the structure of the cluster and no indication that an intramolecular reaction

will occur (figure 14). In making these observations it is important to note some of the limitations of the simulations. The simulations are adiabatic, and as a result are confined to a single potential energy surface and consequently changing electronic state is not possible. Another factor is that the simulations do not account for zero-point energy, which could potentially promote reactivity. Another potential cause for the unobserved reactivity is temperature since at increased temperatures, higher energy isomers of $NO^{+}\cdot(H_2O)_n$ become more populated.[55, 56] However, simulations ran at significantly higher temperatures also did not show reactivity and hence it appears unlikely that zero point vibrational energy (ZPVE) effects will significantly alter the picture deduced herein.

This unexpected behaviour has been previously rationalised by the comparison of the relative energies for the lowest energy $NO^{+}\cdot(H_2O)_5$ cluster ion against the energy of the cluster containing HONO using different levels of theory.[21] For methods that include 100% Hartree-Fock exchange (MP2 and M06-HF) with moderately size or large basis sets, the lowest energy structures with HONO was estimated to be higher in energy than the global minimum energy structures for $n = 4$ and 5 which explained why the formation of nitrous acid was unfavourable. However, quantum chemical methods associated with small basis sets predicts the lowest energy HONO containing cluster to be lower in energy with the DFT calculations predicting a relative energy of about -100 kJ mol^{-1}, hence the inaccurate description of the energetics of the system underlies the observed reactivity in the corresponding AIMD simulations.[21]

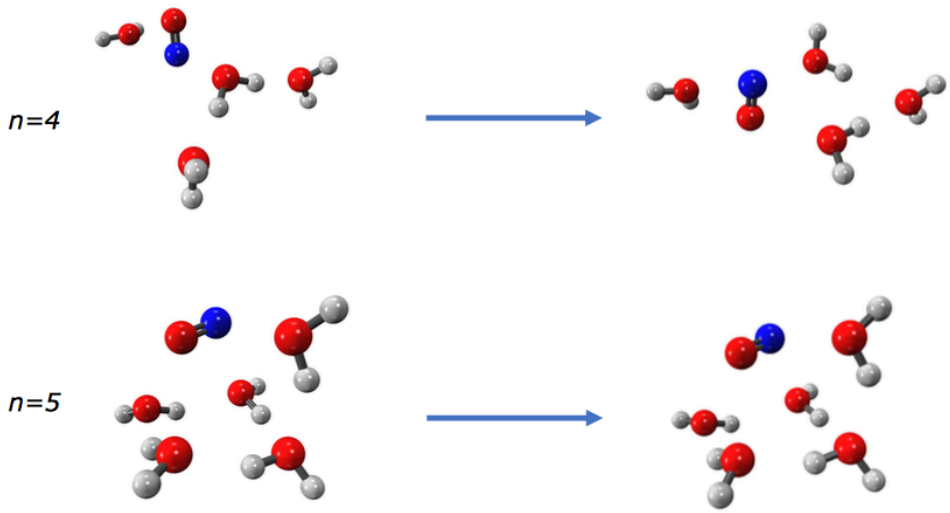


Figure 14: Initial and final structures of the AIMD MP2/6-311++G** simulations of $NO^{+}\cdot(H_2O)_4$ and $NO^{+}\cdot(H_2O)_5$ with thermal initial velocities.

The results from the MP2 based AIMD simulations performed on equilibrated low energy $NO^+\cdot(H_2O)_4$ and $NO^+\cdot(H_2O)_5$ clusters ions in this investigation appear to be inconsistent with the presence of nitrous acid and protonated water clusters experimentally detected within the D-region of the ionosphere.[3 – 5] In order to explain the reactivity of these clusters, the initial conditions of the clusters were considered. In the D-region of the ionosphere, $NO^+\cdot(H_2O)_5$ cluster ions could be formed from the association of a water molecule to $NO^+\cdot(H_2O)_4$ which would lead to $NO^+\cdot(H_2O)_5$ with excess energy. The association of a water molecule to $NO^+\cdot(H_2O)_4$ will impart additional energy to the cluster owing to its kinetic energy and the favourable binding energy. As a consequence, the resulting energy of the cluster will not conform to equilibrium conditions at 220 K and would be heated and highly vibrationally excited which would promote reactivity to form nitrous acid and a protonated water cluster.

$$NO^+\cdot(H_2O)_4 + H_2O \rightarrow H_3O^+\cdot(H_2O)_3 + HONO \qquad (36)$$

The collision of a water molecule with the most stable $NO^+\cdot(H_2O)_4$ cluster ion has been simulated to deduce whether the resulting complex, with excess energy would be more susceptible to the formation of nitrous acid and a protonated water cluster. AIMD simulations were performed where an additional water molecule was started at a location away from the $NO^+\cdot(H_2O)_4$ cluster ion and provided a kinetic energy of approximately 100 kJ mol^{-1} and a velocity directed towards the NO^+ ion. The initial velocities of the atoms in the $NO^+\cdot(H_2O)_4$ cluster ion were sampled from the Maxwell-Boltzmann distribution at a typical D-region ionospheric temperature (220 K.) The AIMD simulations were performed using MP2/6-311++G** as this level of theory has proven to accurately describe the structure and energetics of the low energy isomers of $NO^+\cdot(H_2O)_n$ cluster ions in previous studies.[21] The initial starting locations of the water molecules are illustrated in Figure 15. It is not practicable to sample all possible initial conditions, such as initial position, velocity and orientation of the colliding water molecule since an AIMD simulation is necessary for each choice. Consequently, the aim of the simulations is to illustrate that protonated water clusters are formed under some of the test conditions.

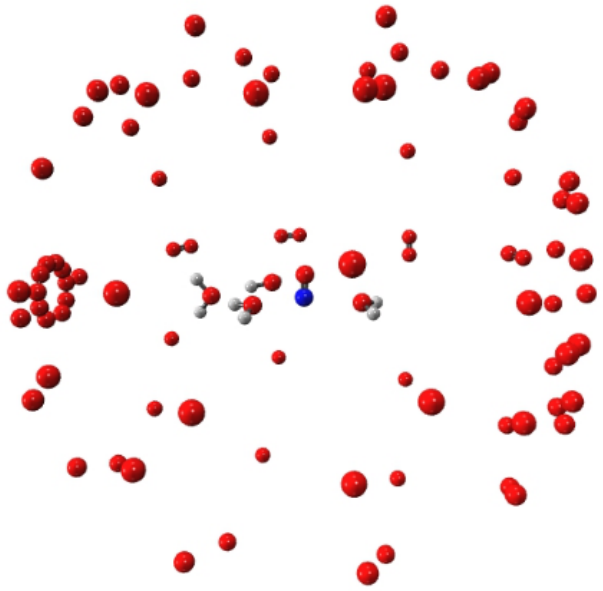


Figure 15: Composite diagram showing the initial positions of the water molecules in the collision-based AIMD simulations, the hydrogen atoms of the colliding water molecules have been omitted for clarity.

A key observation of the simulations is that some collisions with the $NO^+{\cdot}(H_2O)_4$ cluster ion do lead to the formation of protonated water clusters. These collisions lead to various other fragments being formed including dissociated nitrous acid i.e. NO and OH. The initial positions of the water molecules that resulted in the formation of protonated water clusters are also shown in Figure 17. The majority of the successful reactions arise from when the colliding water molecule contacts the oxygen atom of NO^+ first. Collisions with the water molecules surrounding NO^+ do not appear to lead to reactions to form protonated water clusters. The initial orientation of the water molecule does not appear to be an important factor as once the water molecule experiences the NO^+ potential, it re-orientates to collide with the oxygen atom first. The colliding water molecule loses a proton which becomes associated with the surrounding water molecules, forming protonated water clusters and the HONO fragment leaves the cluster as a separate entity. In all of the examples studied where HONO is formed, the fragment is too energetic and dissociates to give OH and NO. An example of the AIMD simulation forming dissociated nitrous acid (NO and OH) is shown in figure 16.

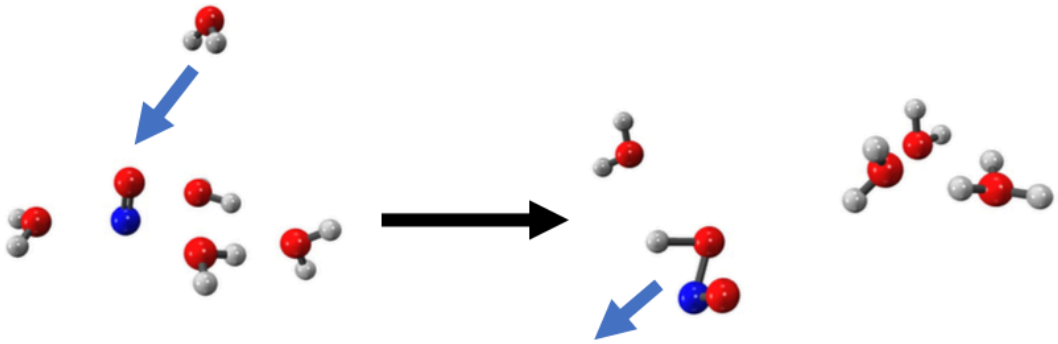


Figure 16: Ab initio molecular dynamics simulation of a water molecule collision onto the most stable $NO^+ \cdot (H_2O)_4$ cluster leading to the formation of protonated water cluster and nitrous acid.

For the reaction shown, reducing the initial velocity of the water molecule by 10% does not lead to the formation of protonated water clusters but to the ejection of NO^+ ion from the cluster. This indicates that both the impact direction and velocity of the colliding water molecule are important factors.

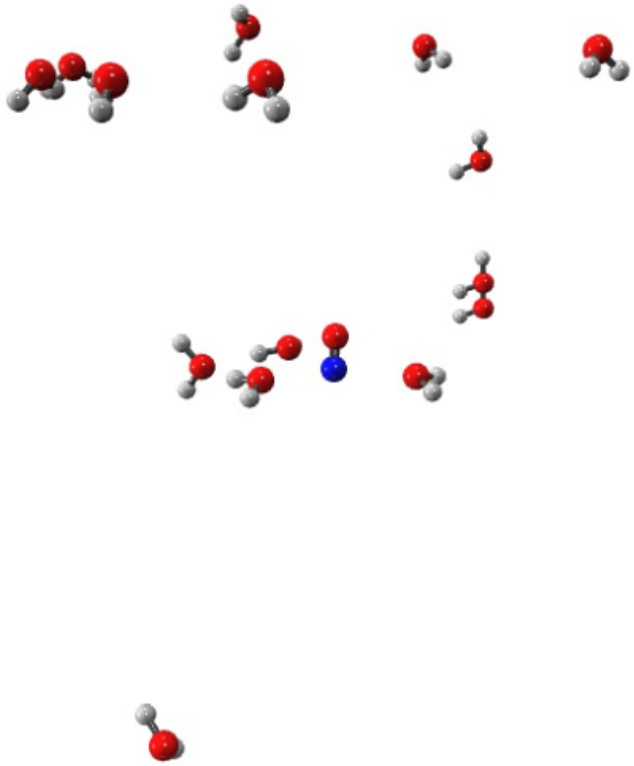


Figure 17: Composite diagram showing the initial locations of the water molecules that led to the formation of protonated water clusters.

4.6 Conclusions

In this study, quantum chemical calculations have been performed to study the formation of protonated water clusters (as experimentally detected within the D-region of the ionosphere [3, 4]) from $O_2^+\cdot(H_2O)_n$ and $NO^+\cdot(H_2O)_n$ cluster ions. The minimum energy geometries of $O_2^+\cdot(H_2O)_n$ with $n = 1 – 5$ were obtained through using the random movement search procedure that was performed using the unrestricted HF with a moderately sized basis set (6-31+G*). A variety of different quantum chemical methods including MP2 and a range of DFT exchange-correlation functionals were investigated and their ability to predict the binding energy, dipole moment and charge distribution for the $O_2^+\cdot(H_2O)$ cluster in comparison to CCSD(T) results were assessed to determine the most suitable method for studying the larger $O_2^+\cdot(H_2O)_n$ cluster ions ($n \geq 2$).

The functionals B3LYP and B3LYP-D were investigated where it was discovered the inclusion of the empirical dispersion correction in the functional resulted in an increase in error for the binding energy when compared B3LYP results. However the direction of the dipole moment had improved as it shifted closer towards the direction of the dipole moment predicted by CCSD(T). The binding energy between O_2^+ and H_2O predicted by both functionals was overestimated by over 100 kJ mol^{-1} and this vast overestimation was explained through the inaccurate prediction for the direction of the dipole moment, when compared to CCSD(T) results and is a consequence of the inaccurate description for the charge distribution in the cluster.

The ωB97X-D and ωB97X-D3 exchange correlation functionals, which are long-ranged corrected hybrid DFT that incorporates 100% exact Hartree-Fock exchange at long range inter-electronic distances were also investigated. [52] It was found both functionals provide a more accurate description for the binding energy, dipole moment direction and charge distribution than both B3LYP and B3LYP-D functionals. The inclusion of dispersion correction in the functional showed an improvement for the binding energy when compared to CCSD(T) results, however direction of the dipole moment remained unchanged. Despite this, both functionals showed large errors in the binding energy, dipole moment direction and charge distribution when compared to CCSD(T) results. It is known DFT suffers from charge delocalisation as a result of self-interaction error,[57 – 59] however from the results obtained from ωB97X-D and ωB97X-D3, it is apparent that the inclusion of 100% Hartree-Fock exchange in the

functional prevents artificial delocalisation of charge from O_2^+ to the water molecule and consequently leads to accurate modelling for charge distribution in the $O_2^+\cdot(H_2O)$ complex.

Subsequently, the PBE and Minnesota functionals which possess different fractions of HF exchange were used to investigate the effects of including HF exchange in the functional. It was observed as the percentage of HF exchange in the functional decreased, the magnitude of the binding energy error, when compared to CCSD(T) results increased and the source of error was attributed to the increasing delocalisation of charge from O_2^+ to the water molecule. Conversely, as the percentage of HF exchange in the functional increased, the direction of the dipole moment shifted closer towards the direction predicted by CCSD(T). The closest agreement for the binding energy value predicted by CCSD(T) for the range of DFT exchange correlation functionals investigated was found to be M06-HF, which is a global hybrid functional with 100% HF exchange. For the methods with 100% HF exchange, the positive charge is almost entirely localised on O_2^+ diatomic cation. The values also show that the binding energies computed with MP2 are in close agreement with coupled cluster values. Of all the DFT exchange correlation functionals investigated, the Minnesota exchange correlation functional, M06-HF provided the most accurate binding energy value and most accurate prediction for direction of the dipole moment when compared to CCSD(T) results.

Consequently the low energy $O_2^+\cdot(H_2O)_n$ with n = 1 – 5 cluster ions obtained from the random movement search procedure were re-optimised with the M06-HF functional. Additionally the low energy structures were also re-optimised using MP2 level of theory as this method has proven to provide an accurate description for the binding energies, dipole moment and charge distribution for similar atmospheric cluster ions.[21] For the $O_2^+\cdot(H_2O)$ cluster, the most stable structure corresponds to a doublet state with O_2^+ and H_2O fragments. Two distinct minima can be identified for the $O_2^+\cdot(H_2O)$ complex corresponding to planar and non-planar orientations of the water molecule. For the lowest energy structure found, the hydrogen atoms of the water lie in the same plane as the oxygen ion, although the corresponding structure with the hydrogen atoms lying approximately perpendicular to the oxygen ion has a very similar energy. The lowest energy structure was also found to be consistent with experimental studies since the recorded CID MIKE spectrum of the complex displayed two significant peaks, one corresponding to O_2^+ and the other corresponding H_2O^+ which provided strong

evidence for the cluster to exist in the form of $O_2^+ \cdot (H_2O)$.[2, 11] The binding energy computed with MP2 is in good agreement with experimental measurements while the binding energy computed with DFT is highly dependent on the exchange-correlation functional used.

For the larger $O_2^+ \cdot (H_2O)_n$ with $n = 2 – 5$ clusters, there is a fundamental change in the nature of the lowest energy structures. From performing RM searches for $O_2^+ \cdot (H_2O)_n$ cluster ions where $n = 2 – 5$ in the doublet spin state, unrestricted HF calculations showed the doublet spin state structures to have high degree of spin contamination and it was difficult to converge the self-consistent field calculation. Consequently, RM searches were performed for $O_2^+ \cdot (H_2O)_n$ with $n = 2 – 5$ complexes in the quartet spin state. When using MP2 and M06-HF, the lowest energy structures found corresponded to quartet spin states in which a charge transfer occurred from the oxygen diatomic cation to a water molecule resulting in a reorganisation of the water molecules to form H_3O^+ and OH radical. Each of the lowest energy structures for $O_2^+ \cdot (H_2O)_n$ ($n = 2 – 5$) showed to have the form of neutral O_2 interacting with the lowest energy structure for $(H_2O)_n^+$ where $n = 2 – 5$. [26, 27] The results for the lowest energy $O_2^+ \cdot (H_2O)_n$ ($n = 2 – 5$) structures are also consistent with the observations made from the experiments performed by Angel and Stace where they showed a charge transfer initially occurs from O_2 to the waters, causing the cluster to adopt the structure $O_2 \cdot (H_2O)_{n-2} \cdot H_3O^+ \cdot OH$ based on collision induced dissociation studies.[2]

MP2 based Born-Oppenheimer AIMD simulations have been performed on the lowest energy structures for $O_2^+ \cdot (H_2O)_n$ ($n = 2 – 5$) clusters at typical ionospheric temperature to investigate potential reaction pathways for the formation of a protonated water cluster which have been experimentally detected within the D-region of the ionosphere.[3, 4] The calculations show that for the structures, the positive charge is almost entirely localised on a water molecule. With the positive charge on a water molecule, as the simulation progresses with thermal initial velocities sampled from a Maxwell-Boltzmann distribution at 220 K, a rearrangement of the water molecules to form H_3O^+ and OH radical was observed, and during this process the O_2 molecule is largely just a spectator. For all of the simulations, the formation of OH radical occurs on a fast timescale and within the simulation length of 4.84 ps. Consequently, when using MP2 and M06-HF, the reaction postulated by Angel and Stace occurs in which

protonated water clusters can be formed from the $O_2^+ \cdot (H_2O)_n$ ($n = 2 – 5$) cluster ions, as proposed in equation 17.[2]

For the $NO^+ \cdot (H_2O)_n$ clusters, a different behaviour is observed. The reactions of $NO^+ \cdot (H_2O)_n$ involve an intracluster bimolecular reaction to form a protonated water cluster and nitrous acid. MP2 based Born-Oppenheimer AIMD simulations with initial velocities sampled from the Maxwell-Boltzmann distribution at a typical ionospheric temperature (220 K) show no reaction to occur, which is in contrast to simulations based upon DFT.[21] This inconsistency with atmospheric and experimental observations was resolved by considering a collision of a water molecule with a $NO^+ \cdot (H_2O)_4$ cluster ion. The resulting highly vibrationally excited $NO^+ \cdot (H_2O)_5$ complex was postulated to become more susceptible to formation of nitrous acid and a protonated water cluster. AIMD simulations replicating these conditions in which a water molecule collides with the $NO^+ \cdot (H_2O)_4$ cluster ion show that some collisions with the cluster do indeed lead to the formation of a protonated water cluster. The majority of the successful reactions arise when the colliding water molecule contacts the oxygen atom of NO^+ first. Conversely, collisions with the water molecules surrounding NO^+ do not appear to lead to reactions to form protonated water clusters. For the reaction shown, reducing the initial velocity of the water molecule by 10% does not lead to the formation of protonated water clusters but to the ejection of NO^+ ion from the cluster which indicates that both the impact direction and velocity of the colliding water molecule are important factors.

Future work could involve higher level theoretical investigations into the role played by atmospheric trace species in the formation of $O_2^+ \cdot (H_2O)_n \cdot X$ clusters ions, (where X represents abundant atmospheric molecules) which in turn leads to the formation of protonated water clusters, as experimentally observed within the D-region of the ionosphere. Similar to the procedure undertaken in this investigation, geometry optimisation calculations can be performed on the $O_2^+ \cdot (H_2O)_n \cdot X$ cluster ions to determine the equilibrium geometries and transition state structures. Born-Oppenheimer AIMD simulations could also be carried out on the $O_2^+ \cdot (H_2O)_n \cdot X$ cluster ions to deduce potential reaction pathways for the formation $O_2^+ \cdot (H_2O)_n$ clusters ions. Previous experimental work on $O_2^+ \cdot (H_2O)_n$ clusters ions have shown that in the presence of nitrogen gas, $O_2^+ \cdot (H_2O) \cdot N_2$ cluster ions are formed and subsequent hydration causes a ligand exchange reaction resulting in the formation of larger hydrated dioxygenyl cluster ions. Similarly, it has been shown for $O_2^+ \cdot (H_2O) \cdot N_2$ cluster

ions in the presence of carbon dioxide, $O_2^+ \cdot (H_2O) \cdot CO_2$ cluster ions can be formed, and further hydration can also lead to larger $O_2^+ \cdot (H_2O)_n$ clusters ions. Consequently, future theoretical investigations into the roles played by atmospheric trace species in reaction 33 may contribute to the explanation for the high abundance of protonated water clusters present within the D-region of the ionosphere.

6. References

1. A He R, L. Lib, J. Zhong, C. Zhub, J.S. Francisco, X.C. Zeng, *Proc. Natl. Acad. Sci.*, 2016, **113**, 4629-4633.

2. L. Angel and A.J. Stace, *J. Phys. Chem.* A., 1999, **103**, 2999-3005.

3. A. Nicolet and A.C. Aikin, *J. Geophys. Res.*, 1960, **65**, 1469-1483.

4. R. Narcisi and A.D. Bailey, *J. Geophys. Res*., 1965, **70**, 3687-3700.

5. F.C. Fehsenfeld and E.E. Ferguson, *J. Geophys. Res*., 1969, **74**, 2217-2222.

6. A. Good, D.A. Durden and P. Kebarle, *J. Chem. Phys*., 1970, **52**, 222-229.

7. N.G. Adams, D.K. Bohme, D.B. Dunkin F.C. Fehsenfeld and E.E. Ferguson, *J. Chem. Phys*., 1970, **52**, 3133-3140.

8. A.B. Rakshit and P. Warneck, *J. Chem. Phys*., 1980, **73**, 5074-5080.

9. J.L. McCrumb, *Planet. Space Sci.*, 1982, **30**, 559-573.

10. J.A. Vanderhoff and R.A. Beyer, *Chem. Phys. Lett.*, 1976, **38**, 532-536.

11. R. Susic, B. Kralj and D. Zigon, *Rapid Commun. Mass Spectrom*., 1995, **9**, 64-66.

12. M.F. Zhou, A.H. Zeng, Y. Wang, Q.Y. Kong, Z.X. Wang and P.R. Schleyer, *J. Am. Chem. Soc.*, 2003, **125**, 11512-11513.

13. M. Nicolet, Ph.D. thesis, University of Brussels, 1945.

14. D.B Dunkin, F.C. Fehsenfeld, A.L. Schmeltekopf and E.E. Ferguson, *J. Chem. Phys*., 1971, **54**, 3827-3822.

15. F. C. Fehsenfeld, M. Mosesman, and E. E. Ferguson, *J. Chem. Phys*., 1971*,* **55**, 2120.

16. J.H. Choi, K.T. Kuwata, B.M. Haas, Y. Cao, M.S. Johnson and M. Okumura, *J. Chem. Phys*., 1994, **100**, 7153-7165.

17. L. Angel and A.J. Stace, *J. Chem. Phys*., 1998, **109**, 1713-1715.

18. E. Hammam, E.P.F. Lee and J.M. Dyke, *J. Phys. Chem*., 2000 **104**, 4571-4580.

19. E. Hammam, E.P.F. Lee and J.M. Dyke, *J. Phys. Chem*., 2001 **105**, 5528-5534.

20. A. Asada, M. Nagaoka and S. Koseki, *Phys. Chem. Chem. Phys*., 2011 **13**, 1590-1596.

21. K.A. Linton, T.G. Wright and N.A. Besley, *Phil. Trans. Roy. Soc.* (London) A, 2018, **376**, 2115.

22. K.R. Siefermann and B. Abel, *Science*, 2010 **327**, 280-281.

23. N. Eyet, N.S. Shuman, A.A. Viggiano, J. Troe, R.A. Relph, R.P. Steele and M.A. Johnson, *J. Phys. Chem. A*., 2011 **115**, 7582-7590.

24. Y. Shao, Z. Gan, E. Epifanovsky, A. T. B. Gilbert, M. Wormit, J. Kussmann, A. W. Lange, A. Behn, J. Deng, X. Feng, D. Ghosh, M. Goldey P. R. Horn, L. D. Jacobson, I. Kaliman, R. Z. Khaliullin, T. Kús, A. Landau, J. Liu, E. I. Proynov, Y. M. Rhee, R. M. Richard, M. A. Rohrdanz, R. P. Steele, E. J. Sundstrom, H. L. Woodcock III, P. M. Zimmerman, D. Zuev, B. Albrecht, E. Alguire, B. Austin, G. J. O. Beran, Y. A. Bernard, E. Berquist, K. Brandhorst, K. B. Bravaya, S. T. Brown, D. Casanova, C.-M. Chang, Y. Chen, S. H. Chien, K. D. Closser, D. L. Crittenden, M. Diedenhofen, R. A. DiStasio Jr., H. Dop, A. D. Dutoi, R. G. Edgar, S. Fatehi, L. Fusti-Molnar, A. Ghysels, A. Golubeva-Zadorozhnaya, J. Gomes, M. W. D. Hanson-Heine, P. H. P. Harbach, A. W. Hauser, E. G. Hohenstein, Z. C.

Holden, T.-C. Jagau, H. Ji, B. Kaduk, K. Khistyaev, J. Kim, J. Kim, R. A. King, P. Klunzinger, D. Kosenkov, T. Kowalczyk, C. M. Krauter, K. U. Lao, A. Laurent, K. V. Lawler, S. V. Levchenko, C. Y. Lin, F. Liu, E. Livshits, R. C. Lochan, A. Luenser, P. Manohar, S. F. Manzer, S.-P. Mao, N. Mardirossian, A. V. Marenich, S. A. Maurer, N. J. Mayhall, C. M. Oana, R. Olivares-Amaya, D. P. O'Neill, J. A. Parkhill, T. M. Perrine, R. Peverati, P. A. Pieniazek, A. Prociuk, D. R. Rehn, E. Rosta, N. J. Russ, N. Sergueev, S. M. Sharada, S. Sharmaa, D. W. Small, A. Sodt, T. Stein, D. Stück, Y.-C. Su, A. J. W. Thom, T. Tsuchimochi, L. Vogt, O. Vydrov, T. Wang, M. A. Watson, J. Wenzel, A. White, C. F. Williams, V. Vanovschi, S. Yeganeh, S. R. Yost, Z.-Q. You, I. Y. Zhang, X. Zhang, Y. Zhou, B. R. Brooks, G. K. L. Chan, D. M. Chipman, C. J. Cramer, W. A. Goddard III, M. S. Gordon, W. J. Hehre, A. Klamt, H. F. Schaefer III, M. W. Schmidt, C. D. Sherrill, D. G. Truhlar, A. Warshel, X. Xua, A. Aspuru-Guzik, R. Baer, A. T. Bell, N. A. Besley, J.-D. Chai, A. Dreuw, B. D. Dunietz, T. R. Furlani, S. R. Gwaltney, C.-P. Hsu, Y. Jung, J. Kong, D. S. Lambrecht, W. Liang, C. Ochsenfeld, V. A. Rassolov, L. V. Slipchenko, J. E. Subotnik, T. Van Voorhis, J. M. Herbert, A. I. Krylov, P. M. W. Gill, and M. Head-Gordon, *Mol. Phys*., 2015, **113**, 184-215.

25. L. I. Yeh, M. Okumura, J. D. Myers, J. M. Price, Y. T. Lee, *J. Chem. Phys.,* 1989, **91**, 7319–7330.

26. K. Mizuse, J.L. Kuo and A. Fujii, *Chem. Sci*., 2011, **2**, 868-876.

27. H. Do and N.A. Besley *J. Phys. Chem., A*, 2013, **117**, 5385-5391.

28. D.R. Hartree, *Math. Proc. Camb. Philos. Soc.,* 1928, **24**, 89-110.

29. D.R. Hartree, *Math. Proc. Camb. Philos. Soc.,* 1928, **24**, 111-132.

30. D.R. Hartree, *Math. Proc. Camb. Philos. Soc.,* 1928, **24**, 426-437.

31. V. Fock, *Z. Phys.,* 1930, **61**, 126.

32. Roothaan, C. C. J., *Rev. Mod. Phys.,* 1951, **23**, 69−89.

33. Hall, G. G., *Proc. R. Soc. London, Ser. A*., 1951, **205**, 541−552.

34. S. F. Boys, *Proc. Roy. Soc. (London)*, 1950, **A200**, 542.

35. M. Sodupe, J. Bertran, L. Rodriguez-Santiago and E.J. Bearends, *J. Phys. Chem. A*., 1999, **103**, 166-170.

36. M. Lundberg and P.E.M. Siegbahn, *J. Chem. Phys*., 2005, **122**, 224103.

37. R.C.R. Pennifold, S.J. Bennie, T.F. Miller, and F.R. Manby, *J. Chem. Phys.,* 2017, **146**, 084113.

38. del Bene, J. Ditchfield, R. Pople, J. A. *J. Chem. Phys.,* 1971, **55**, 2236.

39. R. Ditchfield, W. J. Hehre, and J. A. Pople, *J. Chem. Phys.,* 1970, **52**, 5001.

40. W. J. Hehre, R. F. Stewart, J. A. Pople, *J. Chem. Phys.,* 1969, **51**, 2657–2664.

41. T.H Dunning, *J. Chem. Phys.,* 1989, **90**, 1007 – 1023.

42. C. Møller and M. S. Plesset, *Phys. Rev.,* 1934, **46**, 618−622.

43. F. Coester, *Nucl. Phys.,* 1958, **1**, 421.

44. F. Coester and H. Kümmel, *Nucl. Phys.,* 1960, **17**, 477.

45. P. Hohenberg, W. Kohn, *Phys. Rev.,* 1964, **136**, B864–B871.

46. P. Hohenberg, W. Kohn, *Phys. Rev.,* 1964, **136**, B864.

47. W. Kohn, L. Sham L, *J. Phys. Rev.,* 1965, **140**, A1133–A1138.

48. K. Kim and K. D. Jordan, *J. Phys. Chem.,* 1994, **98**, 10089.

49. F. B. van Duijneveldt, J. G. C. M. van Duijneveldt-van de Rijdt, and J. H. van Lenthe, *Chem. Rev.,* 1994, **94**, 1873.

50. J.D. Wadey and N.A. Besley, *Chem. Phys. Lett.*, 2014, **601**, 110-115.

51. M.W.D. Hanson-Heine and N.A. Besley, *Chem. Phys. Lett.*, 2015, **638**, 191 – 195.

52. J. D. Chai, M. Head-Gordon, *Phys. Chem. Chem. Phys.*, 2008, **10**, 6615−6620.

53. P.F. Bernath, *Phys. Chem. Chem. Phys.*, 2002, **4**, 1501-1509.

54. C. Y. Lin, A. T. B. Gilbert, and P. M. W. Gill, *Theor. Chem. Acc.*, 2008, **120**, 23.

55. K.R. Siefermann and B. Abel, *Science*, 2010 **327**, 280-281.

56. N. Eyet, N.S. Shuman, A.A. Viggiano, J. Troe, R.A. Relph, R.P. Steele and M.A. Johnson, *J. Phys. Chem. A*, 2011 **115**, 7582-7590.

57. M. Sodupe, J. Bertran, L. Rodriguez-Santiago and E.J. Bearends, *J. Phys. Chem. A*, 1999, **103**, 166-170.

58. M. Lundberg and P.E.M. Siegbahn, *J. Chem. Phys.*, 2005, **122**, 224103.

59. R.C.R. Pennifold, S.J. Bennie, T.F. Miller and F.R. Manby, *J. Chem. Phys.*, 2017, **146**, 084113.

60. R. T. McGibbon, A. G. Taube, A. G. Donchev, K. Siva, F. Hernández, C. Hargus, K.-H. Law, J. L. Klepeis, D. E. Shaw, *J. Chem. Phys.* 2017, **147**, 161725.